Thermochemical Structure and Dynamics of Earth's Lowermost Mantle

by

Mingming Li

A Dissertation Presented in Partial Fulfillment
of the Requirements for the Degree
Doctor of Philosophy

Approved December 2014 by the
Graduate Supervisory Committee:

Allen K. McNamara, Chair
Edward J. Garnero
Sang-Heon Shim
James Tyburczy
Amanda Clarke

ARIZONA STATE UNIVERSITY

May 2015

ABSTRACT

Seismic observations have revealed two large low shear velocity provinces (LLSVPs) in the lowermost mantle beneath Pacific and Africa. One hypothesis for the origin of LLSVPs is that they are caused by accumulation of subducted oceanic crust on the core-mantle boundary (CMB). Here, I perform high resolution geodynamical calculations to test this hypothesis. The result shows that it is difficult for a thin (~ 6 km) subducted oceanic crust to accumulate on the CMB, and the major part of it is viscously stirred into the surrounding mantle. Another hypothesis for the origin of LLSVPs is that they are caused by thermochemical piles of more-primitive material which is remnant of Earth's early differentiation. In such case, a significant part of the subducted oceanic crust would enter the more-primitive reservoir, while other parts are either directly entrained into mantle plumes forming on top of the more-primitive reservoir or stirred into the background mantle. As a result, mantle plumes entrain a variable combination of compositional components including more-primitive material, old oceanic crust which first enters the more-primitive reservoir and is later entrained into mantle plumes with the more-primitive material, young oceanic crust which is directly entrained into mantle plumes without contacting the more-primitive reservoir, and depleted background mantle material. The result reconciles geochemical observation of multiple compositional components and varying ages of oceanic crust in the source of ocean-island basalts. Seismic studies have detected ultra-low velocity zones (ULVZs) in some localized regions on the CMB. Here, I present 3D thermochemical calculations to show that the distribution of ULVZs provides important information about their origin. ULVZs with a distinct composition tend to be located at the edges of LLSVPs, while ULVZs solely

i

caused by partial melting tend to be located inboard from the edges of LLSVPs. This indicates that ULVZs at the edges of LLSVPs are best explained by distinct compositional heterogeneity, while ULVZs located insider of LLSVPs are better explained by partial melting. The results provide additional constraints for the origin of ULVZs.

DEDICATION

To my parents and my wife, who have been always supporting me to fulfill my curiosity

in Earth science.

谨以此文献给我的爸爸妈妈和我的妻子赵佳乐女士。我的一切成就源于他们对我在

生活和感情上的支持。

TABLE OF CONTENTS

LIST OF TABLES

LIST OF FIGURES

CHAPTER 1

INTRODUCTION

The Earth is formed about 4.6 billion years ago by accretion of asteroids and planetesimals. It is hypothesized that about 20-100 million years after the formation of Earth, a Mars-size object impacted the proto-Earth and formed the Moon [*Canup and Asphaug*, 2001; *Touboul et al.*, 2007; *Bourdon et al.*, 2008]. It is hypothesized that the Moon-forming impact led to large scale of melting in Earth's mantle, which is called the "magma ocean" [*Tonks and Melosh*, 1993; *Solomatov*, 2000; 2007]. As the Earth cools down, crystallization of the magma ocean causes differentiation in Earth's mantle (e.g., forming a dense layer of primordial mantle material at the bottom of the mantle [*Labrosse et al.*, 2007; *Lee et al.*, 2010]). The process and consequences of magma ocean crystallization play significant role in dictating how the Earth's mantle evolves to the present day. Understanding the composition and interior structure of Earth, and the thermal and chemical evolution of Earth's mantle remains one of the most challenging and important problems in Earth science.

In this chapter, I will first discuss the composition, structure, and mineral phases of Earth's mantle, which are followed by a summary of major tools used in studying the composition, structure and dynamics of Earth's deep mantle. I will then focus on the structure and dynamics of Earth's lowermost mantle, and pay special attention to the structure, dynamics and origin of the seismically observed large low shear velocity provinces (LLSVPs) and ultra-low velocity zones (ULVZs). A brief summary of this dissertation is provided at the end of this chapter.

1

1.1 Composition, Structure and Mineral Phases of Earth's Mantle

The Earth contains a silicate crust and mantle which are mainly made of Oxygen, Silicon, Magnesium, Iron and Aluminum, and a metallic core which is mainly made of Iron and Nickel. There are several ways to estimate the composition of the Earth. Chondrites, a type of undifferentiated meteorites which are believed to be fragments of primordial accretionary material, have the same composition as the Sun that holds 99.86% mass of the solar system [*Anders and Ebihara*, 1982; *Anders and Grevesse*, 1989]. Thus, one way to estimate the composition of the Earth is by analyzing the composition of chondrites and assuming that the concentration of refractory elements (the opposite of volatiles) of Earth are the same as that of chondrites [*Taylor*, 1964; *McDonough and Sun*, 1995]. Another method to constrain the composition of Earth is through chemical and petrological models [*Ringwood*, 1962; *Sun*, 1982; *Hart and Zindler*, 1986; *Irifune*, 1987; *McDonough and Sun*, 1995]. The philosophy behind this method is that decompression melting beneath mid-ocean ridge at a depth of about 60-80 km [*McKenzie and Bickle*, 1988] produces basaltic melts and leaves behind a layer of depleted mantle consisting of harzburgite. The composition of mid-oceanic ridge basalts (MORBs) and harzburgite are well known from direct samples on Earth's surface and xenoliths from the deep Earth, and the bulk composition of Earth's mantle rock is proposed to be equivalent to a mixture of 1 part of MORB with 4 parts of harzburgite [*Ringwood*, 1962; *Irifune*, 1987]. This theoretical mantle rock is called pyrolite [*Ringwood*, 1962].

The composition of pyrolite is different from chondritic Earth, with chondritic Earth has higher SiO_2 content and lower MgO content than pyrolite [*McDonough and*

2

Sun, 1995]. This contradiction has led some authors to propose that the pyrolite model is only applicable to the upper mantle while the Earth's lower mantle has different composition than the upper mantle [*Hofmann*, 1997], or there is a hidden reservoir in the lower mantle with Si enriched [*Kellogg et al.*, 1999], or the missing Si in pyrolite model has been partitioned into Earth's core [*O'Neill*, 1991; *Takafuji et al.*, 2005], or the bulk silicate Earth is not chondritic [*Campbell and O'Neill*, 2012; *Fitoussi and Bourdon*, 2012].

In addition to major elements, the Earth also contains trace elements whose concentration is less than 100 ppm. In terms of trace element chemistry, the bulk silicate Earth contains several compositional components, including subducted oceanic crust, depleted mantle material, more-primordial reservoir, and some other enriched reservoirs (EM1 and EM2) which may be related to continental crust and oceanic sediments [*Hofmann*, 1997; *Hofmann et al.*, 2007; *Tackley*, 2007]. The oceanic crust is formed at mid-ocean ridges by decompression melting and is later subducted into the deep mantle with the cold oceanic lithosphere. The fate of subducted oceanic crust is still controversial. It has been proposed to accumulate on the core-mantle boundary [*Christensen and Hofmann*, 1994; *Brandenburg and van Keken*, 2007; *Nakagawa et al.*, 2010], be brought up to the surface by mantle plumes [*Li and McNamara*, 2013; *Li et al.*, 2014a], or be mixed into the background mantle [*Li and McNamara*, 2013; *Li et al.*, 2014a]. Geochemists often attribute the high $\mu={}^{238}U/{}^{204}Pb$ of oceanic island basalts (OIBs) to the recycled oceanic crust which has been brought up to the surface by mantle plumes [*Hofmann*, 1997; *Hofmann et al.*, 2007; *Tackley*, 2007]. The depleted mantle refers to the mantle which has undergone partial melting and is highly degassed

3

[*Hofmann*, 1997; *Hofmann et al.*, 2007; *Tackley*, 2007]. The more-primordial reservoir refers to the part of mantle which is formed during the early differentiation events and survives later mixing due to mantle convection and is less degassed after its formation [*Hofmann*, 1997; *Deschamps et al.*, 2012]. The feature of high ^{3}He/^{4}He ratio of some OIBs is often attributed to the occurrence of more-primordial material in their melting sources [*Hofmann*, 1997; *Graham*, 2002].

An indirect way to estimate the composition of Earth's mantle is through geophysical studies [*Ricolleau et al.*, 2009; *Stixrude and Lithgow-Bertelloni*, 2011; 2012]. The basic assumption is that different mineral phases have different physical properties such as seismic velocities and density. Thus, the mineral assemblage and thus composition of Earth's mantle can be estimated once seismic velocities and/or density of the Earth's mantle are measured through geophysical studies. However, the difficulty of interpreting seismic velocities and density in terms of composition and mineral assemblage is that these physical properties are significantly affected by pressure, temperature, mineral phases, amount of partial melting and volatile content as well, and the composition model of Earth's mantle constrained using this method is often non-unique.

The 1D model of Earth's seismic structure is featured by a number of seismic discontinuities [*Dziewonski and Anderson*, 1981]. From Earth's surface to the core, the major seismic discontinuities include crust-mantle boundary, lithosphere-asthenosphere boundary, 410 km discontinuity, 520 km discontinuity, 660 km discontinuity, D" discontinuity, core mantle boundary, and inner-outer core boundary. These seismic discontinuities are caused by either composition changes, or phase transitions, or

4

rheology changes. A lot of efforts have been devoted to understand the origin of these seismic discontinuities. In addition, seismic studies have shown that the structure of Earth's mantle is far away from the 1D average model. Strong lateral variations of seismic velocities are observed, particularly in the upper and lowermost mantle [*Ritsema et al.*, 2011].

Olivine and pyroxene are two major mineral phases in Earth upper mantle. In Earth's transition zone from 410 to 660 km, olivine undergoes a series of phase transitions [*Ringwood*, 1982; 1991]. At ~410 km depth (~13.8GPa), olivine is transformed to wadsleyite. At ~520 km (~18GPa), wadsleyite is transformed to ringwoodite. At ~660 km (~23.5 GPa), ringwoodite is disproportionated to Mg-perovskite and (Mg,Fe)O manesiowüstite. In Earth's transition zone, pyroxene is gradually dissolved into garnet until about 700 km at which depth garnet is transformed into Mg-perovskite. Phase transitions in the transition zone cause rapid increase of density and seismic velocities. In the lower mantle, Mg-perovskite and (Mg,Fe)O manesiowüstite are two major mineral phases. Mineral physical experiments found that Mg-perovskite (pv) is further transformed to post-perovskite (ppv) at a depth of several hundred kilometers above the core-mantle boundary (CMB) [*Murakami et al.*, 2004; *Oganov and Ono*, 2004; *Tsuchiya et al.*, 2004; *Shim*, 2008]. The depth of pv-ppv phase transition coincides with the depth of D" layer and the D" seismic discontinuity is often explained by this phase transition [*Hernlund et al.*, 2005; *Wookey et al.*, 2005; *Lay et al.*, 2006; *Lay*, 2008].

1.2 Tools to Study the Structure and Dynamics of Earth's Mantle

The study of structure and dynamics of Earth's mantle involves incorporative work from multiple disciplines, including seismology, mineral physics, geochemistry and geodynamics.

Seismology is the most important and efficient way through which we know the interior structure of the Earth. Seismic waves are elastic waves which travel through Earth's interior from source (location of earthquakes) to receiver (seismic stations). The travel time of seismic phases depends on seismic velocities along the traveling paths. The frequencies of seismic waveforms are sensitive to seismic heterogeneities with different length scale. The amplitude of some reflective seismic phases is influenced by the contrast of seismic velocities and density between seismic heterogeneities and their surroundings. By analyzing the travel time and amplitude of seismic phases and comparing synthetic seismograms with observed seismic waveforms, seismologists are able to calculate seismic velocities and density of the deep Earth.

However, in order to better understand the structure and dynamics of Earth's mantle, we often need to interpret seismic observations in terms of other parameters, such as pressure, temperature, composition, mineral phases, partial melting, and water content. The relationship between these parameters and seismic velocities could be understood through high-pressure-temperature mineral physics experiments. In addition, physical properties (e.g., viscosity, density, thermal expansivity and thermal diffusivity) that greatly influences the dynamics of Earth's mantle are also measured in mineral physics experiments. Mineral physics experiments thus provide fundamental information for us to explore the structure and dynamics of Earth's mantle.

The bulk composition of the Earth is mainly constrained through geochemical observations of the composition of chodrodites, surface rocks, sediments, and xenoliths from the deep interior. In addition, trace elements whose concentration is less than 100 ppm also play significant role for us to understand the process of Earth's differentiation and chemical evolution. Depending on their ability to enter the structural site of crystals, trace elements are divided into compatible and incompatible elements. Different from compatible elements, the incompatible elements are unsuitable for the cation sites of crystals. Once partial melting occurs within the Earth, incompatible trace elements are partitioned into melts while compatible elements remain in the solid phase. Thus the abundance of compatible and incompatible trace elements within magmas (and rocks after the crystallization of magmas), not only depends on the composition of their melting sources, but also depends on their partition coefficient between melt and solid mineral phases and the amount of partial melting. Because of this, the abundance of trace elements give important information about the melting process, the composition and mineral phases of melting sources. By analyzing the abundance of radioactive isotopes (e.g., ^{235}U, ^{238}U, ^{40}K, ^{147}Sm) within rocks, geochemists could estimate the age of these rocks, which is also the time when partial melting or metamorphism occurs. By combining this age information with the partial melting process unveiled through the analysis of trace elements within rocks, clear process of Earth's chemical evolution could be depicted by geochemists.

One challenge in geochemical studies is to constrain the location of compositional reservoirs, such subducted oceanic crust and more-primitive reservoir. This problem can be addressed when combining with seismic observations of the location of these

compositional reservoirs, if these reservoirs have large enough contrast of seismic velocities and density from their surrounding mantle.

Geodynamical modeling is one of the most powerful tool to explore the thermal and chemical evolution and dynamics of Earth's mantle. For geological time scale, Earth's mantle can be treated as ductile like viscous fluid, and the process of mantle convection should follow the fundamental rules of conservation of mass, momentum and energy. In geodynamical modeling, we solve these conservation equations using computers. We setup numerical models and the solution for temperature, velocity and pressure are found at every time-step. However, because some physical parameters (especially viscosity) about the Earth's mantle are not very well constrained and because of the limitation of computational power, modeling the 'real Earth' is not practical. More often, we treat geodynamical modeling as an experimental tool to answer specific scientific questions. That is, appropriate numerical models are setup to address these specific questions. For example, a numerical model could be either two dimensional or three dimensional, either isochemical or thermochemical, either spherical or Cartesian, depending on the scientific questions we need to answer. Usually, numerical models include a reference case with the best estimation of physical parameters of the Earth's mantle. In addition to the reference case, a series of other cases are performed to investigate how changes of physical parameters affect the results. The results of geodynamical modeling are often compared with geochemical and geophysical observations. A good model should be as simple as possible, but still be able to explain most phenomenon and observations.

1.3 Earth's Lowermost Mantle

The Earth's lowermost mantle acts as a lower boundary layer for mantle convection. As a result, the thermochemical structure and dynamics of Earth's lowermost mantle play crucial role in controlling the style of mantle convection and the thermal and chemical evolution of Earth's mantle.

1.3.1 Seismic Structure

Seismic observations have revealed strong seismic heterogeneities in Earth's lowermost several hundred kilometers of the mantle [*Masters et al.*, 2000]. The large-scale features of Earth's lowermost mantle are characterized by degree two seismic heterogeneities with large low shear velocity provinces (LLSVPs) beneath central Pacific and Africa [*Li and Romanowicz*, 1996; *Su and Dziewonski*, 1997; *Garnero and McNamara*, 2008; *Dziewonski et al.*, 2010; *Ritsema et al.*, 2011; *He and Wen*, 2012], which are surrounded by high seismic velocity regions that have been suggested to be locations of past subducted slabs [*Garnero and McNamara*, 2008; *Ritsema et al.*, 2011]. Roughly, the LLSVPs reside in regions with increased density and anti-correlation between shear wave velocity and bulk sound velocity [*Ishii and Tromp*, 2004; *Trampert et al.*, 2004]. High $dlnV_s/dlnV_p$ ratio (>2.5) have also been reported in the lowermost mantle [*Masters et al.*, 2000; *Romanowicz*, 2003; *Ishii and Tromp*, 2004], indicating that the lowermost mantle is compositionally heterogeneous.

Using high resolution seismic forward modeling, seismologists have found a lot interesting small-scale structures in Earth's lowermost mantle. These structures include seismic discontinuities within LLSVPs [*Lay et al.*, 2006; *Ohta et al.*, 2008], rapid shear wave velocity increase across the D" discontinuity [*Kito et al.*, 2007; *van der Hilst et al.*,

9

2007; *Lay*, 2008; *He and Wen*, 2011], ultra-low velocity zones (ULVZs) with significant reduction of seismic velocities and possibly increased density [*Garnero and Helmberger*, 1996; *Revenaugh and Meyer*, 1997; *Wen and Helmberger*, 1998b; *Rost et al.*, 2005; *Cottaar and Romanowicz*, 2012], and seismic scatters on the core-mantle boundary [*Niu and Wen*, 2001; *Miller and Niu*, 2008; *Rost and Earle*, 2010]. In addition, seismic anisotropy is found in the lowermost mantle at subducting regions [*Yamazaki et al.*, 2006; *He and Long*, 2011; *Walker et al.*, 2011; *Cottaar et al.*, 2014] and at the edges of LLSVPs [*Wang and Wen*, 2007a; *Lynner and Long*, 2014], which provides important information of the mantle flow velocity in these regions.

1.3.2 Compositional Heterogeneity

The Earth's core mantle boundary is a first order discontinuity, with solid silicate mantle above the molten metallic outer core. Because of large density and viscosity contrast between Earth's lowermost mantle and outer core, large exchanges of material between core and mantle are not possible (although it has been suggested that interaction between core and mantle could produce a small amount of iron enriched materials in the lowermost mantle [*Buffett et al.*, 2000; *Kanda and Stevenson*, 2006]). Thus, the lowermost mantle acts as a grave yard for dense compositional heterogeneities [*Masters et al.*, 2000]. Candidates of compositional heterogeneities of the lowermost mantle include: (1) production of interaction between mantle and core [*Buffett et al.*, 2000; *Kanda and Stevenson*, 2006], (2) a more-primitive dense reservoir formed by differentiation in early history of the Earth [*Kellogg et al.*, 1999; *Labrosse et al.*, 2007; *Nomura et al.*, 2011], and (3) accumulation of subducted oceanic crust at the CMB [*Hofmann and White*, 1982; *Christensen and Hofmann*, 1994; *Hirose et al.*, 2005;

10

Brandenburg and van Keken, 2007; *Fujita and Ogawa*, 2009; *Nakagawa et al.*, 2010; *Ogawa*, 2010]. Some features of the LLSVPs such as increased density [*Ishii and Tromp*, 2004; *Trampert et al.*, 2004] and sharp edges [*Ni et al.*, 2002; *To et al.*, 2005; *Sun et al.*, 2007a; *Sun et al.*, 2007b] are better explained by compositional heterogeneity. Seismic scatters and discontinuities within LLSVPs have been proposed to be caused by subducted oceanic crust [*Miller and Niu*, 2008; *Ohta et al.*, 2008]. Recently, it is found that density and seismic velocities of ULVZs are consistent with iron enriched (Mg,Fe)O [*Wicks et al.*, 2010; *Bower et al.*, 2011], which could be caused by accumulation of Banded Iron Formation (BIF) [*Dobson and Brodholt*, 2005], subducted oceanic crust [*Ohtani and Maeda*, 2001; *Andrault et al.*, 2014] or production of core mantle interaction [*Knittle and Jeanloz*, 1989; *Brandon and Walker*, 2005; *Hayden and Watson*, 2007; *Otsuka and Karato*, 2012].

Previous numerical modelling results have shown that the dense compositional heterogeneity on the CMB could be passively pushed by cold subducting slabs into thermochemical piles beneath upwelling regions [*McNamara and Zhong*, 2005; *Zhang et al.*, 2010; *Bull et al.*, 2014]. However, the interaction between the compositional heterogeneity in the lowermost mantle and subducting slabs is still unclear. In fact, past plate motion reconstruction and paleo-magmatic results have shown that the LLSVPs remain in the same location for over 540 million years [*Torsvik et al.*, 2014], which implies that the compositional heterogeneity that causes LLSVPs are very stable and may not be passively swept by subducting slabs.

What happens in Earth's lowermost mantle sometimes manifests on the surface in term of geochemistry of hotspot lavas which are suggested to be caused by mantle

11

plumes [*Hofmann*, 1997; *Samuel and Farnetani*, 2003; *Tackley*, 2007; *Hahm et al.*, 2009; *Deschamps et al.*, 2011; *Li et al.*, 2014a]. It is thus of great interest and importance to explore the interaction between mantle plumes and compositional reservoirs and see how does it contribute to the geochemistry of hotspots basalts.

1.3.3 Thermal Structure and Mantle Plume

Earth's lowermost mantle is a thermal boundary layer, with rapid temperature change across the lowermost mantle (on the order of 1,000 K for the lowermost 200 km of Earth's mantle [*Lay et al.*, 2008]). Thermal instabilities origin from the lowermost mantle cause upwelling mantle plumes. It has been suggested that the LLSVPs are caused by superplumes or plume clusters, although the origin of LLSVPs is still under debate. Extrapolating temperature at the inner-core boundary to CMB gives the CMB temperature in the range of 3,500-4,300 K [*Lay et al.*, 2008]. Melting temperature of chondritic mantle at the CMB pressure is constrained to be around 4000 K [*Andrault et al.*, 2011], and much lower melting temperature (3,500-3,800 K) at the CMB condition has also been proposed by mineral physicists for hydrous pyrolite and basalts [*Andrault et al.*, 2014; *Nomura et al.*, 2014]. Thus, partial melting in the lowermost mantle is not impossible and large reduction of seismic velocities (e.g., ULVZs) is often attributed to partial melting [*Williams and Garnero*, 1996].

The structure of Earth's lowermost mantle is directly linked to its dynamics. Mantle plumes forming in the lowermost mantle advect heat out of Earth's core to the mantle. As these mantle plumes reach the surface, they may cause large igneous provinces and hotspots. However, the process of how mantle plumes form and advect heat to the surface is greatly controlled by thermal and compositional structure of the

12

lowermost mantle. For an isochemical lowermost mantle, mantle plumes form on the

CMB and directly advect heat to the surface [*Li and McNamara*, 2013]. However, a layer

of dense material on the CMB, (e.g., primordial reservoir, accumulation of subducted

oceanic crust), will block heat from directly coming out of the core to the mantle. Mantle

plumes would form on top of the dense material [*Farnetani*, 1997; *Li et al.*, 2014a], but

with lower temperature than mantle plumes forming on the CMB [*Farnetani*, 1997;

Zhong, 2006]. In addition, due to the insulating effects of the dense compositional

heterogeneity, temperature within the compositional heterogeneity increases rapidly,

which has a big effect on CMB heat flux [*Nakagawa and Tackley*, 2004], and

temperature of the mantle above the dense layer would decrease much faster than

isochemical condition [*Zhong*, 2006].

1.3.4 Post-Perovskite Phase Transition

Ten years ago, high-temperature-pressure experiments demonstrated that

perovskite (pv) is not sable under temperature and pressure conditions of Earth's

lowermost mantle, but is transformed into a different structure post-perovskite (ppv) with

increasing of density and shear wave velocity [*Murakami et al.*, 2004; *Oganov and Ono*,

2004; *Tsuchiya et al.*, 2004; *Shim*, 2008]. The D" seismic discontinuity is often attributed

to the pv-ppv phase transition [*Lay et al.*, 2006; *Kito et al.*, 2007; *van der Hilst et al.*,

2007; *Lay*, 2008]. In addition, the pv-ppv phase transition has also been used to explain

seismic discontinuities within LLSVPs [*Lay et al.*, 2006]. Furthermore, the ppv phase

transition occurs at different depths for MORB, pyrolite and harzburgite, leading to

multiple seismic discontinuities in the D" layer [*Shang et al.*, 2014]. Anisotropy in the D"

layer has also been attributed to the ppv phase transition [*Merkel et al.*, 2007; *Ammann et al.*, 2010; *Nowacki et al.*, 2010].

The pv-ppv phase transition leads to about 1% density increase [*Oganov and Ono*, 2004; *Shim*, 2008], and the Clapeyron slope for this phase transition is constrained to be about ~7-10 MPa/K [*Oganov and Ono*, 2004; *Tsuchiya et al.*, 2004]. Past numerical modeling results have shown that this phase transition significantly increases the CMB heat flux. In addition, results from lab experiments and first-principle calculations showed that ppv is weaker (lower viscosity) than pv [*Hunt et al.*, 2009; *Ammann et al.*, 2010]. The weak ppv could noticeably modify the dynamics of Earth's lowermost mantle, such as accelerates the speed of downwelling slabs [*Nakagawa and Tackley*, 2011], enhances the segregation of subducted oceanic crust [*Li and McNamara*, 2013; *Li et al.*, 2014a] and leads to large steepness of the thermochemical piles of chemical heterogeneity [*Li et al.*, 2014b].

1.3.5 Spin Transition

The Fe spin crossover from high-spin to low-spin in Earth's lower mantle has been proved by both experiments [*Lin et al.*, 2005; *Fei et al.*, 2007; *Lin et al.*, 2007] and first-principle calculations [*Wu and Wentzcovitch*, 2014]. The spin transition could affect seismic velocities of Earth's lower mantle [*Irifune et al.*, 2010; *Badro*, 2014; *Wu and Wentzcovitch*, 2014]. Using first-principles calculations, *Wu and Wentzcovitch* [2014] found that the anti-correlation between shear wave velocity and bulk sound velocity in Earth's lower mantle could be explained by spin transition within ferropericlase. However, seismic observations do not find a discontinuity at the mid-lower mantle. This

may be because the spin transition occurs gradually and does not cause a noticeable sharp changes of seismic velocities [*Badro*, 2014].

The Fe spin transition in Earth's lower mantle results in about 2-4% of density increase [*Lin et al.*, 2013; *Badro*, 2014]. Previous numerical modeling studies by *Bower et al.* [2009] found that the spin transition could lead to enhanced mantle convection and fast mantle plumes.

1.3.6 LLSVP

Seismic observations have revealed two Large Low Shear Velocity Provinces (LLSVPs) in the lowermost mantle beneath central Pacific and Africa [*Li and Romanowicz*, 1996; *Su and Dziewonski*, 1997; *Garnero and McNamara*, 2008; *Dziewonski et al.*, 2010; *Ritsema et al.*, 2011; *He and Wen*, 2012]. The LLSVPs cover about 21% area of the CMB [*Burke et al.*, 2008] and reach a height of about 1000 km [*He and Wen*, 2009; 2012]. Seismic forward modeling have shown shear wave velocity of LLSVPs ranges from 3% to 5% lower than the 1D PREM model [*He and Wen*, 2009; 2012] and the edges of LLSVPs are sharp [*Luo et al.*, 2001; *Ni et al.*, 2002; *To et al.*, 2005]. The LLSVPs are further suggested to be denser than their surrounding mantle as is shown by seismic studies using Earth's free oscillation [*Ishii and Tromp*, 1999; *Trampert et al.*, 2004]. In addition, seismic discontinuities are found within LLSVPs [*Lay et al.*, 2006; *Ohta et al.*, 2008]. Statistical analyses found that the edges of LLSVPs coincide well with the locations of ancient and present hotpots on Earth's surface [*Wen*, 2006; *Torsvik et al.*, 2010].

The structure, composition, origin and dynamics of LLSVPs are crucial for us to understand the thermal and chemical evolution of Earth's mantle. Various mantle

convection models have been put forward to explain the origin and evolution of LLSVPs, among which are superplumes [*Su et al.*, 1994; *Davaille*, 1999; *Davaille et al.*, 2002; *Jellinek and Manga*, 2004; *Davaille et al.*, 2005], plume clusters [*Schubert et al.*, 2004], piles with high bulk modulus [*Tan and Gurnis*, 2005; 2007] and thermochemical piles [*Tackley and Xie*, 2002; *McNamara and Zhong*, 2005] consist of accumulation of subducted oceanic crust [*Christensen and Hofmann*, 1994] and/or more-primitive material [*Deschamps et al.*, 2012] which is remnants of Earth's early differentiation.

Each of these models is related to different style of mantle dynamics of the Earth. For the superplume model, large thermal domes are formed in hot regions of the lowermost mantle where thermal buoyancy of dense material overcomes its intrinsic chemical buoyancy. As the dense and hot material goes up, it cools down. When it becomes cold enough and becomes negative buoyant, it again sinks to the CMB. Thus the hot and dense domes are oscillating between different stage of rises and falls [*Davaille*, 1999]. Numerical studies show that compositional increase of viscosity is needed for superplumes to form from a dense layer [*McNamara and Zhong*, 2004].

Different from large superplumes, the plume cluster model is characterized by a collection of small-scale mantle plumes which are swept by horizontal flows toward the upwelling center, forming clusters of plumes [*Schubert et al.*, 2004]. For this model, composition only plays a second order role. Owing to the low resolution of seismic tomography, the plume cluster model cannot be simply ruled out [*Bull et al.*, 2009; *Bull et al.*, 2010].

By conducting compressible numerical calculations, [*Tan and Gurnis*, 2005; 2007] show that if the bulk modulus of denser material is higher than that of the

16

background mantle, the slope of chemical density anomaly with depth can be negative (this is, the intrinsic density anomaly decreases with depth). Because temperature increases with depth, it is possible that at some depth (named HNB in [*Tan and Gurnis*, 2005; 2007]) chemical buoyancy neutralizes with thermal buoyancy. In that sense, the net buoyancy force will be negative above the HNB and positive below the HNB. With proper bulk modulus and density anomaly, metastable superplumes can form, with high topography and sharp side boundaries [*Tan and Gurnis*, 2007]. This is the so-called high-bulk modulus model.

When viscosity in the lower mantle is temperature dependent, dense and hot material at the CMB are passively advected to the upwelling center by cold and more viscous subducted slabs, forming thermochemical piles with ridge-like shape and sharp boundaries [*Tackley*, 1998; *McNamara and Zhong*, 2005]. Mantle plumes form on top of the piles and material from the piles is slowly entrained into mantle plumes [*Deschamps et al.*, 2011; *Li et al.*]. This is called thermochemical pile model. In this model, the compositional heterogeneity could be caused by either accumulation of subducted oceanic crust on the CMB [*Christensen and Hofmann*, 1994], or more-primitive material [*Deschamps et al.*, 2012], or both [*Li et al.*, 2014a; *Nakagawa and Tackley*, 2014].

1.3.7 ULVZ

Compared to the large volume of LLSVPs, ultra-low velocity zones (ULVZs) have much smaller length scale (on the order of 10 km thick and 100 km across). In general, the small size ULVZs have significant reduction of seismic velocities and possibly increased density. However, the physical properties of ULVZs (seismic velocity and density), the locations of ULVZs respected to the location of LLSVPs, and the

17

morphology of ULVZs are found to be quite different in different regions on the CMB. The P wave speed anomaly of reported ULVZs varies from -4% [*Avants et al.*, 2006] to -25% [*Ross et al.*, 2004] and the S wave speed anomaly varies from -2% [*Avants et al.*, 2006] to -50% [*Rondenay and Fischer*, 2003]. The density anomaly of some ULVZs has been revealed to be about 10% [*Rost et al.*, 2005] denser than surrounding mantle, but up to 50% increase of density of some ULVZs has also been reported by seismologists [*Rost and Revenaugh*, 2003]. The height of ULVZ is normally in the range of 5-40 km [*Garnero and Helmberger*, 1996; *Rost and Revenaugh*, 2003; *Rost et al.*, 2006]. However, some ULVZs have a thickness more than 80 km [*To et al.*, 2011; *Sun et al.*, 2013]. In general, the lateral scale of ULVZs is to the order of several hundred kilometers [*Wen and Helmberger*, 1998b; *Helmberger et al.*, 2000; *Rost et al.*, 2006; *To et al.*, 2011]. However, mega-ULVZ is also found whose lateral scale is almost 1,000 km [*Cottaar and Romanowicz*, 2012]. Furthermore, while most ULVZs are found to be located at the edges of LLSVPs [*Rost et al.*, 2006], ULVZs within LLSVPs have also been reported [*Wen and Helmberger*, 1998a]. The seismic detections of ULVZs are summarized in *McNamara et al.* [2010] and *Bower et al.* [2011].

Several hypotheses for the origin of ULVZs have been proposed. Here, in terms of composition of ULVZs, we divided the hypotheses of origin of ULVZs into two groups. One hypothesis is that ULVZs have the same composition as LLSVPs. In this hypothesis, ULVZs are caused by partial melting in the hottest regions of LLSVPs [*Williams and Garnero*, 1996]. This hypothesis is supported by the 3:1 ratio of seismic S and P wave speed reduction of some ULVZs [*Williams and Garnero*, 1996; *Rost et al.*, 2005], which could be explained by about 5-30% partial melting [*Williams and Garnero*,

1996; *Hier-Majumder*, 2008]. Mineral physics experiments suggests that partial melts are more compressible and are denser than the solid phase at pressure and temperature condition of Earth's lowermost mantle [*Murakami and Bass*, 2011]. In order to cause partial melting on the CMB, temperature at the CMB should equal to or higher than the melting temperature of Earth's lowermost mantle material. There is still big uncertainty on the temperature of the CMB [*Lay et al.*, 2008]. Within this uncertainty, mineral physical studies found that it is still possible for partial melting to occur at the bottom of the mantle [*Andrault et al.*, 2011; *Andrault et al.*, 2014; *Nomura et al.*, 2014]. In addition, numerical calculations by *Steinbach and Yuen* [1999] showed that viscous heating can heat up the interior of mantle plumes to around 100 degrees above the CMB temperature. They proposed that this amount of temperature increase is sufficient to cause partial melting within upwelling regions in the deep lower mantle.

The other hypothesis for the origin of ULVZs is that ULVZs have different composition as LLSVPs [*Wicks et al.*, 2010]. For example, ULVZs are caused by distinct composition which is iron-enriched and/or has lower melting temperature, and may or may not include partial melting [*Ohtani and Maeda*, 2001; *Mao et al.*, 2005; *Hernlund and Jellinek*, 2010; *Nomura et al.*, 2011; *Andrault et al.*, 2014]. In this case, the locations of ULVZs are mainly controlled by mantle convection [*McNamara et al.*, 2010]. This hypothesis explains why some ULVZs do not have 3:1 ratio of seismic S and P wave speed reduction [*Avants et al.*, 2006]. *Wicks et al.* [2010] found that the sound speed and density of iron-enriched solid $(Mg_{.16}Fe_{.84})O$ are compatible with seismic observations of ULVZs and they proposed an iron-enriched solid origin of ULVZs. *Mao et al.* [2005] and *Mao et al.* [2006] found that post-Perovskite in Earth's lowermost mantle is able to

19

contain a large amount of iron (up to 40 mol% FeSiO$_3$), and they proposed that ULVZs are caused by iron-enriched post-Perovskite. Several hypothetical processes have been proposed to explain the iron-enriched compositional heterogeneity in Earth's lowermost mantle: (1) small accumulation of subducted banded iron formation [*Dobson and Brodholt*, 2005], or subducted oceanic crust on the CMB [*Ohtani and Maeda*, 2001; *Andrault et al.*, 2014]; (2) products of core mantle interaction [*Knittle and Jeanloz*, 1991; *Kanda and Stevenson*, 2006] and (3) remnants of Earth's early differentiation and magma crystallization [*Labrosse et al.*, 2007].

The origin and dynamics of ULVZs are among the most important questions in Earth science. Whether ULVZs contain partial melts or not depends on solidus of Earth's lowermost mantle material and temperature at the CMB. Understanding the solid or molten state of ULVZs helps to constrain the temperature at the CMB and heat flux from the core, and also helps to constrain the composition of ULVZs. The composition and origin of ULVZs are important for understanding the process of Earth's chemical evolution. Furthermore, the distribution and morphology of ULVZs are controlled by physical properties (e.g., density, viscosity) of ULVZs and their interaction with LLSVPs, which as a result, provide information about the dynamics of Earth's lowermost mantle.

The morphology, distribution and dynamics of ULVZs are best assessed with geodynamic models. If ULVZs are caused by partial melting, *Hernlund and Tackley* [2007] found that melts would form a thin molten layer on the CMB if they have increased density, which is inconsistent with the topography of ULVZs detected by seismic studies. Later, *Hernlund and Jellinek* [2010] proposed that viscous stress is able

to suspend the dense melts in solid matrix. *Hier-Majumder and Revenaugh* [2010] found that the topography of ULVZs is strongly controlled by the viscosity of ULVZs. They proposed that ULVZs are about two orders weaker than the background lower mantle, based on the topography of ULVZs as is observed by seismic studies. *Beuchert and Schmeling* [2013] found that the viscosity reduction of ULVZs has a large effects on enhancing mantle flow velocity and increasing mantle temperature. The dynamics of dense solid-state ULVZs is studied by *Bower et al.* [2011], who found that the shape of these ULVZs is largely dictated by their density, with denser ULVZs having larger aspect ratio (relief/half-width). *McNamara et al.* [2010] investigated the interaction between small accumulations of compositionally different ULVZs and large scale dense thermochemical piles at the lowermost mantle. They demonstrated that small accumulations of compositionally different ULVZs can be supported by mantle convection. The ULVZs tend to be located at the edges of the piles, though the location of ULVZs change with mantle flow pattern.

Previously, the dynamics of ULVZs are simulated in 2D numerical models. However, in order to better understand the morphology and distribution of ULVZs and their interaction with LLSVPs, 3D models which simulate the entire mantle convection are essential, and this work is presented in Chapter 5.

1.4 Summary

In this dissertation, we use numerical modeling to study the structure and dynamics of Earth's lowermost mantle. In Chapter 2, we describe the conservation equations and numerical method. In Chapter 3, we investigate the possibility of forming LLSVPs by accumulation of subducted oceanic crust. In Chapter 4, we study the

interaction between mantle plumes, more-primitive reservoir and subducted oceanic crust and its implication for the trace element chemistry of OIBs. In Chapter 5, we explore the 3D morphology and distribution of ULVZs and their implication for the origin of ULVZs. In Chapter 6, we summarize our main conclusions and their implications.

References

Ammann, M. W., J. P. Brodholt, J. Wookey, and D. P. Dobson (2010), First-principles constraints on diffusion in lower-mantle minerals and a weak D" layer, *Nature*, *465*(7297), 462-465, doi:10.1038/nature09052.

Anders, E., and M. Ebihara (1982), Solar-system abundances of the elements, *Geochimica et Cosmochimica Acta*, *46*(11), 2363-2380, doi:10.1016/0016-7037(82)90208-3.

Anders, E., and N. Grevesse (1989), Abundances of the elements: Meteoritic and solar, *Geochimica et Cosmochimica Acta*, *53*(1), 197-214, doi:10.1016/0016-7037(89)90286-X.

Andrault, D., N. Bolfan-Casanova, G. L. Nigro, M. A. Bouhifd, G. Garbarino, and M. Mezouar (2011), Solidus and liquidus profiles of chondritic mantle: Implication for melting of the Earth across its history, *Earth and Planetary Science Letters*, *304*(1-2), 251-259, doi:10.1016/j.epsl.2011.02.006.

Andrault, D., G. Pesce, M. A. Bouhifd, N. Bolfan-Casanova, J.-M. Hénot, and M. Mezouar (2014), Melting of subducted basalt at the core-mantle boundary, *Science*, *344*(6186), 892-895, doi:10.1126/science.1250466.

Avants, M., T. Lay, and E. J. Garnero (2006), A new probe of ULVZ S-wave velocity structure: Array stacking of ScS waveforms, *Geophysical Research Letters*, *33*(7), L07314, doi:10.1029/2005gl024989.

Badro, J. (2014), Spin Transitions in Mantle Minerals, *Annual Review of Earth and Planetary Sciences*, *42*(1), 231-248, doi:10.1146/annurev-earth-042711-105304.

Beuchert, M. J., and H. Schmeling (2013), A melting model for the lowermost mantle using Clapeyron slopes derived from experimental data: Consequences for the thickness of ultralow velocity zones (ULVZs), *Geochemistry Geophysics Geosystems*, *14*(1), 197-208, doi:10.1029/2012gc004356.

Bourdon, B., M. Touboul, G. Caro, and T. Kleine (2008), Early differentiation of the Earth and the Moon, *Philosophical Transactions of the Royal Society A: Mathematical, Physical and Engineering Sciences*, *366*(1883), 4105-4128, doi:10.1098/rsta.2008.0125.

Bower, D. J., M. Gurnis, J. M. Jackson, and W. Sturhahn (2009), Enhanced convection and fast plumes in the lower mantle induced by the spin transition in ferropericlase, *Geophysical Research Letters*, *36*(10), L10306, doi:10.1029/2009gl037706.

Bower, D. J., J. K. Wicks, M. Gurnis, and J. M. Jackson (2011), A geodynamic and mineral physics model of a solid-state ultralow-velocity zone, *Earth and Planetary Science Letters*, *303*(3-4), 193-202, doi:10.1016/j.epsl.2010.12.035.

Brandenburg, J. P., and P. E. van Keken (2007), Deep storage of oceanic crust in a vigorously convecting mantle, *Journal of Geophysical Research*, *112*(B6), B06403, doi:10.1029/2006jb004813.

Brandon, A. D., and R. J. Walker (2005), The debate over core-mantle interaction, *Earth and Planetary Science Letters*, *232*(3-4), 211-225, doi:10.1016/j.epsl.2005.01.034.

Buffett, B. A., E. J. Garnero, and R. Jeanloz (2000), Sediments at the Top of Earth's Core, *Science*, *290*(5495), 1338-1342, doi:10.1126/science.290.5495.1338.

Bull, A. L., M. Domeier, and T. H. Torsvik (2014), The effect of plate motion history on the longevity of deep mantle heterogeneities, *Earth and Planetary Science Letters*, *401*(0), 172-182, doi:10.1016/j.epsl.2014.06.008.

Bull, A. L., A. K. McNamara, T. W. Becker, and J. Ritsema (2010), Global scale models of the mantle flow field predicted by synthetic tomography models, *Physics of The Earth and Planetary Interiors*, *182*(3-4), 129-138, doi:10.1016/j.pepi.2010.03.004.

Bull, A. L., A. K. McNamara, and J. Ritsema (2009), Synthetic tomography of plume clusters and thermochemical piles, *Earth and Planetary Science Letters*, *278*(3-4), 152-162, doi:10.1016/j.epsl.2008.11.018.

Burke, K., B. Steinberger, T. H. Torsvik, and M. A. Smethurst (2008), Plume generation zones at the margins of large low shear velocity provinces on the core-mantle boundary, *Earth and Planetary Science Letters*, *265*(1-2), 49-60, doi:10.1016/j.epsl.2007.09.042.

Campbell, I. H., and H. O'Neill (2012), Evidence against a chondritic Earth, *Nature*, *483*(7391), 553-558, doi:10.1038/nature10901.

Canup, R. M., and E. Asphaug (2001), Origin of the Moon in a giant impact near the end of the Earth's formation, *Nature*, *412*(6848), 708-712, doi:10.1038/35089010.

Christensen, U. R., and A. W. Hofmann (1994), Segregation of subducted oceanic crust in the convecting mantle, *Journal of Geophysical Research*, *99*(B10), 19867-19884, doi:10.1029/93JB03403.

Cottaar, S., M. Li, A. K. McNamara, B. Romanowicz, and H.-R. Wenk (2014), Synthetic seismic anisotropy models within a slab impinging on the core‐mantle boundary, *Geophysical Journal International*, *199*(1), 164-177, doi:10.1093/gji/ggu244.

Cottaar, S., and B. Romanowicz (2012), An unusually large ULVZ at the base of the mantle near Hawaii, *Earth and Planetary Science Letters*, *355-356*(0), 213-222, doi:10.1016/j.epsl.2012.09.005.

Davaille, A. (1999), Simultaneous generation of hotspots and superswells by convection in a heterogenous planetary mantle, *Nature*, *402*(6763), 756-760, doi:10.1038/45461.

Davaille, A., F. Girard, and M. Le Bars (2002), How to anchor hotspots in a convecting mantle?, *Earth and Planetary Science Letters*, *203*(2), 621-634, doi:10.1016/S0012-821X(02)00897-X.

Davaille, A., E. Stutzmann, G. Silveira, J. Besse, and V. Courtillot (2005), Convective patterns under the Indo-Atlantic <box> ?, *Earth and Planetary Science Letters*, *239*(3-4), 233-252, doi:10.1016/j.epsl.2005.07.024.

Deschamps, F., L. Cobden, and P. J. Tackley (2012), The primitive nature of large low shear-wave velocity provinces, *Earth and Planetary Science Letters*, *349*(0), 198-208, doi:10.1016/j.epsl.2012.07.012.

Deschamps, F., E. Kaminski, and P. J. Tackley (2011), A deep mantle origin for the primitive signature of ocean island basalt, *Nature Geosci.*, *4*(12), 879-882, doi:10.1038/Ngeo1295.

Dobson, D. P., and J. P. Brodholt (2005), Subducted banded iron formations as a source of ultralow-velocity zones at the core-mantle boundary, *Nature*, *434*(7031), 371-374, doi:10.1038/Nature03385.

Dziewonski, A. M., and D. L. Anderson (1981), Preliminary reference Earth model, *Physics of The Earth and Planetary Interiors*, *25*(4), 297-356, doi:10.1016/0031-9201(81)90046-7.

Dziewonski, A. M., V. Lekic, and B. A. Romanowicz (2010), Mantle Anchor Structure: An argument for bottom up tectonics, *Earth and Planetary Science Letters*, *299*(1-2), 69-79, doi:10.1016/j.epsl.2010.08.013.

Farnetani, C. G. (1997), Excess temperature of mantle plumes: The role of chemical stratification across D'', *Geophysical Research Letters*, *24*(13), 1583-1586, doi:10.1029/97gl01548.

Fei, Y., L. Zhang, A. Corgne, H. Watson, A. Ricolleau, Y. Meng, and V. Prakapenka (2007), Spin transition and equations of state of (Mg, Fe)O solid solutions, *Geophysical Research Letters*, *34*(17), doi:10.1029/2007gl030712.

Fitoussi, C., and B. Bourdon (2012), Silicon Isotope Evidence Against an Enstatite Chondrite Earth, *Science*, *335*(6075), 1477-1480, doi:10.1126/science.1219509.

Fujita, K., and M. Ogawa (2009), Basaltic accumulation instability and chaotic plate motion in the earliest mantle inferred from numerical experiments, *Journal of Geophysical Research-Solid Earth*, *114*, B10402, doi:10.1029/2008jb006222.

Garnero, E. J., and D. V. Helmberger (1996), Seismic detection of a thin laterally varying boundary layer at the base of the mantle beneath the central-Pacific, *Geophysical Research Letters*, *23*(9), 977-980, doi:10.1029/95gl03603.

Garnero, E. J., and A. K. McNamara (2008), Structure and Dynamics of Earth's Lower Mantle, *Science*, *320*(5876), 626-628, doi:10.1126/science.1148028.

Graham, D. W. (2002), Noble Gas Isotope Geochemistry of Mid-Ocean Ridge and Ocean Island Basalts: Characterization of Mantle Source Reservoirs, *Reviews in Mineralogy and Geochemistry*, *47*(1), 247-317, doi:10.2138/rmg.2002.47.8.

Hahm, D., P. R. Castillo, and D. R. Hilton (2009), A deep mantle source for high ^{3}He/^{4}He ocean island basalts (OIB) inferred from Pacific near-ridge seamount lavas, *Geophysical Research Letters*, *36*(20), L20316, doi:10.1029/2009gl040560.

Hart, S. R., and A. Zindler (1986), In search of a bulk-Earth composition, *Chemical Geology*, *57*(3‒4), 247-267, doi:10.1016/0009-2541(86)90053-7.

Hayden, L. A., and E. B. Watson (2007), A diffusion mechanism for core-mantle interaction, *Nature*, *450*(7170), 709-U706, doi:10.1038/Nature06380.

He, X., and M. D. Long (2011), Lowermost mantle anisotropy beneath the northwestern Pacific: Evidence from PcS, ScS, SKS, and SKKS phases, *Geochemistry Geophysics Geosystems*, *12*, Q12012, doi:10.1029/2011gc003779.

He, Y., and L. Wen (2009), Structural features and shear-velocity structure of the "Pacific Anomaly", *Journal of Geophysical Research*, *114*(B2), B02309, doi:10.1029/2008jb005814.

He, Y., and L. Wen (2011), Seismic velocity structures and detailed features of the D" discontinuity near the core-mantle boundary beneath eastern Eurasia, *Physics of The Earth and Planetary Interiors*(3-4), 176-184, doi:10.1016/j.pepi.2011.09.002.

He, Y., and L. Wen (2012), Geographic boundary of the "Pacific Anomaly" and its geometry and transitional structure in the north, *Journal of Geophysical Research*, *117*(B9), B09308, doi:10.1029/2012jb009436.

Helmberger, D., S. Ni, L. Wen, and J. Ritsema (2000), Seismic evidence for ultralow-velocity zones beneath Africa and eastern Atlantic, *Journal of Geophysical Research*, *105*(B10), 23865-23878, doi:10.1029/2000jb900143.

Hernlund, J. W., and A. M. Jellinek (2010), Dynamics and structure of a stirred partially molten ultralow-velocity zone, *Earth and Planetary Science Letters*, *296*(1-2), 1-8, doi:10.1016/j.epsl.2010.04.027.

Hernlund, J. W., and P. J. Tackley (2007), Some dynamical consequences of partial melting in Earth's deep mantle, *Physics of The Earth and Planetary Interiors*, *162*(1-2), 149-163, doi:10.1016/j.pepi.2007.04.005.

Hernlund, J. W., C. Thomas, and P. J. Tackley (2005), A doubling of the post-perovskite phase boundary and structure of the Earth's lowermost mantle, *Nature*, *434*(7035), 882-886, doi:10.1038/nature03472.

Hier-Majumder, S. (2008), Influence of contiguity on seismic velocities of partially molten aggregates, *Journal of Geophysical Research-Solid Earth*, *113*(B12), doi:10.1029/2008jb005662.

Hier-Majumder, S., and J. Revenaugh (2010), Relationship between the viscosity and topography of the ultralow-velocity zone near the core-mantle boundary, *Earth and Planetary Science Letters*, *299*(3-4), 382-386, doi:10.1016/j.epsl.2010.09.018.

Hirose, K., N. Takafuji, N. Sata, and Y. Ohishi (2005), Phase transition and density of subducted MORB crust in the lower mantle, *Earth and Planetary Science Letters*, *237*(1-2), 239-251, doi:10.1016/j.epsl.2005.06.035.

Hofmann, A. W. (1997), Mantle geochemistry: The message from oceanic volcanism, *Nature*, *385*(6613), 219-229, doi:10.1038/385219a0.

Hofmann, A. W., D. H. Heinrich, and K. T. Karl (2007), Sampling Mantle Heterogeneity through Oceanic Basalts: Isotopes and Trace Elements, in *Treatise on Geochemistry*, edited, pp. 1-44, Pergamon, Oxford.

Hofmann, A. W., and W. M. White (1982), Mantle Plumes from Ancient Oceanic-Crust, *Earth and Planetary Science Letters*, *57*(2), 421-436, doi:10.1016/0012-821x(82)90161-3.

Hunt, S. A., D. J. Weidner, L. Li, L. P. Wang, N. P. Walte, J. P. Brodholt, and D. P. Dobson (2009), Weakening of calcium iridate during its transformation from perovskite to post-perovskite, *Nature Geosci.*, *2*(11), 794-797, doi:10.1038/Ngeo663.

Irifune, T. (1987), An experimental investigation of the pyroxene-garnet transformation in a pyrolite composition and its bearing on the constitution of the mantle, *Physics of The Earth and Planetary Interiors*, *45*(4), 324-336, doi:10.1016/0031-9201(87)90040-9.

Irifune, T., T. Shinmei, C. A. McCammon, N. Miyajima, D. C. Rubie, and D. J. Frost (2010), Iron Partitioning and Density Changes of Pyrolite in Earth's Lower Mantle, *Science*, *327*(5962), 193-195, doi:10.1126/science.1181443.

Ishii, M., and J. Tromp (1999), Normal-mode and free-Air gravity constraints on lateral variations in velocity and density of Earth's mantle, *Science*, *285*(5431), 1231-1236, doi:10.1126/science.285.5431.1231.

Ishii, M., and J. Tromp (2004), Constraining large-scale mantle heterogeneity using mantle and inner-core sensitive normal modes, *Physics of The Earth and Planetary Interiors*, *146*(1-2), 113-124, doi:10.1016/j.pepi.2003.06.012.

Jellinek, A. M., and M. Manga (2004), Links between long-lived hot spots, mantle plumes, D ", and plate tectonics, *Reviews of Geophysics*, *42*(3), doi:10.1029/2003rg000144.

Kanda, R. V. S., and D. J. Stevenson (2006), Suction mechanism for iron entrainment into the lower mantle, *Geophysical Research Letters*, *33*(2), doi:10.1029/2005gl025009.

Kellogg, L. H., B. H. Hager, and R. D. van der Hilst (1999), Compositional Stratification in the Deep Mantle, *Science*, *283*(5409), 1881-1884, doi:10.1126/science.283.5409.1881.

Kito, T., S. Rost, C. Thomas, and E. J. Garnero (2007), New insights into the P- and S-wave velocity structure of the D " discontinuity beneath the Cocos plate, *Geophysical Journal International*, *169*(2), 631-645, doi:10.1111/j.1365-246X.2007.03350.x.

Knittle, E., and R. Jeanloz (1989), Simulating the core-mantle boundary: An experimental study of high-pressure reactions between silicates and liquid iron, *Geophysical Research Letters*, *16*(7), 609-612, doi:10.1029/GL016i007p00609.

Knittle, E., and R. Jeanloz (1991), Earth's Core-Mantle Boundary: Results of Experiments at High Pressures and Temperatures, *Science*, *251*(5000), 1438-1443, doi:10.1126/science.251.5000.1438.

Labrosse, S., J. W. Hernlund, and N. Coltice (2007), A crystallizing dense magma ocean at the base of the Earth's mantle, *Nature*, *450*(7171), 866-869, doi:10.1038/Nature06355.

Lay, T. (2008), Sharpness of the D " discontinuity beneath the Cocos Plate: Implications for the perovskite to post-perovskite phase transition, *Geophysical Research Letters*, *35*(3), doi:10.1029/2007GL032465.

Lay, T., J. Hernlund, and B. A. Buffett (2008), Core-mantle boundary heat flow, *Nature Geosci*, *1*(1), 25-32, doi:10.1038/Ngeo.2007.44.

Lay, T., J. Hernlund, E. J. Garnero, and M. S. Thorne (2006), A Post-Perovskite Lens and D" Heat Flux Beneath the Central Pacific, *Science*, *314*(5803), 1272-1276, doi:10.1126/science.1133280.

Lee, C. T. A., P. Luffi, T. Hoink, J. Li, R. Dasgupta, and J. Hernlund (2010), Upside-down differentiation and generation of a 'primordial' lower mantle, *Nature*, *463*(7283), 930-U102, doi:10.1038/Nature08824.

Li, M., and A. K. McNamara (2013), The difficulty for subducted oceanic crust to accumulate at the Earth's core-mantle boundary, *Journal of Geophysical Research*, *118*(4), 1807-1816, doi:10.1002/Jgrb.50156.

Li, M., A. K. McNamara, and E. J. Garnero (2014a), Chemical complexity of hotspots caused by cycling oceanic crust through mantle reservoirs, *Nature Geoscience*, *7*(5), 366-370, doi:10.1038/Ngeo2120.

Li, X. D., and B. Romanowicz (1996), Global mantle shear velocity model developed using nonlinear asymptotic coupling theory, *Journal of Geophysical Research-Solid Earth*, *101*(B10), 22245-22272, doi:10.1029/96JB01306.

Li, Y., F. Deschamps, and P. J. Tackley (2014b), Effects of low-viscosity post-perovskite on the stability and structure of primordial reservoirs in the lower mantle, *Geophysical Research Letters*, 2014GL061362, doi:10.1002/2014GL061362.

Lin, J.-F., S. Speziale, Z. Mao, and H. Marquardt (2013), EFFECTS OF THE ELECTRONIC SPIN TRANSITIONS OF IRON IN LOWER MANTLE MINERALS: IMPLICATIONS FOR DEEP MANTLE GEOPHYSICS AND GEOCHEMISTRY, *Reviews of Geophysics*, *51*(2), 244-275, doi:10.1002/rog.20010.

Lin, J.-F., G. Vanko, S. D. Jacobsen, V. Iota, V. V. Struzhkin, V. B. Prakapenka, A. Kuznetsov, and C.-S. Yoo (2007), Spin Transition Zone in Earth's Lower Mantle, *Science*, *317*(5845), 1740-1743, doi:10.1126/science.1144997.

Lin, J. F., V. V. Struzhkin, S. D. Jacobsen, M. Y. Hu, P. Chow, J. Kung, H. Liu, H. K. Mao, and R. J. Hemley (2005), Spin transition of iron in magnesiowustite in the Earth's lower mantle, *Nature*, *436*(7049), 377-380, doi:10.1038/nature03825.

Luo, S.-N., S. Ni, and D. V. Helmberger (2001), Evidence for a sharp lateral variation of velocity at the core-mantle boundary from multipathed PKPab, *Earth and Planetary Science Letters*, *189*(3-4), 155-164, doi:10.1016/S0012-821x(01)00364-8.

Lynner, C., and M. D. Long (2014), Lowermost mantle anisotropy and deformation along the boundary of the African LLSVP, *Geophysical Research Letters*, *41*(10), 3447-3454, doi:10.1002/2014gl059875.

Mao, W. L., H.-k. Mao, W. Sturhahn, J. Zhao, V. B. Prakapenka, Y. Meng, J. Shu, Y. Fei, and R. J. Hemley (2006), Iron-Rich Post-Perovskite and the Origin of Ultralow-Velocity Zones, *Science*, *312*(5773), 564-565, doi:10.1126/science.1123442.

Mao, W. L., et al. (2005), Iron-rich silicates in the Earth's D " layer, *Proceedings of the National Academy of Sciences of the United States of America*, *102*(28), 9751-9753, doi:10.1073/pnas.0503737102.

Masters, G., G. Laske, H. Bolton, and A. Dziewonski (2000), The relative behavior of shear veocity, bulk sound speed, and compressional velocity in the mantle: implications for chemical and thermal structure, in *Earth's Deep Interior: Mineral Physics and Tomography From the Atomic to the Global Scale*, edited by S. K. e. al., pp. 63-86, AGU Geophysical Monograph, Washington, D.C.

McDonough, W. F., and S. s. Sun (1995), The composition of the Earth, *Chemical Geology*, *120*(3‒4), 223-253, doi:10.1016/0009-2541(94)00140-4.

McKenzie, D., and M. J. Bickle (1988), The Volume and Composition of Melt Generated by Extension of the Lithosphere, *Journal of Petrology*, *29*(3), 625-679, doi:10.1093/petrology/29.3.625.

McNamara, A. K., E. J. Garnero, and S. Rost (2010), Tracking deep mantle reservoirs with ultra-low velocity zones, *Earth and Planetary Science Letters*, *299*(1-2), 1-9, doi:10.1016/j.epsl.2010.07.042.

McNamara, A. K., and S. Zhong (2004), Thermochemical structures within a spherical mantle: Superplumes or piles?, *Journal of Geophysical Research*, *109*(B7), B07402, doi:10.1029/2003jb002847.

McNamara, A. K., and S. Zhong (2005), Thermochemical structures beneath Africa and the Pacific Ocean, *Nature*, *437*(7062), 1136-1139, doi:10.1038/nature04066.

Merkel, S., A. K. McNamara, A. Kubo, S. Speziale, L. Miyagi, Y. Meng, T. S. Duffy, and H.-R. Wenk (2007), Deformation of (Mg,Fe)SiO3 Post-Perovskite and D" Anisotropy, *Science*, *316*(5832), 1729-1732, doi:10.1126/science.1140609.

Miller, M. S., and F. Niu (2008), Bulldozing the core-mantle boundary: Localized seismic scatterers beneath the Caribbean Sea, *Physics of The Earth and Planetary Interiors*, *170*(1-2), 89-94, doi:10.1016/j.pepi.2008.07.044.

Murakami, M., and J. Bass (2011), Evidence of denser MgSiO3 glass above 133 gigapascal (GPa) and implications for remnants of ultradense silicate melt from a deep magma ocean, *Proceedings of the National Academy of Sciences of the United States of America*, *108*(42), 17286-17295, doi:10.1073/pnas.1109748108.

Murakami, M., K. Hirose, K. Kawamura, N. Sata, and Y. Ohishi (2004), Post-Perovskite Phase Transition in MgSiO3, *Science*, *304*(5672), 855-858, doi:10.1126/science.1095932.

Nakagawa, T., and P. J. Tackley (2004), Effects of thermo-chemical mantle convection on the thermal evolution of the Earth's core, *Earth and Planetary Science Letters*, *220*(1-2), 107-119, doi:10.1016/S0012-821x(04)00055-X.

Nakagawa, T., and P. J. Tackley (2011), Effects of low-viscosity post-perovskite on thermo-chemical mantle convection in a 3-D spherical shell, *Geophysical Research Letters*, *38*(4), L04309, doi:10.1029/2010gl046494.

Nakagawa, T., and P. J. Tackley (2014), Influence of combined primordial layering and recycled MORB on the coupled thermal evolution of Earth's mantle and core, *Geochemistry, Geophysics, Geosystems*, *15*(3), 619-633, doi:10.1002/2013GC005128.

Nakagawa, T., P. J. Tackley, F. Deschamps, and J. A. D. Connolly (2010), The influence of MORB and harzburgite composition on thermo-chemical mantle convection in a 3-D spherical shell with self-consistently calculated mineral physics, *Earth and Planetary Science Letters*, *296*(3-4), 403-412, doi:10.1016/j.epsl.2010.05.026.

Ni, S., E. Tan, M. Gurnis, and D. Helmberger (2002), Sharp Sides to the African Superplume, *Science*, *296*(5574), 1850-1852, doi:10.1126/science.1070698.

Niu, F., and L. Wen (2001), Strong seismic scatterers near the core-mantle boundary west of Mexico, *Geophysical Research Letters*, *28*(18), 3557-3560, doi:10.1029/2001gl013270.

Nomura, R., K. Hirose, K. Uesugi, Y. Ohishi, A. Tsuchiyama, A. Miyake, and Y. Ueno (2014), Low Core-Mantle Boundary Temperature Inferred from the Solidus of Pyrolite, *Science*, *343*(6170), 522-525, doi:10.1126/science.1248186.

Nomura, R., H. Ozawa, S. Tateno, K. Hirose, J. Hernlund, S. Muto, H. Ishii, and N. Hiraoka (2011), Spin crossover and iron-rich silicate melt in the Earth's deep mantle, *Nature*, *473*(7346), 199-202, doi:10.1038/Nature09940.

Nowacki, A., J. Wookey, and J. M. Kendall (2010), Deformation of the lowermost mantle from seismic anisotropy, *Nature*, *467*(7319), 1091-1094, doi:10.1038/nature09507.

O'Neill, H. S. C. (1991), The origin of the moon and the early history of the earth—A chemical model. Part 2: The earth, *Geochimica et Cosmochimica Acta*, *55*(4), 1159-1172, doi:10.1016/0016-7037(91)90169-6.

Oganov, A. R., and S. Ono (2004), Theoretical and experimental evidence for a post-perovskite phase of MgSiO3 in Earth's D" layer, *Nature*, *430*(6998), 445-448, doi:10.1038/Nature02701.

Ogawa, M. (2010), Variety of plumes and the fate of subducted basaltic crusts, *Physics of The Earth and Planetary Interiors*, *183*(1-2), 366-375, doi:10.1016/j.pepi.2010.05.001.

Ohta, K., K. Hirose, T. Lay, N. Sata, and Y. Ohishi (2008), Phase transitions in pyrolite and MORB at lowermost mantle conditions: Implications for a MORB-rich pile above the core-mantle boundary, *Earth and Planetary Science Letters*, *267*(1-2), 107-117, doi:10.1016/j.epsl.2007.11.037.

Ohtani, E., and M. Maeda (2001), Density of basaltic melt at high pressure and stability of the melt at the base of the lower mantle, *Earth and Planetary Science Letters*, *193*(1), 69-144, doi:10.1016/S0012-821x(01)00505-2.

Otsuka, K., and S. Karato (2012), Deep penetration of molten iron into the mantle caused by a morphological instability, *Nature*, *492*(7428), 243-246, doi:10.1038/nature11663.

Revenaugh, J., and R. Meyer (1997), Seismic Evidence of Partial Melt Within a Possibly Ubiquitous Low-Velocity Layer at the Base of the Mantle, *Science*, *277*(5326), 670-673, doi:10.1126/science.277.5326.670.

Ricolleau, A., et al. (2009), Density profile of pyrolite under the lower mantle conditions, *Geophysical Research Letters*, *36*(6), L06302, doi:10.1029/2008gl036759.

Ringwood, A. E. (1962), A model for the upper mantle, *Journal of Geophysical Research*, *67*(2), 857-867, doi:10.1029/JZ067i002p00857.

Ringwood, A. E. (1982), Phase-Transformations and Differentiation in Subducted Lithosphere - Implications for Mantle Dynamics, Basalt Petrogenesis, and Crustal Evolution, *Journal of Geology*, *90*(6), 611-643, doi:10.1086/628721.

Ringwood, A. E. (1991), Phase-Transformations and Their Bearing on the Constitution and Dynamics of the Mantle, *Geochimica et Cosmochimica Acta*, *55*(8), 2083-2110, doi:10.1016/0016-7037(91)90090-R.

Ritsema, J., A. Deuss, H. J. van Heijst, and J. H. Woodhouse (2011), S40RTS: a degree-40 shear-velocity model for the mantle from new Rayleigh wave dispersion, teleseismic traveltime and normal-mode splitting function measurements, *Geophysical Journal International*, *184*(3), 1223-1236, doi:10.1111/j.1365-246X.2010.04884.x.

Romanowicz, B. (2003), Global mantle tomography: Progress status in the past 10 years, *Annual Review of Earth and Planetary Sciences*, *31*, 303-328, doi:10.1146/annurev.earth.31.091602.113555.

Rondenay, S., and K. M. Fischer (2003), Constraints on localized core-mantle boundary structure from multichannel, broadband SKS coda analysis, *Journal of Geophysical Research*, *108*(B11), 2537, doi:10.1029/2003jb002518.

Ross, A. R., H. Thybo, and L. N. Solidilov (2004), Reflection seismic profiles of the core-mantle boundary, *Journal of Geophysical Research*, *109*(B8), B08303, doi:10.1029/2003jb002515.

Rost, S., and P. S. Earle (2010), Identifying regions of strong scattering at the core-mantle boundary from analysis of PKKP precursor energy, *Earth and Planetary Science Letters*, *297*(3-4), 616-626, doi:10.1016/j.epsl.2010.07.014.

Rost, S., E. J. Garnero, and Q. Williams (2006), Fine-scale ultralow-velocity zone structure from high-frequency seismic array data, *Journal of Geophysical Research*, *111*(B9), B09310, doi:10.1029/2005jb004088.

Rost, S., E. J. Garnero, Q. Williams, and M. Manga (2005), Seismological constraints on a possible plume root at the core-mantle boundary, *Nature*, *435*(7042), 666-669, doi:10.1038/Nature03620.

Rost, S., and J. Revenaugh (2003), Small-scale ultralow-velocity zone structure imaged by ScP, *Journal of Geophysical Research*, *108*(B1), 2056, doi:10.1029/2001jb001627.

Samuel, H., and C. G. Farnetani (2003), Thermochemical convection and helium concentrations in mantle plumes, *Earth and Planetary Science Letters*, *207*(1-4), 39-56, doi:10.1016/S0012-821x(02)01125-1.

Schubert, G., G. Masters, P. Olson, and P. Tackley (2004), Superplumes or plume clusters?, *Physics of The Earth and Planetary Interiors*, *146*(1-2), 147-162, doi:10.1016/j.pepi.2003.09.025.

Shang, X., S.-H. Shim, M. de Hoop, and R. van der Hilst (2014), Multiple seismic reflectors in Earth's lowermost mantle, *Proceedings of the National Academy of Sciences*, *111*(7), 2442-2446, doi:10.1073/pnas.1312647111.

Shim, S.-H. (2008), The Postperovskite Transition, *Annual Review of Earth and Planetary Sciences*, *36*(1), 569-599, doi:10.1146/annurev.earth.36.031207.124309.

Solomatov, V. S. (2000), Fluid dynamics of a terrestrial magma ocean, *In Origin of the Earth and Moon (ed. R. Canup and K. Righter)*, 323-338.

Solomatov, V. S. (2007), Magma oceans and primordial mantle differentiation, *Treatise on Geophysics*, 91-119.

Steinbach, V., and D. A. Yuen (1999), Viscous heating: a potential mechanism for the formation of the ultralow velocity zone, *Earth and Planetary Science Letters*, *172*(3–4), 213-220, doi:10.1016/S0012-821X(99)00205-8.

Stixrude, L., and C. Lithgow-Bertelloni (2011), Thermodynamics of mantle minerals – II. Phase equilibria, *Geophysical Journal International*, *184*(3), 1180-1213, doi:10.1111/j.1365-246X.2010.04890.x.

Stixrude, L., and C. Lithgow-Bertelloni (2012), Geophysics of Chemical Heterogeneity in the Mantle, *Annual Review of Earth and Planetary Sciences*, *40*(1), 569-595, doi:10.1146/annurev.earth.36.031207.124244.

Su, W. J., and A. M. Dziewonski (1997), Simultaneous inversion for 3-D variations in shear and bulk velocity in the mantle, *Physics of The Earth and Planetary Interiors*, *100*(1-4), 135-156, doi:10.1016/S0031-9201(96)03236-0.

Su, W. J., R. L. Woodward, and A. M. Dziewonski (1994), Degree-12 Model of Shear Velocity Heterogeneity in the Mantle, *Journal of Geophysical Research-Solid Earth*, *99*(B4), 6945-6980, doi:10.1029/93JB03408.

Sun, D., D. V. Helmberger, J. M. Jackson, R. W. Clayton, and D. J. Bower (2013), Rolling hills on the core‐mantle boundary, *Earth and Planetary Science Letters*, *361*(0), 333-342, doi:10.1016/j.epsl.2012.10.027.

Sun, D., E. Tan, D. Helmberger, and M. Gurnis (2007a), Seismological support for the metastable superplume model, sharp features, and phase changes within the lower mantle, *Proceedings of the National Academy of Sciences of the United States of America*, *104*(22), 9151-9155, doi:10.1073/pnas.0608160104.

Sun, S.-S. (1982), Chemical composition and origin of the earth's primitive mantle, *Geochimica et Cosmochimica Acta*, *46*(2), 179-192, doi:10.1016/0016-7037(82)90245-9.

Sun, X., X. Song, S. Zheng, and D. V. Helmberger (2007b), Evidence for a chemical-thermal structure at base of mantle from sharp lateral P-wave variations beneath Central America, *Proc Natl Acad Sci U S A*, *104*(1), 26-30, doi:10.1073/pnas.0609143103.

Tackley, P. (1998), Three-Dimensional Simulations of Mantle Convection with a Thermo-Chemical Basal Boundary Layer: D"?, *AGU Geophysical Mongraph on the CMB ed. M. Gurnis*.

Tackley, P. J. (2007), Mantle Geochemical Geodynamics, in *Treatise on Geophysics*, edited by D. Bercovici, pp. 437‐505, Elsevier.

Tackley, P. J., and S. X. Xie (2002), The thermochemical structure and evolution of Earth's mantle: constraints and numerical models, *Philosophical Transactions of the Royal Society of London Series a-Mathematical Physical and Engineering Sciences*, *360*(1800), 2593-2609, doi:10.1098/rsta.2002.1082.

Takafuji, N., K. Hirose, M. Mitome, and Y. Bando (2005), Solubilities of O and Si in liquid iron in equilibrium with (Mg,Fe)SiO3 perovskite and the light elements in the core, *Geophysical Research Letters*, *32*(6), L06313, doi:10.1029/2005gl022773.

Tan, E., and M. Gurnis (2005), Metastable superplumes and mantle compressibility, *Geophysical Research Letters*, *32*(20), L20307, doi:10.1029/2005GL024190.

Tan, E., and M. Gurnis (2007), Compressible thermochemical convection and application to lower mantle structures, *Journal of Geophysical Research*, *112*(B6), B06304, doi:10.1029/2006JB004505.

Taylor, S. R. (1964), Chondritic Earth Model, *Nature*, *202*(4929), 281-282, doi:10.1038/202281a0.

To, A., Y. Fukao, and S. Tsuboi (2011), Evidence for a thick and localized ultra low shear velocity zone at the base of the mantle beneath the central Pacific, *Physics of The Earth and Planetary Interiors*, *184*(3-4), 119-133, doi:10.1016/j.pepi.2010.10.015.

To, A., B. Romanowicz, Y. Capdeville, and N. Takeuchi (2005), 3D effects of sharp boundaries at the borders of the African and Pacific Superplumes: Observation and modeling, *Earth and Planetary Science Letters*, *233*(1-2), 137-153, doi:10.1016/j.epsl.2005.01.037.

Tonks, W. B., and H. J. Melosh (1993), Magma ocean formation due to giant impacts, *Journal of Geophysical Research: Planets*, *98*(E3), 5319-5333, doi:10.1029/92JE02726.

Torsvik, T. H., K. Burke, B. Steinberger, S. J. Webb, and L. D. Ashwal (2010), Diamonds sampled by plumes from the core-mantle boundary, *Nature*, *466*(7304), 352-355, doi:10.1038/nature09216.

Torsvik, T. H., R. van der Voo, P. V. Doubrovine, K. Burke, B. Steinberger, L. D. Ashwal, R. G. Tronnes, S. J. Webb, and A. L. Bull (2014), Deep mantle structure as a reference frame for movements in and on the Earth, *Proceedings of the National Academy of Sciences*, *111*(24), 8735-8740, doi:10.1073/pnas.1318135111.

Touboul, M., T. Kleine, B. Bourdon, H. Palme, and R. Wieler (2007), Late formation and prolonged differentiation of the Moon inferred from W isotopes in lunar metals, *Nature*, *450*(7173), 1206-1209, doi:10.1038/nature06428.

Trampert, J., F. Deschamps, J. Resovsky, and D. Yuen (2004), Probabilistic Tomography Maps Chemical Heterogeneities Throughout the Lower Mantle, *Science*, *306*(5697), 853-856, doi:10.1126/science.1101996.

Tsuchiya, T., J. Tsuchiya, K. Umemoto, and R. M. Wentzcovitch (2004), Phase transition in MgSiO3 perovskite in the earth's lower mantle, *Earth and Planetary Science Letters*, *224*(3-4), 241-248, doi:10.1016/j.epsl.2004.05.017.

van der Hilst, R. D., M. V. de Hoop, P. Wang, S. H. Shim, P. Ma, and L. Tenorio (2007), Seismostratigraphy and Thermal Structure of Earth's Core-Mantle Boundary Region, *Science*, *315*(5820), 1813-1817, doi:10.1126/science.1137867.

Walker, A. M., A. M. Forte, J. Wookey, A. Nowacki, and J. M. Kendall (2011), Elastic anisotropy of D" predicted from global models of mantle flow, *Geochemistry Geophysics Geosystems*, *12*(10), Q10006, doi:10.1029/2011gc003732.

Wang, Y., and L. Wen (2007a), Complex seismic anisotropy at the border of a very low velocity province at the base of the Earth's mantle, *Journal of Geophysical Research*, *112*(B9), B09305, doi:10.1029/2006jb004719.

Wen, L. (2006), A compositional anomaly at the Earth's core-mantle boundary as an anchor to the relatively slowly moving surface hotspots and as source to the DUPAL anomaly, *Earth and Planetary Science Letters*, *246*(1-2), 138-148, doi:10.1016/j.epsl.2006.04.024.

Wen, L., and D. V. Helmberger (1998a), A two-dimensional P-SV hybrid method and its application to modeling localized structures near the core-mantle boundary, *Journal of Geophysical Research*, *103*(B8), 17901-17918, doi:10.1029/98jb01276.

Wen, L., and D. V. Helmberger (1998b), Ultra-Low Velocity Zones Near the Core-Mantle Boundary from Broadband PKP Precursors, *Science*, *279*(5357), 1701-1703, doi:10.1126/science.279.5357.1701.

Wicks, J. K., J. M. Jackson, and W. Sturhahn (2010), Very low sound velocities in iron-rich (Mg,Fe)O: Implications for the core-mantle boundary region, *Geophysical Research Letters*, *37*, doi:10.1029/2010gl043689.

Williams, Q., and E. J. Garnero (1996), Seismic Evidence for Partial Melt at the Base of Earth's Mantle, *Science*, *273*(5281), 1528-1530, doi:10.1126/science.273.5281.1528.

Wookey, J., S. Stackhouse, J. M. Kendall, J. Brodholt, and G. D. Price (2005), Efficacy of the post-perovskite phase as an explanation for lowermost-mantle seismic properties, *Nature*, *438*(7070), 1004-1007, doi:10.1038/nature04345.

Wu, Z., and R. M. Wentzcovitch (2014), Spin crossover in ferropericlase and velocity heterogeneities in the lower mantle, *Proceedings of the National Academy of Sciences*, *111*(29), 10468-10472, doi:10.1073/pnas.1322427111.

Yamazaki, D., T. Yoshino, H. Ohfuji, J.-i. Ando, and A. Yoneda (2006), Origin of seismic anisotropy in the D" layer inferred from shear deformation experiments on post-perovskite phase, *Earth and Planetary Science Letters*, *252*(3-4), 372-378, doi:10.1016/j.epsl.2006.10.004.

Zhang, N., S. Zhong, W. Leng, and Z.-X. Li (2010), A model for the evolution of the Earth's mantle structure since the Early Paleozoic, *Journal of Geophysical Research*, *115*(B6), doi:10.1029/2009jb006896.

Zhong, S. J. (2006), Constraints on thermochemical convection of the mantle from plume heat flux, plume excess temperature, and upper mantle temperature, *Journal of Geophysical Research-Solid Earth*, *111*(B4), doi:10.1029/2005jb003972.

CHAPTER 2

GOVERNING EQUATIONS AND NUMERICAL METHOD

We perform numerical calculations to study the nature of mantle convection by solving the equations of conservation of mass, momentum and energy under the Boussinesq approximation. In this chapter, I describe these equations first and give a brief introduction of numerical methods to solve these equations.

The equation for conservation of mass is:

$$\frac{\partial \rho}{\partial t} + \nabla \cdot \left(\rho \vec{V} \right) = 0 \tag{2.1}$$

or

$$\frac{D\rho}{Dt} + \rho \nabla \cdot \vec{V} = 0 \tag{2.2}$$

where $\frac{D}{Dt}$ is the material derivative, ρ is density, t is time, $\vec{V}$ is velocity.

For incompressible fluid, particles have constant density and $\frac{D\rho}{Dt} = 0$. The equation for conservation of mass becomes:

$$\nabla \cdot \vec{V} = 0 \tag{2.3}$$

The equation for conservation of momentum is:

$$\rho \left(\frac{\partial \vec{V}}{\partial t} + (\vec{V} \cdot \nabla)\vec{V} \right) = -\nabla \cdot \bar{\bar{\sigma}} + \rho g \hat{z} \tag{2.4}$$

where $\bar{\bar{\sigma}}$ is stress tensor and g is gravitational acceleration, and $\hat{z}$ is unit vector in vertical direction.

The stress tensor could be constructed by adding pressure P with a deviatoric stress tensor, $\bar{\bar{\tau}}$:

$$\bar{\bar{\sigma}} = \bar{\bar{\tau}} + P \tag{2.5}$$

Plug Eq. (2.5) into Eq. (2.4), the equation for conservation of momentum becomes:

$$\rho\left(\frac{\partial \vec{V}}{\partial t} + (\vec{V} \cdot \nabla)\vec{V}\right) = -\nabla \cdot \bar{\bar{\tau}} - \nabla P + \rho g \hat{z} \tag{2.6}$$

where the deviatoric stress is caused by viscous forces. Its value is proportional to strain rate for Newtonian material:

$$\bar{\bar{\tau}} = -\eta \bar{\bar{\dot{\varepsilon}}} \tag{2.7}$$

where η is viscosity and $\bar{\bar{\dot{\varepsilon}}}$ is strain rate tensor. The negative sign on the right part of Eq. (2.7) is due to our convection of defining direction of compression as the positive direction of normal stress.

Plug Eq. (2.7) into Eq. (2.6), the equation for conservation of momentum becomes:

$$\rho\left(\frac{\partial \vec{V}}{\partial t} + (\vec{V} \cdot \nabla)\vec{V}\right) = -\nabla P + \nabla \cdot \eta \bar{\bar{\dot{\varepsilon}}} + \rho g \hat{z} \tag{2.8}$$

Next, let's further simplify Eq. (2.8). The pressure, density and gravitational acceleration could be written as the summation of a reference value and the deviatoric value:

$$P = P_R + \tilde{P} \tag{2.9}$$

$$\rho = \rho_R + \tilde{\rho} \tag{2.10}$$

$$g = g_R + \tilde{g} \tag{2.11}$$

where P_R, ρ_R, and g_R are reference values for pressure, density and gravitational acceleration based on hydrostatic compression, and $\tilde{P}$, $\tilde{\rho}$, and $\tilde{g}$ are deviatoric pressure, density and gravitational acceleration from the reference values.

Notice that P_R, ρ_R, and g_R are not independent but relate to each other by:

$$\nabla P_R = \rho_R g_R \hat{z} \tag{2.12}$$

Plug Eq. (2.9)-Eq. (2.11) into Eq. (2.8), and take into account Eq. (2.12), the equation for conservation of momentum becomes:

$$\rho \left(\frac{\partial \vec{V}}{\partial t} + (\vec{V} \cdot \nabla)\vec{V} \right) = -\nabla \tilde{P} + \nabla \cdot \eta \bar{\bar{\varepsilon}} + \tilde{\rho} g_R \hat{z} + \rho_R \tilde{g} \hat{z} + \tilde{\rho} \tilde{g} \hat{z} \tag{2.13}$$

Assuming $\tilde{g} \approx 0$ and $g = g_R$ (anomaly of gravitational acceleration is small enough), we can further simplify Eq. (2.13) to:

$$\rho \left(\frac{\partial \vec{V}}{\partial t} + (\vec{V} \cdot \nabla)\vec{V} \right) = -\nabla \tilde{P} + \nabla \cdot \eta \bar{\bar{\varepsilon}} + \tilde{\rho} g \hat{z} \tag{2.14}$$

The conservation of energy is given as follows:

$$\rho \frac{Dq}{Dt} = \nabla \cdot (k \nabla T) + \rho H + \phi \tag{2.15}$$

where q is heat flow, k is thermal conductivity, T is temperature, H is heat production rate, and ϕ is viscous heating.

Using thermodynamics, heat flow q can be written as:

$$dq = TdS \tag{2.16}$$

and

$$dS = \frac{C_p}{T} dT - \frac{\alpha}{\rho} dP \tag{2.17}$$

where S is entropy, α is thermal expansivity, and C_p is heat capacity.

Plug Eq. (2.16) and Eq. (2.17) into Eq. (2.15), the equation for conservation of energy becomes:

$$\rho C_p \frac{DT}{Dt} - \alpha T \frac{DP}{Dt} = \rho C_p \nabla \cdot (\kappa \nabla T) + \rho H + \phi \tag{2.18}$$

where κ is thermal diffusivity.

Remember, $P = P_R + \tilde{P}$, then

$$\frac{DP}{Dt} = \frac{DP_R}{Dt} + \frac{D\tilde{P}}{Dt} = \frac{\partial P_R}{\partial t} + V_z \frac{\partial P_R}{\partial z} + \frac{D\tilde{P}}{Dt} \tag{2.19}$$

In Eq. (2.19), P_R is the reference pressure, which is independent of time. Thus,

$$\frac{\partial P_R}{\partial t} = 0 \tag{2.20}$$

In addition,

$$\frac{\partial P_R}{\partial z} = \rho_R g \tag{2.21}$$

Plug Eq. (2.20)-Eq. (2.21) into Eq. (2.19), we get:

$$\frac{DP}{Dt} = V_z \rho_R g + \frac{D\tilde{P}}{Dt} \tag{2.22}$$

Plug Eq. (2.22) into Eq. (2.18), the equation for conservation of energy becomes:

$$\rho C_p \frac{DT}{Dt} - \alpha T \left(V_z \rho_R g + \frac{D\tilde{P}}{Dt} \right) = \rho C_p \nabla \cdot (\kappa \nabla T) + \rho H + \phi \tag{2.23}$$

In summary, the equations for conservation of mass, momentum and energy for incompressible fluid are:

$$\nabla \cdot \vec{V} = 0 \tag{2.24}$$

$$\rho \left(\frac{\partial \vec{V}}{\partial t} + (\vec{V} \cdot \nabla) \vec{V} \right) = -\nabla \tilde{P} + \nabla \cdot \eta \bar{\bar{\varepsilon}} + \tilde{\rho} g \hat{z} \tag{2.25}$$

$$\rho C_p \frac{DT}{Dt} - \alpha T \left(V_z \rho_R g + \frac{D\tilde{P}}{Dt} \right) = \rho C_p \nabla \cdot (\kappa \nabla T) + \rho H + \phi \tag{2.26}$$

Let's non-dimensionalize Eq. (2.24)-Eq. (2.26) using:

$$\rho = \rho_0 \rho' \tag{2.27}$$

$$\alpha = \alpha_0 \alpha' \tag{2.28}$$

$$g = g_0 g' \tag{2.29}$$

$$\kappa = \kappa_0 \kappa' \tag{2.30}$$

$$\eta = \eta_0 \eta' \tag{2.31}$$

$$C_p = C_{p_0} C_p'\tag{2.32}$$

$$\vec{V} = \frac{\kappa_0}{D}\vec{V}'\tag{2.33}$$

$$T = \Delta T T'\tag{2.34}$$

$$H = \frac{\kappa_0}{D^2} C_{p_0} \Delta T H'\tag{2.35}$$

$$t = \frac{D^2}{\kappa_0} t'\tag{2.36}$$

$$\tilde{P} = \frac{\eta_0 \kappa_0}{D^2} P'\tag{2.37}$$

$$\nabla = \frac{1}{D}\nabla'\tag{2.38}$$

where ρ_0, α_0, g_0, κ_0, η_0, and C_{p_0} are reference density, reference thermal expansivity, reference gravity, reference thermal diffusivity, reference viscosity, and reference heat capacity, respectively. D is the thickness of the mantle, and ΔT is temperature difference between surface and the core-mantle boundary. Parameters with a prime are non-dimensional parameters.

Plug Eq. (2.27)-Eq. (2.38) into Eq. (2.24)-Eq. (2.26), we get:

$$\nabla' \cdot \vec{V}' = 0\tag{2.39}$$

$$\frac{1}{P_r}\rho'\left(\frac{\partial \vec{V}'}{\partial t} + (\vec{V}' \cdot \nabla')\vec{V}'\right) = -\nabla'P' + \nabla'\eta'\bar{\bar{\varepsilon}}' + \frac{D^3}{\eta_0 \kappa_0}\tilde{\rho}g\hat{z}\tag{2.40}$$

$$\rho'C_p'\frac{DT'}{Dt'} - \alpha'T'D_i\left(\frac{\alpha_0 \Delta T}{Ra}\frac{D\tilde{P}}{Dt} + \rho_R Vz\right) = \rho'C_p'\nabla' \cdot (\kappa'\nabla'T') + \rho'H' + \frac{D_i}{Ra}\phi'\tag{2.41}$$

where D_i is the dissipation number, which is defined as:

$$D_i = \frac{\alpha_0 g_0 D}{C_{p_0}}\tag{2.42}$$

The vigor of mantle convection is measured by Rayleigh number Ra, which is defined as follows:

$$Ra = \frac{\rho_0 g_0 \alpha_0 \Delta T D^3}{\eta_0 \kappa_0} \tag{2.43}$$

The Prandtl number P_r is defined as:

$$P_r = \frac{\eta_0}{\rho_0 \kappa_0} \tag{2.44}$$

The viscosity and thermal diffusivity of Earth's mantle are on the order of 1e22 and 1e-6, respectively. Given a density of Earth's mantle of 4000 kgm^{-3}, the Prandtl number P_r is on the order of 2.5e24, and the inverse of Prandtl number is almost infinite. Thus, the term on the left side of Eq. (2.40) which is the "inertia" of Earth's mantle can be removed. The equation of conservation of momentum becomes:

$$0 = -\nabla' P' + \nabla' \eta' \bar{\bar{\varepsilon}}' + \frac{D^3}{\eta_0 \kappa_0} \tilde{\rho} g \hat{z} \tag{2.45}$$

which is also called the stokes equation.

The density anomaly $\tilde{\rho}$ in Eq. (2.45) could be approximated as:

$$\tilde{\rho} = \Delta \rho C - \rho_0 \alpha_0 \Delta T T' \tag{2.46}$$

where $\Delta \rho$ is the density difference between different materials and C is the fraction of dense material.

Plug Eq. (2.46) into Eq. (2.45) and considering the definition of Rayleigh number Ra, the non-dimensional form of the equation for the conservation of momentum becomes:

$$0 = -\nabla' P' + \nabla'(\eta' \bar{\bar{\varepsilon}}') - Ra(T' - BC)\hat{z} \tag{2.47}$$

or

$$-\nabla' P' + \nabla'(\eta' \bar{\bar{\varepsilon}}') = Ra(T' - BC)\hat{z} \tag{2.48}$$

where, B is buoyancy number, which is defined as:

$$B = \frac{\Delta\rho}{\rho_0 \alpha_0 \Delta T} \tag{2.49}$$

The equations for conservation of mass, momentum and energy for incompressible fluid with infinite Prandtl number are:

$$\nabla' \cdot \vec{V}' = 0 \tag{2.50}$$

$$-\nabla'P' + \nabla'(\eta'\bar{\bar{\dot{\varepsilon}}}') = Ra(T' - BC)\hat{z} \tag{2.51}$$

$$\rho'C_p'\frac{DT'}{Dt'} - \alpha'T'D_i\left(\frac{\alpha_0\Delta T}{Ra}\frac{D\tilde{P}}{Dt} + \rho_R Vz\right) = \rho'C_p'\nabla' \cdot (\kappa'\nabla'T') + \rho'H' + \frac{D_i}{Ra}\phi' \tag{2.52}$$

Under the Boussinesq approximation, the Dissipation number is assumed to be zero. Thus, all the terms containing Dissipation number D_i in Eq. (2.52) are dropped. In addition, under the Boussinesq approximation, non-dimensional values of ρ', C_p' and κ' in Eq. (2.52) all equal to 1. The equations for conservation of mass, momentum and energy under the Boussinesq approximation becomes:

$$\nabla' \cdot \vec{V}' = 0 \tag{2.53}$$

$$-\nabla'P' + \nabla'(\eta'\bar{\bar{\dot{\varepsilon}}}') = Ra(T' - BC)\hat{z} \tag{2.54}$$

$$\frac{\partial T'}{\partial t'} + (\vec{V}' \cdot \nabla')T' = \nabla'^2 T' + H' \tag{2.55}$$

For convenience, we drop the prime in these equations for non-dimensional values and the non-dimensional form of these conservation equations under the Boussinesq becomes:

$$\nabla \cdot \vec{V} = 0 \tag{2.56}$$

$$-\nabla P + \nabla(\eta\bar{\bar{\dot{\varepsilon}}}) = Ra(T - BC)\hat{z} \tag{2.57}$$

$$\frac{\partial T}{\partial t} + (\vec{V} \cdot \nabla)T = \nabla^2 T + H \tag{2.58}$$

In this dissertation, we use the finite element code Citcom (a 2D code) [*Moresi and Solomatov*, 1995; *Moresi and Gurnis*, 1996] and CitcomCU (a 3D code) [*Zhong*, 2006] to solve these equations. In numerical modeling, the selection of geometry (2D or 3D), initial condition and boundary condition for solving these equations and the chosen of physical parameters, such as viscosity and Rayleigh number, are all based on the nature of the scientific questions we want to answer and the specific mantle dynamics we want to understand. The details of numerical method for understanding the thermochemical structure and dynamics of Earth's lowermost mantle are described in Chapter 3, 4 and 5.

References

Moresi, L., and M. Gurnis (1996), Constraints on the lateral strength of slabs from three-dimensional dynamic flow models, *Earth and Planetary Science Letters*, *138*(1-4), 15-28, doi:10.1016/0012-821x(95)00221-W.

Moresi, L. N., and V. S. Solomatov (1995), Numerical Investigation of 2d Convection with Extremely Large Viscosity Variations, *Physics of Fluids*, *7*(9), 2154-2162, doi:10.1063/1.868465.

Zhong, S. J. (2006), Constraints on thermochemical convection of the mantle from plume heat flux, plume excess temperature, and upper mantle temperature, *Journal of Geophysical Research-Solid Earth*, *111*(B4), doi:10.1029/2005jb003972.

CHAPTER 3

THE DIFFICULTY FOR SUBDUCTED OCEANIC CRUST TO ACCUMULATE AT

THE EARTH'S CORE-MANTLE BOUNDARY

3.1 Abstract

Seismic tomography has revealed two large low shear velocity provinces (LLSVPs) in the lowermost mantle beneath the central Pacific and Africa. The LLSVPs are further shown to be compositionally different from their surroundings. Among several hypotheses put forth in recent years to explain the cause of the LLSVPs, one postulates that they are thermochemical piles caused by accumulation of subducted oceanic crust at the core-mantle boundary (CMB). Mineral physics experiments indicate that oceanic crust becomes denser than surrounding mantle at lower mantle pressures. In addition, seismic observations provide evidence of subducted slabs arriving at the CMB. However, a major question pertains to whether subducted oceanic crust can survive viscous stirring associated with mantle plumes and accumulate into piles with the same spatial scale as LLSVPs. We perform a set of high resolution convection calculations to examine this hypothesis by investigating the interaction of thin oceanic crust (6 km) with mantle plumes. Our results show that as subducted oceanic crust is swept toward upwelling plume regions, the majority of it is viscously stirred into surrounding mantle. Only a

small amount of oceanic crust may accumulate at the base of plumes, but it is consistently entrained away into the plume at a rate equal to or greater than it is accumulated. We find that it is difficult for subducted oceanic crust to accumulate into large thermochemical piles at the CMB.

3.2 Introduction

Understanding the role that compositional heterogeneity plays in controlling mantle dynamics, and therefore heat transport and thermal evolution, remains one of the most challenging problems in Earth Science. A critical question relates to the origin and dynamic nature of proposed large-scale compositional heterogeneity in Earth's lower mantle. Although it has long been proposed that the lowermost mantle of the Earth is compositionally heterogeneous on a global scale [*Masters et al.*, 2000; *Trampert et al.*, 2004], the cause of this heterogeneity and how it affects mantle dynamics is not well understood.

Seismic tomography studies have discovered the existence of two large low shear velocity provinces (LLSVPs) in the lowermost mantle beneath the central Pacific and Africa [*Li and Romanowicz*, 1996; *Su and Dziewonski*, 1997; *Grand*, 2002; *Ritsema et al.*, 2004]. These are regions furthest removed from paleosubduction, and geodynamical studies have revealed that Earth's subduction history should act to drive upwellings in these regions [*Bunge et al.*, 1998; *Zhong et al.*, 2000; *McNamara and Zhong*, 2005]. The two LLSVP anomalies beneath Africa and central Pacific are both of large size. As demonstrated in recent seismic studies, the African anomaly maybe a single massive pile reaching 1300 km above the CMB, and the Pacific anomaly may contain several piles whose height ranges from ~400 km to at least 740 km [*Wang and Wen*, 2007b; *He and*

Wen, 2009; 2012]. Interestingly, paleo-magnetic constraints infer that the LLSVPs may have been in their current locations for several hundred million years [*Torsvik et al.*, 2010]. The LLSVPs are also characterized by increased density [*Ishii and Tromp*, 1999; *Trampert et al.*, 2004], large $dlnVs/dlnVp$ ratio [*Wang and Wen*, 2007b] and anti-correlation between seismic shear velocity and bulk sound speed [*Trampert et al.*, 2004]. In addition, seismic travel-time and waveform studies indicate sharp edges [*Wen et al.*, 2001; *Wen*, 2001] and large contrasts in elastic properties within the LLSVP regions, particularly along the margins [*Ni et al.*, 2002; *Ni and Helmberger*, 2003; *Wang and Wen*, 2004; *To et al.*, 2005; *Ford et al.*, 2006; *He and Wen*, 2009].

The characteristics of the LLSVPs discussed above suggest that their composition is different from that of the background mantle [*Ishii and Tromp*, 1999; *Masters et al.*, 2000; *Trampert et al.*, 2004; *Hernlund and Houser*, 2008]. Possible origins for a distinct composition of LLSVPs may include (1) products resulting from interaction between mantle and core [*Buffett et al.*, 2000; *Kanda and Stevenson*, 2006], (2) remnants of primordial dense reservoirs formed by differentiation in Earth's early history [*Wen et al.*, 2001; *Wen*, 2001; *Labrosse et al.*, 2007; *Lee et al.*, 2010; *Nomura et al.*, 2011] and (3) accumulation of subducted oceanic crust at the CMB [*Christensen and Hofmann*, 1994; *Brandenburg and van Keken*, 2007; *Nakagawa et al.*, 2009; *Tackley*, 2011]. Each of these possibilities is related to different dynamics and Earth's chemical evolution [*Wen et al.*, 2001; *Wen*, 2001; *Garnero and McNamara*, 2008; *Tackley*, 2012].

In this study, we test the third possibility using numerical modeling. Seismic tomography shows that subducted lithosphere is able to reach the lowermost mantle [*Grand et al.*, 1997; *Li et al.*, 2008]. In addition, mineral physics experiments indicate

50

that oceanic crust becomes denser than surrounding mantle at lower mantle pressures [*Hirose et al.*, 2005]. Furthermore, geodynamical experiments reveal that oceanic crust can delaminate from oceanic lithosphere in the lowermost mantle [*Tackley*, 2011]. However, an important question is whether subducted oceanic crust can survive vigorous stirring associated with mantle plumes and accumulate into large thermochemical piles with the same spatial scale as LLSVPs. The fact that oceanic crust becomes denser than surrounding mantle at lower mantle pressures would support this idea; however, because oceanic crust is so thin compared to mantle-scale convection, it may not be able to survive viscous stirring (i.e., viscous forces dominate buoyancy forces). We investigate this question here by performing high resolution mantle convection calculations that include realistic, 6 km, crustal thickness. We investigate whether oceanic crust can accumulate in significant quantities in upwelling plume regions over billion-year timescales.

Previous numerical calculations have been conducted to explore the possibility of subducted oceanic crust to accumulate at the CMB [*Christensen and Hofmann*, 1994; *Brandenburg and van Keken*, 2007; *Huang and Davies*, 2007; *Nakagawa et al.*, 2009; *Tackley*, 2011]. *Christensen and Hofmann* [1994] modeled the process of segregation and accumulation of subducted oceanic crust at the CMB. They found that of the order of 1/6 of the subducted oceanic crust accumulated in pools at the bottom of the model, which resides underneath thermal plumes. In their study, the thickness of oceanic crust is about 30 km and the Rayleigh number is moderately low because of computational limitation. Later, *Brandenburg and van Keken* [2007] expanded the results of *Christensen and Hofmann* [1994] by studying models with more Earth-like vigor. Their results show that

51

significant accumulation is still possible at high Rayleigh number, but only when the excess density of oceanic crust in the lower mantle is larger than that currently suggested from laboratory experiments. *Huang and Davies* [2007] showed the ability of subducted oceanic crust to accumulate at the CMB using 3D calculations in which the mantle is only heated within and zero heat flux is employed at the CMB. As a result, plumes are suppressed in their study. By incorporating self-consistently calculated mineral physics into mantle convection models, *Nakagawa et al.* [2009] found that a large amount of subducted dense materials accumulate at the CMB. However, they state that they assume more MORB material in the petrological model, which explains why their calculations produce a much thicker layer of segregated MORB above the CMB. Most recently, *Tackley* [2011] simulated the process of segregating subducted oceanic crust from a compositionally-stratified slab in both two-dimensional (2-D) and three-dimensional (3-D) models. The results show that a large fraction of subducted oceanic crust can segregate and remain at the CMB if a primordial dense layer exists at the lowermost mantle. However, the thickness of oceanic crust in his study is 30 km.

It is not understood whether realistic thin 6 km oceanic crust could survive vigorous entrainment from plumes and accumulate into large piles at the CMB. In this study, we test the possibility of accumulating large amount of subducted oceanic crust at CMB in the existence of upwelling plumes. Our calculations are featured by high resolution which allows us to study the subduction and accumulation of a realistic thin oceanic crust (6 km).

3.3 Method

We conducted geodynamic calculations by solving the following non-dimensional equations for conservation of mass, momentum, and energy using Boussinesq approximation:

$$\nabla \cdot \vec{u} = 0 \tag{3.1}$$

$$-\nabla P + \nabla(\eta \bar{\bar{\varepsilon}}) = Ra(T - BC)\hat{z} \tag{3.2}$$

$$\frac{\partial T}{\partial t} + (\vec{V} \cdot \nabla)T = \nabla^2 T + Q \tag{3.3}$$

where, $\vec{u}$ is velocity, P is dynamic pressure, η is viscosity, $\bar{\bar{\varepsilon}}$ is strain rate tensor, T is temperature, C is composition, $\hat{z}$ is unit vector in vertical direction, t is time and Q is internal heating. The thermal Rayleigh number Ra is defined as:

$$Ra = \frac{\rho_0 g_0 \alpha_0 \Delta T D^3}{\eta_0 \kappa_0} \tag{3.4}$$

where ρ_0, α_0, ΔT, η_0, and κ_0 are dimensional reference values of density, thermal expansivity, temperature difference between CMB and surface, reference viscosity at temperature $T = 0.5$ (non-dimensional), and thermal diffusivity, respectively. g and h are dimensional gravitational acceleration and thickness of mantle, respectively.

The chemical density anomaly is measured by buoyancy number B, which is defined as:

$$B = \frac{\Delta \rho}{\rho_0 \alpha_0 \Delta T} \tag{3.5}$$

where, $\Delta \rho$ is the dimensional density contrast between oceanic crust and background mantle.

All boundaries have free-slip velocity boundary conditions. Temperature boundary conditions are isothermal on the top and bottom and insulating on the sides. In

this study, we examine the dynamical relationship between plumes and subducted oceanic crust, so by trial and error, we established a long-lived stable convection configuration which contains downwellings surrounded by upwelling regions on both sides. To develop an appropriate initial condition, we first performed a series of isochemical calculations to find the model with stable downwellings between two upwellings. After finding one, we ran the calculation until it reached a steady thermal state. Then, we interpolated to a high resolution mesh and introduced about 6 million tracers to represent the compositional field.

Compositional advection is performed using the ratio tracer method [*Tackley and King*, 2003]. On average, each element has 20 randomly distributed tracers which are advected with mantle flow. To provide a constant oceanic crust at the surface, we prescribe a composition of 1 to tracers that reach the upper 6km of the model. As noted in [*Christensen and Hofmann*, 1994], we also found that some crustal tracers become artificially trapped to the side boundaries, which overemphasize the amount of crustal material that accumulates in the lowermost mantle because it descends directly into the lowermost thermal boundary layer. To avoid this problem, on the upper half of model, crustal tracers are reverted back to normal background mantle if they enter a thin buffer width of 0.1 from the side boundaries. In other words, we ignore crust that is subducted along the side boundaries of the domain to avoid artificial accumulation of crust in the lowermost mantle.

O'Farrell and Lowman [2010] found that it is appropriate to disregard internal heating in Cartesian models in order to better simulate temperature conditions within spherical models that do include internal heating. In other words, adding internal heating

to Cartesian models will overheat them and as a consequence, suppress plume formation. Our previous experience with both spherical and Cartesian mantle convection modeling support this idea, and we arrive at the same general conclusion as [*O'Farrell and Lowman*, 2010]. Therefore, we exclude internal heating for most of our cases except Case 3.9 in which we employ internal heating to the subducted oceanic crust to explore how this affects our results.

The Perovskite to post-Perovskite phase transition is expected to form in relatively cooler portions of the lowermost mantle [*Murakami et al.*, 2004; *Oganov and Ono*, 2004; *Tsuchiya et al.*, 2004; *Hernlund et al.*, 2005]. It is possible that the post-Perovskite phase could be less viscous than the background mantle by about 5-1000 times [*Hunt et al.*, 2009; *Ammann et al.*, 2010]. We investigate this possibility in Case 3.10 by decreasing the viscosity of post-Perovskite of two orders. The phase transition is expected to experience a double crossing in downwelling regions [*Hernlund et al.*, 2005] which has possibly been observed by seismology [*van der Hilst et al.*, 2007]. We found that the following non-dimensional depth-temperature relationship produces double crossings of the transition within lowermost mantle portions of the downwellings:

$$D = T + 0.5 \tag{3.5}$$

where D is non-dimensional depth and T is non-dimensional temperature. We use this relation as phase boundary between Perovskite and post-Perovskite and we modify viscosity in post-Perovskite regions.

Viscosity is a function of temperature, depth and Perovskite/post-Perovskite phase:

$$\eta = \eta_{660}\eta_{ppv}\exp[A[0.5 - T]] \tag{3.6}$$

55

where A and T are activation parameter for temperature-dependence of viscosity and non-dimensional temperature, respectively. The viscosity contrast due to temperature can be computed by $\Delta\eta_T = \exp(A)$. η_{660} represents the viscosity increase at the 660 km discontinuity. In all cases of this study $\eta_{660} = 50$, indicating a 50 times viscosity increase from upper mantle to lower mantle across the 660km depth [*LithgowBertelloni and Gurnis*, 1997]. η_{ppv} represents the prescribed viscosity decrease for post-Perovskite phase transition (for Case 3.10).

All cases are performed in 2D Cartesian geometry. We employed an aspect ratio of 6 for all cases except Case 3.11, for which the aspect ratio is 7. There are 1152 and 256 elements in the horizontal and vertical direction, respectively (1344 x 256 elements for Case 3.11). The grid is refined in the top 6 km and bottom 600 km, resulting in resolutions of 3 km and 6 km in these regions, respectively.

To solve the conservation equations, we use our modified version of the convection code, Citcom [*Moresi and Solomatov*, 1995; *Moresi and Gurnis*, 1996], that includes the thermochemical convection and compositional-dependent rheology.

We perform the calculations for about 50 slab transit times, equating to several billion years of geologic time. Dimensionalized model time is often not that useful for timing geologic events because it is highly sensitive to accurately representing the viscosity structure, hence effective Rayleigh number, of the actual Earth. In other words, modest uncertainties in viscosity lead to large uncertainties associated with using dimensional time to reference geologic time. Instead, for problems such as this one, it is more appropriate to reference the transit time that takes for a slab to descend to the lowermost mantle, based on surface velocity and mantle thickness. We use the following

transit time scaling law, from *Christensen and Hofmann* [1994] to calculate the geological time:

$$t_G = t u_0 t^*$$
(3.7)

where, t_G is geological time, t and u_0 are non-dimensional time and average non-dimensional surface velocity at the surface, respectively. t^* is the transit time, which is given by $t^* = h_M / u_p$, where h_M is the thickness of the mantle and u_p is a representative mean plate velocity for the Earth. We use a transition time of 60 Ma in this study.

3.4 Results

Here, we describe 11 representative cases (Table 3.1). All cases have a thin, 6 km thick crust and an intrinsic 50x viscosity increase from upper mantle to lower mantle (in addition to temperature-dependent viscosity). In Cases 3.1-3.5, the density of oceanic crust is varied. Effects of different Rayleigh number are explored in Case 3.6 and Case 3.7. The temperature-dependence of viscosity is increased in Case 3.8. In Case 3.9, we employ internal heating to the subducted oceanic crust. Case 3.10 investigates a viscosity softening due to post-Perovskite in high-pressure, cooler regions [*van der Hilst et al.*, 2007]. In Case 3.11, we choose a different aspect ratio for the model. In order to be consistent with experimental and theoretical results [*Ringwood*, 1990; *Hirose et al.*, 2005; *Ricolleau et al.*, 2010], the buoyancy number of oceanic crust in all cases is kept in the range of 0.6-1.5 which is equivalent to a density increase of about 1.0-4.5% (depending on parameters used for non-dimensionalization) for oceanic crust with respect to background mantle.

We define Case 3.1 as the reference case, in which the buoyancy number is 0.8 and we use an activation parameter of $A = 6.91$ for the temperature dependent viscosity,

57

which leads to a maximum of 1000x viscosity contrast due to temperature. The Rayleigh number for this case is $Ra = 1.0 \times 10^7$. The steady-state, initial condition features a downwelling region in the middle of the domain, surrounded by upwelling plume regions on both sides of it. Oceanic crust is continuously introduced in the upper 6 km of the model, and most of which is ultimately subducted into the center downwelling region. Figure 3.1a illustrates the combined temperature and compositional field after 1 billion years of model time. Note the thin ribbon of oceanic crust within the downwelling region. The relatively undisturbed crust descends with the downwelling, without being stirred into the surrounding mantle. Once the crust reaches the lowermost mantle, along with the downwelling, it begins to migrate laterally toward one of the plume regions. Although the oceanic crust is denser than the surrounding mantle, most of it is unable to escape the viscous drag and settle to the lowermost mantle. Once it reaches a plume, it is viscously stirred into the background mantle. Several convection transit times have occurred by this time, and the mantle is littered with remnants of older crust that had been previous stirred by mantle plumes and is now being stirred by larger-scale mantle convection flow. The logarithm of the viscosity field at this time is shown in Figure 3.1b. Figures 3.1c and 3.1d show similar results at 2.0 and 2.8 billion years. At any given time, a small fraction of oceanic crust may reside in a tiny pile in the lowermost 0-200 km of a mantle plume, but this amount is variable and does not grow with time; it is continually entrained into the mantle plume itself. Figure 3.1e-g shows the depth profiles of average temperature, viscosity and velocity magnitude, respectively.

Case 3.2 employs a lower density crust, with a buoyancy number of 0.6. Snapshots in time are shown at 1.0 and 2.8 billion years in figures 3.2a and 3.2b,

respectively. The results are very similar to that of Case 3.1, with the main difference being that small piles of oceanic crust do not form at the base of mantle plumes in this lower-density case. Case 3.3 employs a higher density crust, with a buoyancy number of 1.0. Snapshots at 1.0 and 2.8 billion years are shown in figures 3.2c and 3.2d, respectively. The results are characteristically similar to Case 3.1, and we did not identify any noticeable differences from the reference case.

In Case 3.4, the buoyancy number of the oceanic crust is increased to 1.2. Snapshots in time are shown at 1.0 and 2.8 billion years in figures 3.3a and 3.3b, respectively. The results are quite similar to Case 3.1, with the main difference being that only a slightly larger fraction of oceanic crust resides at the base of plumes. However, this amount does not grow with time. In fact, there is a smaller accumulation of crust at the CMB at 2.8 billion years (Figure 3.3a) than at 1.0 billion years (Figure 3.3b). In Case 3.5, the density of the oceanic crust is further increased, with a buoyancy number of 1.5. Snapshots in time are shown at 1.0 and 2.8 billion years in figures 3.3c and 3.3d, respectively. In this case, we see an increased amount of oceanic crust resides at the base of plumes. However, the majority of the subducted oceanic crust is still entrained up by plumes. At any given time, the piles are quite small compared to the size of LLSVPs, which extend vertically over 1000 km above CMB [*Wang and Wen*, 2007b; *He and Wen*, 2009; 2012]. From Case 3.1 to Case 3.5, we find that the fraction of oceanic crust that accumulates at the CMB increases with the density of oceanic crust. However, none of these cases generates large accumulations of oceanic crust at the CMB at the scale of LLSVPs.

Case 3.6 employs a lower Rayleigh number $Ra = 5.0 \times 10^6$. The combined temperature and composition field is shown in Figure 3.4a. In this case, two stable plumes form at the CMB which consistently entrain the subducted oceanic crust. Case 3.7 employs a higher Rayleigh number $Ra = 5.0 \times 10^7$. The combined temperature and composition field is shown in Figure 3.4b. The higher Rayleigh number leads to a more vigorous convection. Subducted oceanic crust experiences more vigorous entrainment into upwelling plumes and is difficult to accumulate into large piles at the CMB.

Case 3.8 employs a higher temperature-dependence of viscosity, such that the temperature dependent viscosity contrast between hottest and coldest regions is 10,000x. The combined temperature and composition field and the logarithm of viscosity at 1.0 billion years are shown in figures 3.5a and 3.5b, respectively. We found 2 notable differences between this case and the reference case. Case 3.8 lacked the small piles of oceanic crust at the base of mantle plumes, and oceanic crust was more-efficiently stirred into the back ground mantle. Lowered viscosity in the high temperature regions led to weaker and more vigorously advecting mantle plumes. Oceanic crust was unable to accumulate at the base of plumes due to more vigorous entrainment into the plume conduit. Furthermore, the decreased viscosity in the upper mantle promoted more rapid stirring there, and oceanic crust that returned to the upper mantle via plume upwelling and return flow was promptly and efficiently stirred into the background mantle.

In Case 3.9, the subducted oceanic crust includes an internal heating of $Q_{crust} = 20$. Figure 3.6 shows the combined temperature and composition field for Case 3.9 at 1.0 billion years. The results are very similar to Case 3.1. We did not identify noticeable differences from the reference case.

In Case 3.10, we investigated the potential softening of downwelling material due to the Perovskite to post-Perovskite phase change [*Hunt et al.*, 2009; *Ammann et al.*, 2010]. Because the post-Perovskite transition is expected to occur in higher-pressure, colder regions of the mantle, it should be mostly present in the lowermost mantle portion of downwellings. In this case, we imposed a 100x viscosity reduction in regions of post-Perovskite phase transition. The combined temperature and composition field and the logarithm of viscosity are shown in Figure 3.7a and Figure 3.7b, respectively, at 1 billion years of model time. Note the lowered viscosity at the base of downwelling regions. The lowered viscosity at the base of the downwelling region allows oceanic crust to migrate deeper, into the lower thermal boundary layer above the bottom boundary (i.e., core-mantle boundary). However, the crust is still easily entrained up by upwelling plumes.

In Case 3.11, we employ an aspect ratio of 7 for the model. Figure 3.8 shows the combined temperature and composition field for Case 3.11 at 1.3 billion years. This case is featured by two downwellings on both sides of one upwelling plume in the center of the model. Although approximately twice the amount of oceanic crust comes into interaction with this plume compared to previous cases, the subducted oceanic crust is still entrained into this plume and no crustal material resides at the base of the plume. Small piles exist at the base of the plumes at/near the side boundaries. However, these piles could be more influenced by boundary conditions and are not representative.

3.5 Discussion

We investigated whether the negative buoyancy associated with subducted oceanic crust can overcome the viscous forces associated with mantle plumes and accumulate into large thermochemical piles with the same size of LLSVPs. In the cases

presented here, we varied the density of oceanic crust relative to the surrounding mantle, the temperature dependence of viscosity, Rayleigh number, internal heating of subducted oceanic crust, and a potential weakening of slab regions due to a rheological weakening from the post-Perovskite phase transition. We also explore influences of different aspect ratio of the model. We found that viscous stirring caused by mantle plumes was stronger than the negative buoyancy of oceanic crust, and the majority of subducted oceanic crust was stirred into the surrounding mantle. For some cases, a small amount of oceanic crust formed small, narrow piles on the order of hundreds of kilometers or less in height at the base of mantle plumes. This material was subsequently entrained into plumes at a rate equal or exceeding the rate at which it could accumulate. Even the buoyancy number of subducted oceanic crust is increased to 1.5, it is still difficult to accumulate into large piles at the CMB with the same scale as LLSVPs. Our results are consistent with *Deschamps et al.* [2012] who shows that seismic velocities of LLSVPs are better explained by iron and silicate-rich primordial materials than subducted oceanic crust.

Our cases assumed a crustal thickness and density that remained constant, at present-day values, over billions of years. If oceanic crust was thicker or denser in the geologic past, it would have stronger negative buoyancy and could therefore accumulate into large thermochemical structures in the lowermost mantle. For example, [*Brandenburg and van Keken*, 2007] found that if oceanic crust has a density higher than that inferred from experimental results, significant accumulation of crust could occur. This also occurs in calculations in which the oceanic crust is significantly thicker than present day values [*Nakagawa et al.*, 2009]. Furthermore, warmer mantle temperatures associated with earlier geologic times could facilitate temporary storage of oceanic crust

in the transition zone that could episodically avalanche into the lower mantle, enhancing accumulation within the lower mantle [*Davies*, 2008]. Therefore, it is possible that different conditions associated with early Earth history may have promoted the accumulation of oceanic crust.

We found that weakened post-Perovskite facilitated segregation of oceanic crust, allowing it to reach the lowermost thermal boundary layer, consistent with [*Nakagawa and Tackley*, 2011]. However, their study found that weakened post-Perovskite increased the amount of accumulation, whereas we find that once the oceanic crust reaches the lowermost thermal boundary, it is sheared and stretched, becoming even thinner and more easily stirred and entrained into mantle plumes. The thickness of crust in [*Nakagawa and Tackley*, 2011] is unclear because they employ a melt algorithm to generate crust, which may lead to thicker crust at earlier times.

We allow downwellings to form self-consistently, which results in symmetric subduction. As a result, our effective crustal thickness in the downwelling varies up to twice the crustal thickness (we measured a representative snapshot to be ~9 km thick at the top of the lower mantle). In order to keep the mesh resolution in the lowermost mantle at least as fine as the crustal thickness, we did not explore thinner crust. From our preliminary calculations and other studies [*Nakagawa et al.*, 2009], we found that the amount of long-term crustal accumulation at the base of the mantle increases with greater crustal thickness. Therefore, our results likely represent an upper bound, and thinner crust would be more easily stirred by and entrained into mantle plumes. Alternatively, we explored using kinematic boundary conditions at the surface which generated asymmetric subduction, but we were unable to find a satisfactory configuration that prevented

63

downwelling from unnaturally deflecting in an artificial, kinematically-induced mantle wind. *Tackley* [2011] reproduced asymmetric subduction by imposing a slab in a uniform, non-convecting mantle as the initial condition. In some cases, the descending lithosphere and crust flipped upside-down, allowing the crust to come into contact with the lowermost thermal boundary layer (not being impeded by the lithosphere), allowing it to be more easily segregated, especially in 3D calculations. It is unclear how to compare this study to ours, in terms of the amount of crustal accumulation. In [*Tackley*, 2011], plumes form in response to the slab contacting the CMB, whereas, in our calculations, oceanic crust is swept toward pre-existing plumes within upwelling regions. Furthermore, in [*Tackley*, 2011], the oceanic crust is prescribed to be 30 km thick because of presumed thickening as a slab passes through a viscosity increase at the top of the upper mantle. Our calculations employ a 50x viscosity increase; however, we find that the crust does not thicken when passing into higher viscosity lower mantle. Some previous studies on viscous mixing show that mixing in 3D is as efficient as in 2D [*Ferrachat and Ricard*, 1998; *Coltice and Schmalzl*, 2006]. This implies that there should not be large difference between 2D and 3D calculations in terms of the amount of crustal material that can accumulate in upwelling regions.

In Case 3.1 and Case 3.8, we investigated changing the temperature dependence of viscosity from 1000x (Case 3.1) to 10,000x (Case 3.8). We found that increasing the temperature dependence of viscosity did not cause an increase in accumulation of oceanic crust at the CMB. At first glance, this appears to contradict to *Christensen and Hofmann* [1994], who found that the amount of crust segregation increases with the degree of temperature dependence of viscosity. Therefore, we performed additional cases with

temperature dependent viscosity in the range of isoviscous to 10,000x viscosity contrast due to temperature. Like *Christensen and Hofmann* [1994], we found that the amount of oceanic crust accumulating at the CMB roughly increases with degree of temperature dependence of viscosity. However, in all cases, the amount of accumulation remains small. After more detailed comparison between Case 3.1 and Case 3.8, we found that a higher degree of temperature dependence of viscosity leads to higher viscosity contrast around the top of downwelling regions. This leads to larger velocity gradient in these regions where oceanic crust is more stretched and becomes slightly thinner (about 1 km thinner). Therefore, to first order, the amount of crustal accumulation at the CMB should increase with degree of temperature dependence of viscosity; however, our results show that even a slight reduction of crustal thickness can counteract the effects of increasing the temperature dependence of viscosity by a factor of 10.

3.6 Conclusion

In summary, one hypothesis for the cause of LLSVPs is that they are thermochemical piles caused by accumulation of subducted oceanic crust at the CMB. However, although subducted oceanic crust is denser than its surroundings, it was unclear whether thin oceanic crust could provide enough negative buoyancy to overcome viscous stresses that act to stir the crust into mantle. Our results find that viscous forces caused by mantle plume regions are stronger than the negative buoyancy of subducted oceanic crust, so crust is easily stirred into the background mantle. A small amount of crustal material may collect at the base of plumes, but it is sufficiently entrained away into the plume and does not accumulate into larger-scale thermochemical structures. Therefore, it is difficult for the subducted oceanic crust to accumulate into large piles at the CMB with

the same size as LLSVPs. Our study does not preclude accumulation of oceanic crust at

earlier times in Earth's history when oceanic crust may have been thicker and/or early

Earth's mantle facilitated storage and later avalanching of crust at the transition zone.

References

Ammann, M. W., J. P. Brodholt, J. Wookey, and D. P. Dobson (2010), First-principles constraints on diffusion in lower-mantle minerals and a weak D" layer, *Nature*, *465*(7297), 462-465, doi:10.1038/nature09052.

Brandenburg, J. P., and P. E. van Keken (2007), Deep storage of oceanic crust in a vigorously convecting mantle, *Journal of Geophysical Research*, *112*(B6), B06403, doi:10.1029/2006jb004813.

Buffett, B. A., E. J. Garnero, and R. Jeanloz (2000), Sediments at the Top of Earth's Core, *Science*, *290*(5495), 1338-1342, doi:10.1126/science.290.5495.1338.

Bunge, H.-P., M. A. Richards, C. Lithgow-Bertelloni, J. R. Baumgardner, S. P. Grand, and B. A. Romanowicz (1998), Time Scales and Heterogeneous Structure in Geodynamic Earth Models, *Science*, *280*(5360), 91-95, doi:10.1126/science.280.5360.91.

Christensen, U. R., and A. W. Hofmann (1994), Segregation of subducted oceanic crust in the convecting mantle, *Journal of Geophysical Research*, *99*(B10), 19867-19884, doi:10.1029/93JB03403.

Coltice, N., and J. Schmalzl (2006), Mixing times in the mantle of the early Earth derived from 2-D and 3-D numerical simulations of convection, *Geophysical Research Letters*, *33*(23), doi:10.1029/2006gl027707.

Davies, G. F. (2008), Episodic layering of the early mantle by the 'basalt barrier' mechanism, *Earth and Planetary Science Letters*, *275*(3-4), 382-392, doi:10.1016/j.epsl.2008.08.036.

Deschamps, F., L. Cobden, and P. J. Tackley (2012), The primitive nature of large low shear-wave velocity provinces, *Earth and Planetary Science Letters*, *349*(0), 198-208, doi:10.1016/j.epsl.2012.07.012.

Ferrachat, S., and Y. Ricard (1998), Regular vs, chaotic mantle mixing, *Earth and Planetary Science Letters*, *155*(1-2), 75-86, doi:10.1016/S0012-821X(97)00200-8.

Ford, S. R., E. J. Garnero, and A. K. McNamara (2006), A strong lateral shear velocity gradient and anisotropy heterogeneity in the lowermost mantle beneath the southern Pacific, *Journal of Geophysical Research*, *111*(B3), B03306, doi:10.1029/2004jb003574.

Garnero, E. J., and A. K. McNamara (2008), Structure and Dynamics of Earth's Lower Mantle, *Science*, *320*(5876), 626-628, doi:10.1126/science.1148028.

Grand, S. P. (2002), Mantle shear-wave tomography and the fate of subducted slabs, *Philosophical Transactions of the Royal Society of London Series a-Mathematical Physical and Engineering Sciences*, *360*(1800), 2475-2491, doi:10.1098/rsta.2002.1077.

Grand, S. P., R. D. van der Hilst, and S. Widiyantoro (1997), Global seismic tomography: a snapshot of convection in the Earth, *GSA Today*, *7*, 1-7, Retrived from http://geo.web.ru/sbmg/sbor/tomography/Grand/grand.html

He, Y., and L. Wen (2009), Structural features and shear-velocity structure of the "Pacific Anomaly", *Journal of Geophysical Research*, *114*(B2), B02309, doi:10.1029/2008jb005814.

He, Y., and L. Wen (2012), Geographic boundary of the "Pacific Anomaly" and its geometry and transitional structure in the north, *Journal of Geophysical Research*, *117*(B9), B09308, doi:10.1029/2012jb009436.

Hernlund, J. W., and C. Houser (2008), The statistical distribution of seismic velocities in Earth's deep mantle, *Earth and Planetary Science Letters*, *265*(3-4), 423-437, doi:10.1016/j.epsl.2007.10.042.

Hernlund, J. W., C. Thomas, and P. J. Tackley (2005), A doubling of the post-perovskite phase boundary and structure of the Earth's lowermost mantle, *Nature*, *434*(7035), 882-886, doi:10.1038/nature03472.

Hirose, K., N. Takafuji, N. Sata, and Y. Ohishi (2005), Phase transition and density of subducted MORB crust in the lower mantle, *Earth and Planetary Science Letters*, *237*(1-2), 239-251, doi:10.1016/j.epsl.2005.06.035.

Huang, J., and G. F. Davies (2007), Stirring in three-dimensional mantle convection models and implications for geochemistry: 2. Heavy tracers, *Geochemistry Geophysics Geosystems*, *8*(7), Q07004, doi:10.1029/2007gc001621.

Hunt, S. A., D. J. Weidner, L. Li, L. P. Wang, N. P. Walte, J. P. Brodholt, and D. P. Dobson (2009), Weakening of calcium iridate during its transformation from perovskite to post-perovskite, *Nature Geosci.*, *2*(11), 794-797, doi:10.1038/Ngeo663.

Ishii, M., and J. Tromp (1999), Normal-mode and free-Air gravity constraints on lateral variations in velocity and density of Earth's mantle, *Science*, *285*(5431), 1231-1236, doi:10.1126/science.285.5431.1231.

Kanda, R. V. S., and D. J. Stevenson (2006), Suction mechanism for iron entrainment into the lower mantle, *Geophysical Research Letters*, *33*(2), doi:10.1029/2005gl025009.

Labrosse, S., J. W. Hernlund, and N. Coltice (2007), A crystallizing dense magma ocean at the base of the Earth's mantle, *Nature*, *450*(7171), 866-869, doi:10.1038/Nature06355.

Lee, C. T. A., P. Luffi, T. Hoink, J. Li, R. Dasgupta, and J. Hernlund (2010), Upside-down differentiation and generation of a 'primordial' lower mantle, *Nature*, *463*(7283), 930-U102, doi:10.1038/Nature08824.

Li, C., R. D. van der Hilst, E. R. Engdahl, and S. Burdick (2008), A new global model for P wave speed variations in Earth's mantle, *Geochemistry Geophysics Geosystems*, *9*(5), Q05018, doi:10.1029/2007gc001806.

Li, X. D., and B. Romanowicz (1996), Global mantle shear velocity model developed using nonlinear asymptotic coupling theory, *Journal of Geophysical Research-Solid Earth*, *101*(B10), 22245-22272, doi:10.1029/96JB01306.

LithgowBertelloni, C., and M. Gurnis (1997), Cenozoic subsidence and uplift of continents from time-varying dynamic topography, *Geology*, *25*(8), 735-738, doi:10.1130/0091-7613(1997).

Masters, G., G. Laske, H. Bolton, and A. Dziewonski (2000), The relative behavior of shear veocity, bulk sound speed, and compressional velocity in the mantle: implications for chemical and thermal structure, in *Earth's Deep Interior: Mineral Physics and Tomography From the Atomic to the Global Scale*, edited by S. K. e. al., pp. 63-86, AGU Geophysical Monograph, Washington, D.C.

McNamara, A. K., and S. Zhong (2005), Thermochemical structures beneath Africa and the Pacific Ocean, *Nature*, *437*(7062), 1136-1139, doi:10.1038/nature04066.

Moresi, L., and M. Gurnis (1996), Constraints on the lateral strength of slabs from three-dimensional dynamic flow models, *Earth and Planetary Science Letters*, *138*(1-4), 15-28, doi:10.1016/0012-821x(95)00221-W.

Moresi, L. N., and V. S. Solomatov (1995), Numerical Investigation of 2d Convection with Extremely Large Viscosity Variations, *Physics of Fluids*, *7*(9), 2154-2162, doi:10.1063/1.868465.

Murakami, M., K. Hirose, K. Kawamura, N. Sata, and Y. Ohishi (2004), Post-Perovskite Phase Transition in MgSiO3, *Science*, *304*(5672), 855-858, doi:10.1126/science.1095932.

Nakagawa, T., and P. J. Tackley (2011), Effects of low-viscosity post-perovskite on thermo-chemical mantle convection in a 3-D spherical shell, *Geophysical Research Letters*, *38*(4), L04309, doi:10.1029/2010gl046494.

Nakagawa, T., P. J. Tackley, F. Deschamps, and J. A. D. Connolly (2009), Incorporating self-consistently calculated mineral physics into thermochemical mantle convection simulations in a 3-D spherical shell and its influence on seismic anomalies in Earth's mantle, *Geochemistry Geophysics Geosystems*, *10*(3), Q03004, doi:10.1029/2008gc002280.

Ni, S., and D. V. Helmberger (2003), Ridge-like lower mantle structure beneath South Africa, *Journal of Geophysical Research*, *108*(B2), 2094, doi:10.1029/2001jb001545.

Ni, S., E. Tan, M. Gurnis, and D. Helmberger (2002), Sharp Sides to the African Superplume, *Science*, *296*(5574), 1850-1852, doi:10.1126/science.1070698.

Nomura, R., H. Ozawa, S. Tateno, K. Hirose, J. Hernlund, S. Muto, H. Ishii, and N. Hiraoka (2011), Spin crossover and iron-rich silicate melt in the Earth's deep mantle, *Nature*, *473*(7346), 199-202, doi:10.1038/Nature09940.

O'Farrell, K. A., and J. P. Lowman (2010), Emulating the thermal structure of spherical shell convection in plane-layer geometry mantle convection models, *Physics of The Earth and Planetary Interiors*, *182*(1-2), 73-84, doi:10.1016/j.pepi.2010.06.010.

Oganov, A. R., and S. Ono (2004), Theoretical and experimental evidence for a post-perovskite phase of MgSiO3 in Earth's D" layer, *Nature*, *430*(6998), 445-448, doi:10.1038/Nature02701.

Ricolleau, A., J.-P. Perrillat, G. Fiquet, I. Daniel, J. Matas, A. Addad, N. Menguy, H. Cardon, M. Mezouar, and N. Guignot (2010), Phase relations and equation of state of a natural MORB: Implications for the density profile of subducted oceanic crust in the Earth's lower mantle, *Journal of Geophysical Research*, *115*(B8), B08202, doi:10.1029/2009jb006709.

Ringwood, A. E. (1990), Slab-Mantle Interactions .3. Petrogenesis of Intraplate Magmas and Structure of the Upper Mantle, *Chemical Geology*, *82*(3-4), 187-207, doi:10.1016/0009-2541(90)90081-H.

Ritsema, J., H. J. van Heijst, and J. H. Woodhouse (2004), Global transition zone tomography, *Journal of Geophysical Research*, *109*(B2), B02302, doi:10.1029/2003jb002610.

Su, W. J., and A. M. Dziewonski (1997), Simultaneous inversion for 3-D variations in shear and bulk velocity in the mantle, *Physics of The Earth and Planetary Interiors*, *100*(1-4), 135-156, doi:10.1016/S0031-9201(96)03236-0.

Tackley, P. J. (2011), Living dead slabs in 3-D: The dynamics of compositionally-stratified slabs entering a "slab graveyard" above the core-mantle boundary, *Physics of The Earth and Planetary Interiors*, *188*(3-4), 150-162, doi:10.1016/j.pepi.2011.04.013.

Tackley, P. J. (2012), Dynamics and evolution of the deep mantle resulting from thermal, chemical, phase and melting effects, *Earth Sci. Rev.*, *110*(1-4), 1-25, doi:10.1016/j.earscirev.2011.10.001.

Tackley, P. J., and S. D. King (2003), Testing the tracer ratio method for modeling active compositional fields in mantle convection simulations, *Geochemistry Geophysics Geosystems*, *4*(4), 8302, doi:10.1029/2001gc000214.

To, A., B. Romanowicz, Y. Capdeville, and N. Takeuchi (2005), 3D effects of sharp boundaries at the borders of the African and Pacific Superplumes: Observation and modeling, *Earth and Planetary Science Letters*, *233*(1-2), 137-153, doi:10.1016/j.epsl.2005.01.037.

Torsvik, T. H., K. Burke, B. Steinberger, S. J. Webb, and L. D. Ashwal (2010), Diamonds sampled by plumes from the core-mantle boundary, *Nature*, *466*(7304), 352-355, doi:10.1038/nature09216.

Trampert, J., F. Deschamps, J. Resovsky, and D. Yuen (2004), Probabilistic Tomography Maps Chemical Heterogeneities Throughout the Lower Mantle, *Science*, *306*(5697), 853-856, doi:10.1126/science.1101996.

Tsuchiya, T., J. Tsuchiya, K. Umemoto, and R. M. Wentzcovitch (2004), Phase transition in MgSiO3 perovskite in the earth's lower mantle, *Earth and Planetary Science Letters*, *224*(3-4), 241-248, doi:10.1016/j.epsl.2004.05.017.

van der Hilst, R. D., M. V. de Hoop, P. Wang, S. H. Shim, P. Ma, and L. Tenorio (2007), Seismostratigraphy and Thermal Structure of Earth's Core-Mantle Boundary Region, *Science*, *315*(5820), 1813-1817, doi:10.1126/science.1137867.

Wang, Y., and L. Wen (2004), Mapping the geometry and geographic distribution of a very low velocity province at the base of the Earth's mantle, *J. Geophys. Res.*, *109*(B10), B10305, doi:10.1029/2003jb002674.

Wang, Y., and L. X. Wen (2007b), Geometry and P and S velocity structure of the "African Anomaly", *Journal of Geophysical Research-Solid Earth*, *112*(B5), doi:10.1029/2006jb004483.

Wen, L., P. Silver, D. James, and R. Kuehnel (2001), Seismic evidence for a thermo-chemical boundary at the base of the Earth's mantle, *Earth and Planetary Science Letters*, *189*(3-4), 141-153, doi:10.1016/S0012-821X(01)00365-X.

Wen, L. X. (2001), Seismic evidence for a rapidly varying compositional anomaly at the base of the Earth's mantle beneath the Indian Ocean, *Earth and Planetary Science Letters*, *194*(1-2), 83-95, doi:10.1016/S0012-821x(01)00550-7.

Zhong, S., M. T. Zuber, L. Moresi, and M. Gurnis (2000), Role of temperature-dependent viscosity and surface plates in spherical shell models of mantle convection, *J. Geophys. Res.*, *105*(B5), 11063-11082, doi:10.1029/2000jb900003.

Table 3.1

Cases Used in Chapter 3.

Case	B	Ra	A	Q_{crust}	μ_{ppv}	Aspect ratio
3.1	0.8	10^7	6.91	0	1.0	6
3.2	**0.6**	10^7	6.91	0	1.0	6
3.3	**1.0**	10^7	6.91	0	1.0	6
3.4	**1.2**	10^7	6.91	0	1.0	6
3.5	**1.5**	10^7	6.91	0	1.0	6
3.6	0.8	$\mathbf{5\times10^6}$	6.91	0	1.0	6
3.7	0.8	$\mathbf{5\times10^7}$	6.91	0	1.0	6
3.8	0.8	10^7	**9.21**	0	1.0	6
3.9	0.8	10^7	6.91	**20**	1.0	6
3.10	0.8	10^7	6.91	0	**0.01**	6
3.11	0.8	10^7	6.91	0	1.0	**7**

B: Buoyancy number; Ra: Rayleigh number; A: activation parameter for temperature dependent viscosity; Q_{crust}: internal heating for subducted oceanic crust; μ_{ppv}: viscosity contrast between post-Perovskite and Perovskite.
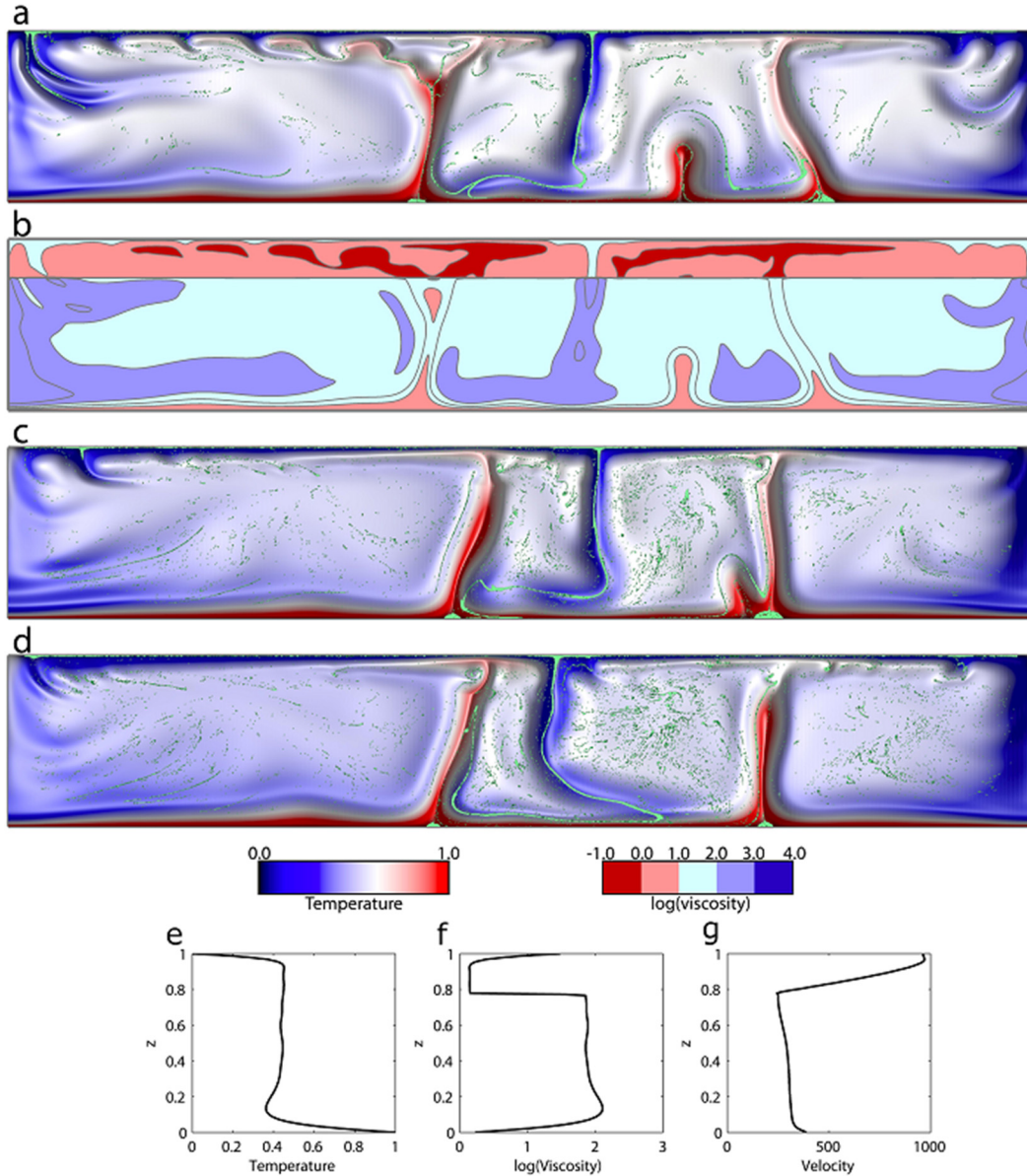
Figure 3.1. Snapshots for Case 3.1. (a) Snapshot (at 1.0 Gyr) of the non-dimensional temperature field with oceanic crust superimposed (shown in green). (b) Logarithm of non-dimensional viscosity at 1.0 Gyr. Black lines are contours of viscosity with an interval of 0.5. (c) Non-dimensional temperature and oceanic crust at 2.0 Gyr. (d) Non-dimensional temperature and oceanic crust at 2.8 Gyr. (e-g) Profiles of horizontally averaged non-dimensional temperature (e), logarithm of non-dimensional viscosity (f), and magnitude of non-dimensional velocity (g) at 1.0 Gyr. This is the reference case.
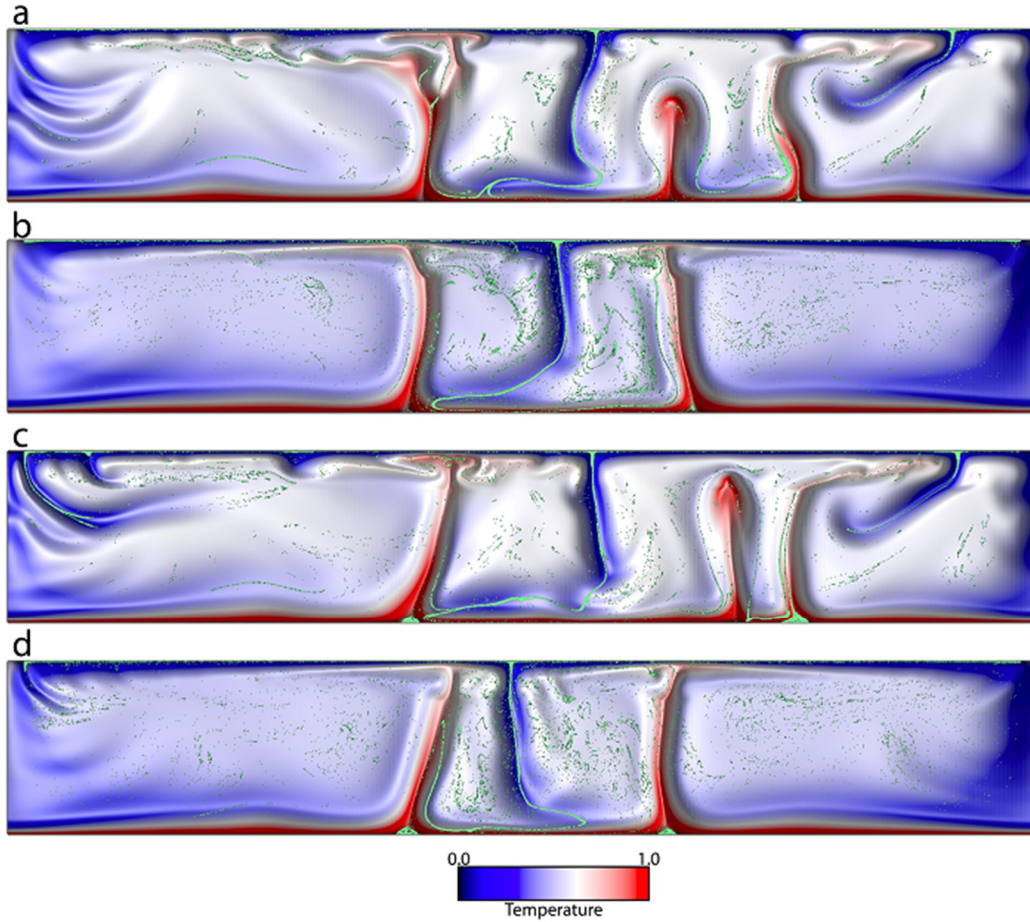
Figure 3.2. Snapshots of the non-dimensional temperature and oceanic crust for Case 3.2 (a, b) and Case 3.3 (c, d) at 1.0 Gyr (a, c) and 2.8 Gyr (b, d). The buoyancy number is B=0.6 for Case 3.2 and B=1.0 for Case 3.3.

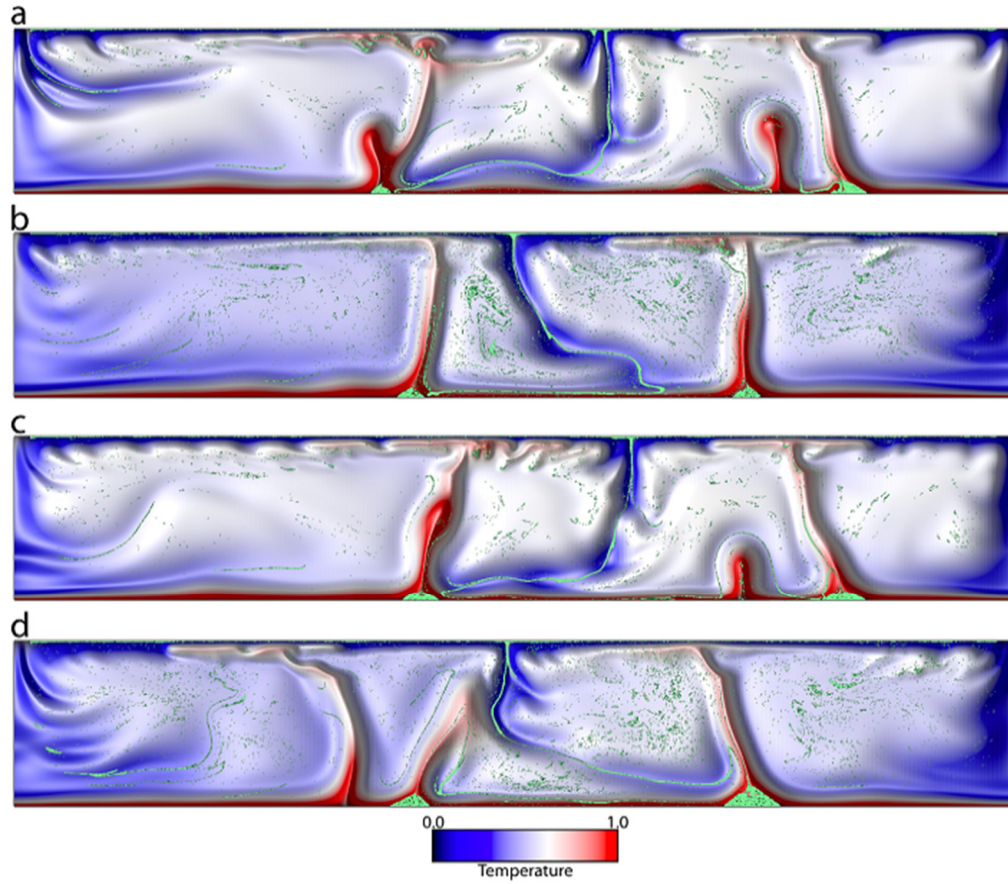*Figure 3.3*. Snapshots of the non-dimensional temperature and oceanic crust for Case 3.4 (a, b) and Case 3.5 (c, d) at 1.0 Gyr (a, c) and 2.8 Gyr (b, d). The buoyancy number is B=1.2 for Case 3.4 and B=1.5 for Case 3.5.
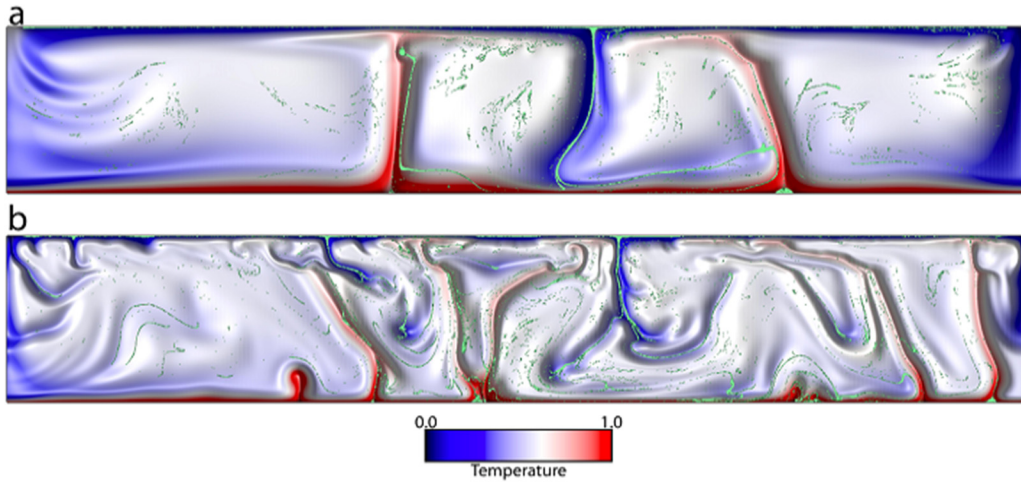
Figure 3.4. Snapshots (at 1.0 Gyr) of the non-dimensional temperature and oceanic crust for Case 3.6 (a) and Case 3.7 (b). The Rayleigh number is Ra=5e6 for Case 3.6 and Ra=5e7 for Case 3.7.

Figure 3.5. Case 3.8 (a) Snapshot (at 1.0 Gyr) of the non-dimensional temperature and oceanic crust. (b) Logarithm of non-dimensional viscosity at 1.0 Gyr. Black lines are contours of viscosity with an interval of 0.5. This case employs 10x higher temperature-dependence of viscosity than that of the reference case.
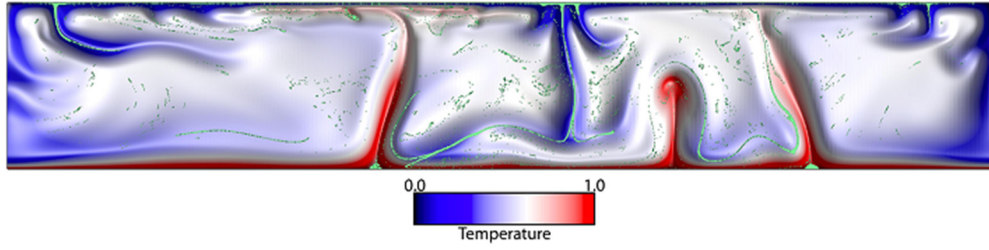
Figure 3.6. Snapshots of the non-dimensional temperature and oceanic crust for Case 3.9 at 1.0 Gyr. The subducted oceanic crust includes an internal heating of 20 in this case.
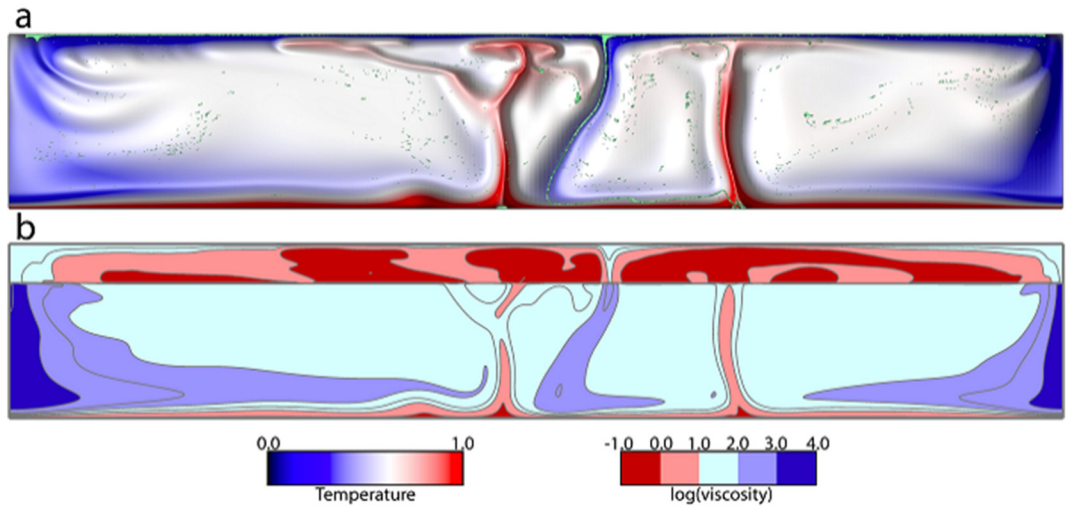
Figure 3.7. Case 3.10 (a) Snapshot (at 1.0 Gyr) of the non-dimensional temperature and oceanic crust. (b) Logarithm of non-dimensional viscosity at 1.0 Gyr. Black lines are contours of viscosity with an interval of 0.5. The viscosity is reduced by 100x in post-Perovskite regions.
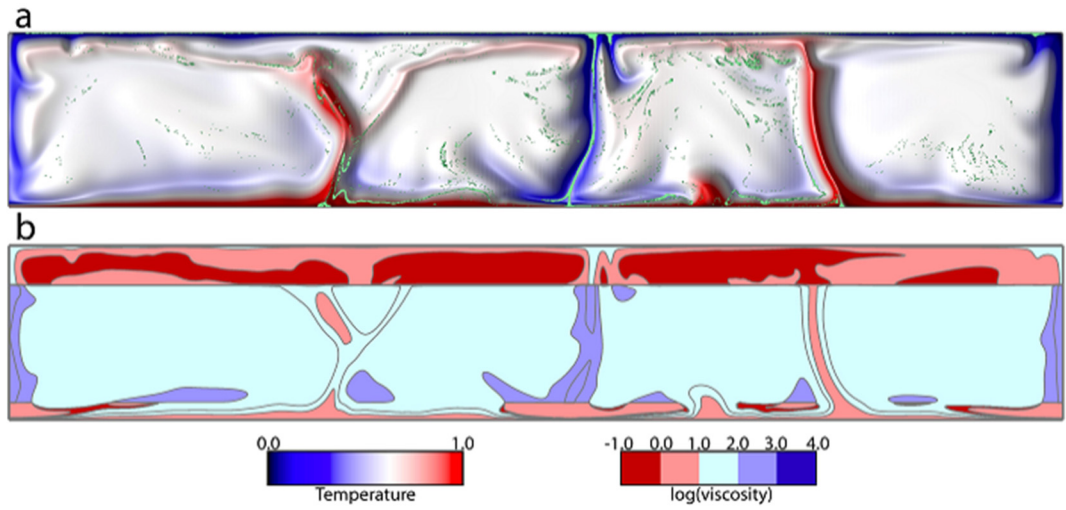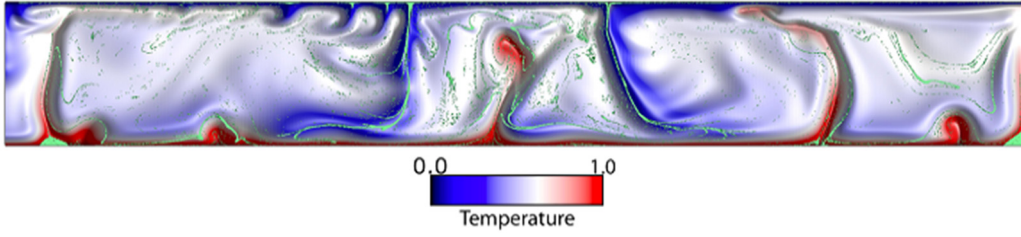
Figure 3.8. Snapshots of the non-dimensional temperature and oceanic crust for Case 3.11 at 1.3 Gyr. The aspect ratio is 7 in this case.

CHAPTER 4

CHEMICAL COMPLEXITY OF HOTSPOTS CAUSED BY CYCLING OCEANIC

CRUST THROUGH MANTLE RESERVOIRS

The work presented in this chapter was published as *Li, M., et al. (2014). "Chemical complexity of hotspots caused by cycling oceanic crust through mantle reservoirs." Nature Geosci 7(5): 366-370, DOI: 10.1038/NGEO2120.*

4.1 Abstract

Ocean-island basalts erupted from hotspots such as Hawaii display a rich chemistry derived from multiple compositional sources, including a more-primitive, less-degassed, component and several recycled, oceanic crustal components [*Hofmann*, 1997; *Jackson et al.*, 2010; *Mukhopadhyay*, 2012]. These sources have been hypothesized to originate from mantle reservoirs that are entrained to the surface by mantle plumes [*Tackley*, 2000]. However, it remains unclear how individual mantle plumes could succesively sample each of these reservoirs. Furthermore, it is challenging to reconcile crustal signatures in ocean-island basalts that display vastly different crustal ages [*Sobolev et al.*, 2011; *Cabral et al.*, 2013]. Here, we perform high resolution calculations to investigate the interaction between plumes, subducted oceanic crust, and a more-primitive lower mantle reservoir. We show that, while some subducted oceanic crust is entrained directly into mantle plumes, a significant fraction (up to ~10%) enters more-primitive reservoirs. This fraction increases with the intrinsic density of oceanic crust and is strongly enhanced by a rheologically weaker post-Perovskite in the lowermost mantle.

As a result, mantle plumes entrain a variable combination of (a) relatively young oceanic crust, (b) ancient more-primitive material stirred with older oceanic crust, and (c) background, depleted mantle. This work provides an explanation for multi-component geochemical signatures of ocean-island basalts and reconciles the vastly different ages of oceanic crust observed in these basalts [*Sobolev et al.*, 2011; *Cabral et al.*, 2013].

4.2 Introduction

The two large low shear velocity provinces (LLSVPs) of the lower mantle [*Garnero and McNamara*, 2008; *Dziewonski et al.*, 2010; *He and Wen*, 2012] are hypothesized to be caused by large accumulations of intrinsically denser more-primitive material [*Tackley*, 1998; *Labrosse et al.*, 2007; *Deschamps et al.*, 2011; *Deschamps et al.*, 2012], perhaps formed by Earth's early differentiation processes [*Labrosse et al.*, 2007]. This material could be swept into thermochemical piles beneath upwelling regions by Earth's subducting history [*McNamara and Zhong*, 2005; *Bull et al.*, 2009]. Plumes are predicted to root from the top of these piles, entraining a small amount of more-primitive material into them [*Deschamps et al.*, 2011]. This conceptual framework provides an understanding for the more-primitive chemical signature of ocean-island basalts, but it doesn't explain the recycled oceanic crustal components (e.g., HIMU, EM1, EM2) [*Hofmann*, 1997]. Previous numerical calculations have shown that the interaction between subducted oceanic crust and a dense layer of undegassed material could result in plumes entraining both components [*Samuel and Farnetani*, 2003; *Tackley*, 2011]. However, it is unclear how subducted oceanic crust would interact with the thermochemical piles that are hypothesized to cause the LLSVPs and lead to compositional heterogeneity within plumes. It is also unclear how plumes could entrain

recycled oceanic crust with vastly different ages, ranging from Archean time [*Cabral et al.*, 2013] to geologically-recent [*Sobolev et al.*, 2011].

4.3 Method

We modified the 2D Cartesian code Citcom [*Moresi and Gurnis*, 1996] to include multiple thermochemical species and compositional rheology to solve the following equations of conservation equations of mass, momentum and energy in Boussinesq approximation:

$$\nabla \cdot \vec{u} = 0 \tag{4.1}$$

$$-\nabla P + \nabla(\eta \bar{\bar{\dot{\varepsilon}}}) = Ra(T - BC)\hat{z} \tag{4.2}$$

$$\frac{\partial T}{\partial t} + (\vec{V} \cdot \nabla)T = \nabla^2 T + Q \tag{4.3}$$

where, $\vec{u}$ is velocity, P is dynamic pressure, η is viscosity, $\bar{\bar{\dot{\varepsilon}}}$ is strain rate tensor, T is temperature, C is composition, $\hat{z}$ is unit vector in vertical direction, t is time and Q is internal heating. The thermal Rayleigh number Ra is defined as:

$$Ra = \frac{\rho_0 g \alpha_0 \Delta T D^3}{\eta_0 \kappa_0} \tag{4.4}$$

where ρ_0, α_0, ΔT, η_0, and κ_0 are dimensional reference values of density of the background mantle, thermal expansivity, temperature difference between core-mantle boundary and surface, reference viscosity at temperature $T = 0.5$ (non-dimensional), and thermal diffusivity, respectively. g and h are dimensional gravitational acceleration and thickness of mantle, respectively.

The buoyancy number B is defined as the ratio between chemical density anomaly and density anomaly due to thermal expansion:

$$B = \frac{\Delta \rho}{\rho_0 \alpha_0 \Delta T} \tag{4.5}$$

where, $\Delta\rho$ is intrinsic density difference from the background mantle. Both α_0 and ρ_0 are constant throughout the model. In this study, we use α_0=1e-5 (which is the value representative of the lowermost mantle [*Chopelas and Boehler*, 1992]) and $\Delta T = 3000K$ for non-dimensionalization. The term $T - BC$ in the right part of Eq. (4.2) is effective buoyancy, which reflects density contributions from chemical intrinsic density and from density changes due to thermal effects.

We employ a Rayleigh number Ra=1×10^7 for most cases. Viscosity is both depth- and temperature-dependent. A 50x viscosity increase is employed from upper mantle to lower mantle. The temperature dependent viscosity is expressed as $\eta_T = \exp[A(0.5 - T)]$, where T is non-dimensional temperature, and we use a non-dimensional activation coefficient of A=9.21, leading to a 10,000x viscosity range due to changes in temperature. Table 4.1 lists all cases used in this study.

MgSiO$_3$-Perovskite (Pv) is expected to undergo a phase transition to post-Perovskite (pPv) at lowermost mantle pressures in cold downwelling regions [*Murakami et al.*, 2004; *Oganov and Ono*, 2004; *Tsuchiya et al.*, 2004; *Shim*, 2008] where it may undergo a double crossing [*Hernlund et al.*, 2005], which has possibly been observed by seismology [*Lay et al.*, 2006; *van der Hilst et al.*, 2007]. Mineral physics experiments and theoretical calculations have suggested a reduction of viscosity for pPv, compared to Pv [*Hunt et al.*, 2009; *Ammann et al.*, 2010], which may influence the segregation of oceanic crust from the downwelling slab [*Nakagawa and Tackley*, 2011; *Li and McNamara*, 2013]. In this study, a viscosity reduction due to pPv phase transition is employed in the lowermost mantle. We found that the non-dimensional depth-temperature relationship, D = T + 0.5, produces double crossings of the phase transition within downwelling regions

of the lowermost mantle (for D>0.9), where D and T are non-dimensional depth and temperature respectively. We use this relation as phase boundary between Perovskite and post-Perovskite, and we explore different viscosity reduction in post-Perovskite regions in this study. Because the Clapeyron slope of post-Perovskite phase transition is not very well constrained and large uncertainties exist for the temperature of Earth's lowermost mantle, the justification for this non-dimensional phase equation is only based on the goal to obtain a lens of the post-Perovskite phase in colder regions of the lowermost mantle, as is observed by seismic studies [*Lay et al.*, 2006; *van der Hilst et al.*, 2007]. This simple non-dimensional phase equation does not place contraints on the dimensional parameters for the post-Perovskite phase transition.

Our models contain three compositional components, including background mantle, subducted oceanic crust and an ancient more-primitive material. Different compositional components are represented by different type of tracers, and we use the ratio tracer method [*Tackley and King*, 2003] to simulate the composition field. About 7.4 million tracers are used in this study.

To generate an appropriate initial condition, we first perform a lower-resolution (1152 x 192 elements), 2-component calculation that includes only the more-primitive material and background mantle until the model comes to thermal equilibrium and large-scale thermochemical piles (composed of denser more-primitive material) are developed. Then, we interpolate the temperature and composition fields to higher resolution (1152x320 elements). The new mesh is refined in the very top (3 km resolution) and lowermost 1200 km of the mantle (6 km resolution). Thereafter, we continually introduce a 6-km-thick oceanic crust near the surface of the model. In order to introduce a 6 km

86

thick oceanic crust at the surface, tracers are changed into crustal type once they are advected up by mantle flow and pass through the 6 km depth below surface. The crustal tracers are changed into background mantle tracers as they enter a buffer width of 0.1 from the side boundaries to avoid artificially embedding it into the lower thermal boundary layer along side boundaries [*Christensen and Hofmann*, 1994; *Li and McNamara*, 2013].

All boundaries are free-slip. Temperature boundary conditions are isothermal on the top and bottom and insulating on both sides.

When constructing the composition field in our figures, we first define a high resolution mesh with 5 km resolution for each element. We then calculate the number of tracers for each material within every element and the composition for the element is estimated based on the following criteria:

1. If there are crustal tracers within the element, the composition of the element is treated as crust.

2. If the element does not contain crustal tracers, but contain more-primitive material tracers, the composition of the element is treated as more-primitive material.

3. If the element does not contain any crustal tracers or more-primitive material tracers, the composition of the element is treated as background mantle material.

4.4 Results

We define a reference case in which the oceanic crust and more-primitive material have the same buoyancy number of 0.8 (about 2-3% denser than background mantle) and the viscosity of the pPv phase is reduced by 100 times (in addition to the temperature-dependence of viscosity). Figure 4.1 shows a snapshot of the reference case well into the

calculation, at 856 Myr. Figure 4.1a is the temperature field with mantle velocity superimposed as arrows. Figure 4.1b shows the compositional field. Figure 4.1c shows the logarithm of viscosity; note the viscosity increase from upper to lower mantle and lenses of lowered viscosity at the base of downwellings due to the presence of pPv. The more-primitive material forms 3 piles in the lowermost mantle that are separated by downwellings, which carry a thin layer of oceanic crust that is ultimately incorporated into the lower thermal boundary layer and advected towards the piles.

Each pile is characterized by high temperature and undergoes vigorous internal convection. The composition of the piles is largely more-primitive material (~90%) but contains oceanic crust (~2%) and background mantle (~8%) (Figure 4.1b). As shown in Figure 4.2, the proportion of subducted oceanic crust and background mantle within piles slightly increases with time, leading to evolving composition of the piles. Thermal plumes forming on top of the piles entrain multiple materials: ~2% more-primitive material, ~3% subducted oceanic crust (including geologically younger oceanic crust originating outside of the piles and relatively older crustal material that is stirred and later entrained out with the more-primitive material), and background mantle (Figure 4.1b). Figure 4.3 shows the proportion of oceanic crust and more-primitive material within plumes as a function of time. Outside of the piles, subducted oceanic crust and material entrained from piles are stirred into the background mantle, forming a "marble cake" texture [*Allegre and Turcotte*, 1986].

Figure 4.4 shows a representative time sequence of snapshots from the reference case, illustrating how subducted oceanic crust is transported into and out of the pile and into the mantle plume. Figure 4.4a-c are zoomed-in at the top of the central pile, in the

region at the root of the mantle plume where material is exchanged between the pile and surrounding mantle. The corresponding effective buoyancy (which reflects density contributions from chemical intrinsic density and from density changes due to thermal effects) for Figure 4.4a-c is illustrated in Figure 4.5. Figure 4.4d-e are zoomed-out for the entire central pile. Figure 4.4a shows a time when oceanic crust is being carried directly into the mantle plume. Furthermore, two-way material exchange is observed at the top of the pile, where pile material is being entrained into the plume and background mantle is being entrained into the pile. Figure 4.4b shows a later time at which oceanic crust accumulates at the base of the plume, atop the pile. After ~20 Myr, the accumulation of oceanic crust (from Figure 4.4b) is flushed into the pile (Figure 4.4c). A significant amount of background mantle material with positive effective buoyancy (Figure 4.5) gets trapped within this crustal package on top of the pile (Figure 4.5b) and hence gets viscously coupled and later incorporated into the pile with the crustal material (Figure 4.5c). We find this time sequence of events to be a typical process throughout all of the calculations performed, in which the subducted oceanic crust is episodically flushed into the more-primitive reservoir. Figures 4.4d and 4.4e show later times at which the flushed accumulation of crust (on the scale of ~100 km) is stretched and stirred because of internal convection within the pile (Figure 4.4e).

In the reference case discussed above, the oceanic crust and more-primitive material have the same intrinsic density. An important question relates to how different density contrasts between the two components affects the dynamics, particularly whether it could lead to density stratification (e.g., separate oceanic crust and more-primitive reservoirs). In Figure 4.6a-d, we show two cases in which the oceanic crust is either

89

intrinsically less dense (B_c=0.6, Figure 4.6a-b) or more dense (B_c=1.0, Figure 4.6c-d) than the more-primitive material. We find that these two cases highly resemble the reference case, and therefore, relatively modest intrinsic density contrasts (~1%) between oceanic crust and more-primitive material do not change the fundamental dynamics. This indicates that the relevant dynamics are more controlled by viscous forces than buoyancy forces for realistically thin oceanic crust. Furthermore, we explored additional cases (Case 4.4-4.5) in which the buoyancy number of oceanic crust ranged from B_c=0.0 to B_c=1.2, corresponding to ~0-4% denser than the background mantle [*Hirose et al.*, 2005]. In all cases, the relevant dynamics resembled the reference case, characterized by multiple, alternative pathways of oceanic crust which is either directly entrained into upwelling plumes, episodically flushed into the more-primitive reservoir, or stirred into the background mantle. Nevertheless, we did find that the fraction of subducted oceanic crust within the piles increases with the intrinsic density of oceanic crust, as shown in Figure 4.7.

Figure 4.7 shows the percentage of total oceanic crust that resides within piles as a function of time. It is important to note that relative differences are more meaningful than absolute values because the magnitude of entrainment is somewhat dependent upon mesh resolution (as is typical in numerical models), even for these high resolution calculations. In all cases, the percentage is zero near the beginning because it takes a finite amount of time for the crust to descend into the lower mantle before being incorporated into piles. After about 350 Myrs, the reference case (solid black line) is characterized by about 7-10% of oceanic crust being incorporated into the piles.

90

Figure 4.7 also shows how the viscosity of the pPv phase significantly influences the amount of oceanic crust that is incorporated into piles. The reference case employed a 100x viscosity reduction in the pPv phase that allowed oceanic crust to go deeper into the lower thermal boundary layer [*Nakagawa and Tackley*, 2011; *Li and McNamara*, 2013], where it is dragged closer to the pile surface by mantle flow and more easily incorporated into the pile. As we lessen the viscosity reduction of the pPv phase, oceanic crust doesn't penetrate the lower thermal boundary layer as deeply, and therefore, the amount of oceanic crust being incorporated into the piles is reduced.

Here, we varied the buoyancy number of oceanic crust (Case 4.2-4.5) and the intrinsic viscosity reduction associated with the pPv phase (Case 4.6-4.7), both being parameters expected to play important, first-order roles in the underlying dynamics associated with this study. We found that although these parameters controlled the amount of oceanic crust that is incorporated into piles (Figure 4.7), the fundamental dynamical process remained unchanged.

We also investigated parameters such as Rayleigh number (Case 4.8-4.9), temperature-dependence of viscosity (Case 4.10), amount of internal heating (Case 4.11), and buoyancy number of more-primitive material (Case 4.12), which lead to only second-order effects as expected (Figure 4.8-4.17).

In Figure 4.8, we show a snapshot at 1.0 Gyrs for Case 4.4 in which the buoyancy number of oceanic crust is B=0.0. In this case, only a very small amount of oceanic crust could enter the piles. The major part of it is entrained into plumes and mixed into the background mantle. However, as the buoyancy number of oceanic crust is increased to B=1.2 (Case 4.5) which is shown in Figure 4.9, a great increase of the amount of oceanic

crust inside piles is observed. Nevertheless, the interaction between subducted oceanic crust and the more-primitive reservoir material resembles the reference case. Subducted oceanic crust takes alternative pathways at the top piles, either being directly entrained into plumes or flushed into the piles.

In Figure 4.10, we show a snapshot of Case 4.6 in which no viscosity reduction is applied to post-Perovskite. In this case, the major part of subducted oceanic crust is dragged to upwellings before arriving at the lower thermal boundary layer. Only a small amount of oceanic crust could enter the piles (Figure 4.7). We lower the viscosity of post-Perovskite by 10x in Case 4.7 which is shown in Figure 4.11, but no noticeable change is observed.

In Figure 4.12, we show a snapshot at 839 Myr for Case 4.8 with lower Rayleigh number ($Ra = 5 \times 10^6$) than that of the reference case ($Ra = 1 \times 10^7$). The result is similar to the reference case. A significant amount of subducted oceanic crust is flushed into the more-primitive reservoir through the top of piles, and undergoes vigorous stirring within the piles. Plumes forming on top of piles entrain a combination of different compositions.

In Figure 4.13, we show a snapshot at 828 Myr for Case 4.9 with higher Rayleigh number ($Ra = 5 \times 10^7$) than that of the reference case ($Ra = 1 \times 10^7$). At higher Rayleigh number, piles become more stagnant with a lower topography. The same result is also found by *Tackley* [1998], who explained that higher Rayleigh number leads to decreasing stresses associated with thicker upwellings and downwellings. Nevertheless, the subducted oceanic crust accumulates at the top of piles and episodically flushed into

the piles. The interaction between the subducted oceanic crust and the more-primitive reservoir is similar to the reference case.

In Figure 4.14, we show a snapshot at 855 Myr for Case 4.10 with lower temperature dependence of viscosity than that of the reference case, which leads to 1,000x temperature-dependent viscosity contrast between the hottest and coldest region. Different from the reference case, we notice that more materials from piles are entrained away by plumes and mixed into the background mantle. The same result is also found by *Deschamps and Tackley* [2008]. The reason may be that lower degree of temperature dependent viscosity increases the viscous coupling between hot piles and their surroundings. Referring to the interaction between subducted oceanic crust and more-primitive reservoir, we did not identify noticeable differences from the reference case.

In Figure 4.15, we show a snapshot at 343 Myr for Case 4.11 with internal heating (Q=20). Compared to the reference case, temperature difference between piles and their surroundings is reduced and mantle plumes become less effective to supporting piles, which leads to a reduction in topography of piles. In addition, entrainment of pile materials by mantle plumes also decreases. These results are also found and discussed in [*Tackley*, 1998]. At the base of mantle plumes, the subducted oceanic crust takes dual pathways: either being directly entrained up into plumes or being episodically flushed into the piles, with the same process to the reference case.

In Figure 4.16, we show a snapshot at 653 Myr for Case 4.12 in which the buoyancy number for the more-primitive reservoir material is increased to 1.0. Because of increased density of the piles, entrainment of pile materials by plumes is decreased. In this case, the oceanic crust is less dense than the more-primitive reservoir. The subducted

93

oceanic crust interact with the more-primitive reservoir in similar way as the reference case, but the fraction of oceanic crust inside piles is reduced as is shown in Figure 4.17.

In Figure 4.17, we show the fraction of total oceanic crust that is incorporated into the piles as a function of time for Case 4.8-4.12 and the reference case. Except for Case 4.12, where the fraction is lower than that of the reference case, the fraction in Case 4.8-4.11 is of the same level as the reference case. Compared to the effects of density contrast between subducted oceanic crust and more-primitive reservoir material and the viscosity of weakened post-Perovskite, parameters including Rayleigh number, temperature-dependent viscosity and internal heating generate only second-order differences for the amount of subducted oceanic crust that could enter the thermochemical piles.

4.5 Discussion and Conclusion

This work shows how subducted oceanic crust interacts with long-lived, originally more-primitive compositional reservoirs (which are hypothesized to cause the LLSVPs). We show that oceanic crust first enters the lowermost thermal boundary layer at the CMB in downwelling regions and is then transported laterally toward and then, up along the surface of the piles. At the top of the piles where plumes are rooted, the oceanic crust is either entrained into plumes (along with material from the pile) or flushed into the pile. This process appears to be dominated by viscous forces and is relatively insensitive to density contrasts between the oceanic crust and more-primitive material.

Within piles, oceanic crust is continually stirred within the more-primitive material, leading to multi-scale compositional heterogeneity in space and time. This could possibly contribute to seismic heterogeneity and/or discontinuities within LLSVPs as is observed by seismic studies [*Lay et al.*, 2006; *Ohta et al.*, 2008]. In particular, future

seismological studies should focus on the tops of LLSVPs, where the oceanic crust may be detected. More importantly, this heterogeneity would be reflected in hotspot basalt chemistry because mantle plumes would entrain a time-variable combination of different compositions, including (a) relatively young oceanic crust, (b) older oceanic crust that was flushed into the pile at an earlier time, (c) ancient, more-primitive reservoir material, and (d) depleted background mantle. In addition, plumes sampling geographically different parts of the LLSVPs could have different composition [*Weis et al.*, 2011]. These factors provide an explanation for the spatial and temporal variability of trace element chemistry in hotspot basalts [*Hofmann*, 1997; *Farnetani et al.*, 2002; *Weis et al.*, 2011], and provide an understanding of why signatures of oceanic crust in hotspot basalts can range from Archean age [*Cabral et al.*, 2013] to geologically recent [*Sobolev et al.*, 2011].

References

Allegre, C. J., and D. L. Turcotte (1986), Implications of a two-component marble-cake mantle, *Nature*, *323*(6084), 123-127, doi:10.1038/323123a0.

Ammann, M. W., J. P. Brodholt, J. Wookey, and D. P. Dobson (2010), First-principles constraints on diffusion in lower-mantle minerals and a weak D" layer, *Nature*, *465*(7297), 462-465, doi:10.1038/nature09052.

Bull, A. L., A. K. McNamara, and J. Ritsema (2009), Synthetic tomography of plume clusters and thermochemical piles, *Earth and Planetary Science Letters*, *278*(3-4), 152-162, doi:10.1016/j.epsl.2008.11.018.

Cabral, R. A., M. G. Jackson, E. F. Rose-Koga, K. T. Koga, M. J. Whitehouse, M. A. Antonelli, J. Farquhar, J. M. Day, and E. H. Hauri (2013), Anomalous sulphur isotopes in plume lavas reveal deep mantle storage of Archaean crust, *Nature*, *496*(7446), 490-493, doi:10.1038/nature12020.

Chopelas, A., and R. Boehler (1992), Thermal expansivity in the lower mantle, *Geophysical Research Letters*, *19*(19), 1983-1986, doi:10.1029/92gl02144.

Christensen, U. R., and A. W. Hofmann (1994), Segregation of subducted oceanic crust in the convecting mantle, *Journal of Geophysical Research*, *99*(B10), 19867-19884, doi:10.1029/93JB03403.

Deschamps, F., L. Cobden, and P. J. Tackley (2012), The primitive nature of large low shear-wave velocity provinces, *Earth and Planetary Science Letters*, *349*(0), 198-208, doi:10.1016/j.epsl.2012.07.012.

Deschamps, F., E. Kaminski, and P. J. Tackley (2011), A deep mantle origin for the primitive signature of ocean island basalt, *Nature Geosci.*, *4*(12), 879-882, doi:10.1038/Ngeo1295.

Deschamps, F., and P. J. Tackley (2008), Searching for models of thermo-chemical convection that explain probabilistic tomography: I. Principles and influence of rheological parameters, *Physics of The Earth and Planetary Interiors*, *171*(1-4), 357-373, doi:10.1016/j.pepi.2008.04.016.

Dziewonski, A. M., V. Lekic, and B. A. Romanowicz (2010), Mantle Anchor Structure: An argument for bottom up tectonics, *Earth and Planetary Science Letters*, *299*(1-2), 69-79, doi:10.1016/j.epsl.2010.08.013.

Farnetani, C. G., B. Legras, and P. J. Tackley (2002), Mixing and deformations in mantle plumes, *Earth and Planetary Science Letters*, *196*(1-2), 1-15, doi:10.1016/S0012-821x(01)00597-0.

Garnero, E. J., and A. K. McNamara (2008), Structure and Dynamics of Earth's Lower Mantle, *Science*, *320*(5876), 626-628, doi:10.1126/science.1148028.

He, Y., and L. Wen (2012), Geographic boundary of the "Pacific Anomaly" and its geometry and transitional structure in the north, *Journal of Geophysical Research*, *117*(B9), B09308, doi:10.1029/2012jb009436.

Hernlund, J. W., C. Thomas, and P. J. Tackley (2005), A doubling of the post-perovskite phase boundary and structure of the Earth's lowermost mantle, *Nature*, *434*(7035), 882-886, doi:10.1038/nature03472.

Hirose, K., N. Takafuji, N. Sata, and Y. Ohishi (2005), Phase transition and density of subducted MORB crust in the lower mantle, *Earth and Planetary Science Letters*, *237*(1-2), 239-251, doi:10.1016/j.epsl.2005.06.035.

Hofmann, A. W. (1997), Mantle geochemistry: The message from oceanic volcanism, *Nature*, *385*(6613), 219-229, doi:10.1038/385219a0.

Hunt, S. A., D. J. Weidner, L. Li, L. P. Wang, N. P. Walte, J. P. Brodholt, and D. P. Dobson (2009), Weakening of calcium iridate during its transformation from perovskite to post-perovskite, *Nature Geosci.*, *2*(11), 794-797, doi:10.1038/Ngeo663.

Jackson, M. G., R. W. Carlson, M. D. Kurz, P. D. Kempton, D. Francis, and J. Blusztajn (2010), Evidence for the survival of the oldest terrestrial mantle reservoir, *Nature*, *466*(7308), 853-U884, doi:10.1038/Nature09287.

Labrosse, S., J. W. Hernlund, and N. Coltice (2007), A crystallizing dense magma ocean at the base of the Earth's mantle, *Nature*, *450*(7171), 866-869, doi:10.1038/Nature06355.

Lay, T., J. Hernlund, E. J. Garnero, and M. S. Thorne (2006), A Post-Perovskite Lens and D" Heat Flux Beneath the Central Pacific, *Science*, *314*(5803), 1272-1276, doi:10.1126/science.1133280.

Li, M., and A. K. McNamara (2013), The difficulty for subducted oceanic crust to accumulate at the Earth's core-mantle boundary, *Journal of Geophysical Research*, *118*(4), 1807-1816, doi:10.1002/Jgrb.50156.

McNamara, A. K., and S. Zhong (2005), Thermochemical structures beneath Africa and the Pacific Ocean, *Nature*, *437*(7062), 1136-1139, doi:10.1038/nature04066.

Moresi, L., and M. Gurnis (1996), Constraints on the lateral strength of slabs from three-dimensional dynamic flow models, *Earth and Planetary Science Letters*, *138*(1-4), 15-28, doi:10.1016/0012-821x(95)00221-W.

Mukhopadhyay, S. (2012), Early differentiation and volatile accretion recorded in deep-mantle neon and xenon, *Nature*, *486*(7401), 101-U124, doi:10.1038/Nature11141.

Murakami, M., K. Hirose, K. Kawamura, N. Sata, and Y. Ohishi (2004), Post-Perovskite Phase Transition in MgSiO3, *Science*, *304*(5672), 855-858, doi:10.1126/science.1095932.

Nakagawa, T., and P. J. Tackley (2011), Effects of low-viscosity post-perovskite on thermo-chemical mantle convection in a 3-D spherical shell, *Geophysical Research Letters*, *38*(4), L04309, doi:10.1029/2010gl046494.

Oganov, A. R., and S. Ono (2004), Theoretical and experimental evidence for a post-perovskite phase of MgSiO3 in Earth's D" layer, *Nature*, *430*(6998), 445-448, doi:10.1038/Nature02701.

Ohta, K., K. Hirose, T. Lay, N. Sata, and Y. Ohishi (2008), Phase transitions in pyrolite and MORB at lowermost mantle conditions: Implications for a MORB-rich pile above the core-mantle boundary, *Earth and Planetary Science Letters*, *267*(1-2), 107-117, doi:10.1016/j.epsl.2007.11.037.

Samuel, H., and C. G. Farnetani (2003), Thermochemical convection and helium concentrations in mantle plumes, *Earth and Planetary Science Letters*, *207*(1-4), 39-56, doi:10.1016/S0012-821x(02)01125-1.

Shim, S.-H. (2008), The Postperovskite Transition, *Annual Review of Earth and Planetary Sciences*, *36*(1), 569-599, doi:10.1146/annurev.earth.36.031207.124309.

Sobolev, A. V., A. W. Hofmann, K. P. Jochum, D. V. Kuzmin, and B. Stoll (2011), A young source for the Hawaiian plume, *Nature*, *476*(7361), 434-437, doi:10.1038/nature10321.

Tackley, P. (1998), Three-Dimensional Simulations of Mantle Convection with a Thermo-Chemical Basal Boundary Layer: D"?, *AGU Geophysical Mongraph on the CMB ed. M. Gurnis*.

Tackley, P. J. (2000), Mantle Convection and Plate Tectonics: Toward an Integrated Physical and Chemical Theory, *Science*, *288*(5473), 2002-2007, doi:10.1126/science.288.5473.2002.

Tackley, P. J. (2011), Living dead slabs in 3-D: The dynamics of compositionally-stratified slabs entering a "slab graveyard" above the core-mantle boundary, *Physics of The Earth and Planetary Interiors*, *188*(3-4), 150-162, doi:10.1016/j.pepi.2011.04.013.

Tackley, P. J., and S. D. King (2003), Testing the tracer ratio method for modeling active compositional fields in mantle convection simulations, *Geochemistry Geophysics Geosystems*, *4*(4), 8302, doi:10.1029/2001gc000214.

Tsuchiya, T., J. Tsuchiya, K. Umemoto, and R. M. Wentzcovitch (2004), Phase transition in MgSiO3 perovskite in the earth's lower mantle, *Earth and Planetary Science Letters*, *224*(3-4), 241-248, doi:10.1016/j.epsl.2004.05.017.

van der Hilst, R. D., M. V. de Hoop, P. Wang, S. H. Shim, P. Ma, and L. Tenorio (2007), Seismostratigraphy and Thermal Structure of Earth's Core-Mantle Boundary Region, *Science*, *315*(5820), 1813-1817, doi:10.1126/science.1137867.

Weis, D., M. O. Garcia, J. M. Rhodes, M. Jellinek, and J. S. Scoates (2011), Role of the deep mantle in generating the compositional asymmetry of the Hawaiian mantle plume, *Nature Geosci.*, *4*(12), 831-838, doi:10.1038/Ngeo1328.

Table 4.1

Cases Used in Chapter 4.

Case	$\Delta\eta_{pPv}$	B_c	B_p	Ra	A	Q
4.1(REF)	0.01	0.8	0.8	1e7	9.21	0
4.2	0.01	**0.6**	0.8	1e7	9.21	0
4.3	0.01	**1.0**	0.8	1e7	9.21	0
4.4	0.01	**0.0**	0.8	1e7	9.21	0
4.5	0.01	**1.2**	0.8	1e7	9.21	0
4.6	**1**	0.8	0.8	1e7	9.21	0
4.7	**0.1**	0.8	0.8	1e7	9.21	0
4.8	0.01	0.8	0.8	**5e6**	9.21	0
4.9	0.01	0.8	0.8	**5e7**	9.21	0
4.10	0.01	0.8	0.8	1e7	**6.91**	0
4.11	0.01	0.8	0.8	1e7	9.21	**20**
4.12	0.01	0.8	**1.0**	1e7	9.21	0

REF: reference case; $\Delta\eta_{pPv}$: viscosity reduction due to the pPv phase; B_c: buoyancy number of oceanic crust; B_p: buoyancy number of more-primitive material; Ra: Rayleigh number; A: activation coefficient; Q: internal heating. Numbers in bold are parameters different from the reference case.
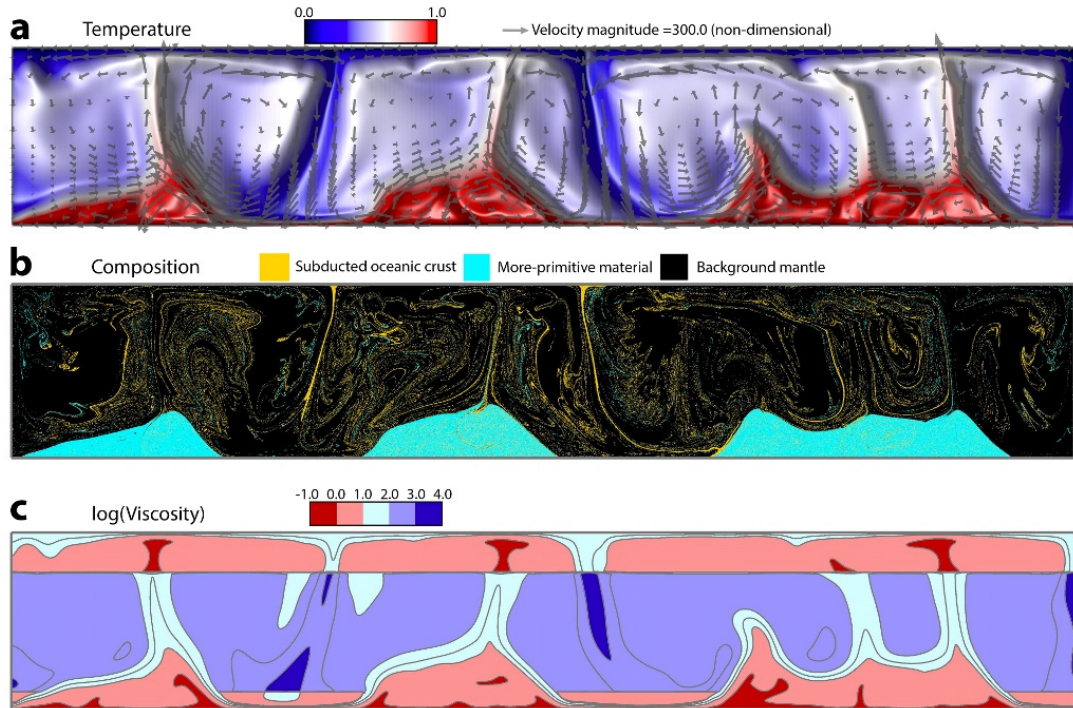
Figure 4.1. Snapshot of the reference case (Case 4.1) at 856 Myrs. a, temperature field (non-dimensional) with mantle flow velocity superimposed (gray arrows). b, composition field with 3 components: oceanic crust (yellow), more-primitive material (cyan), and background mantle (black). In this case, the more-primitive material and oceanic crust have the same density (*B*=0.8). c, logarithm of non-dimensional viscosity. Gray lines are contours with an interval of 0.5. A 100x viscosity reduction is employed for pPv, which exists near the base of downwelling regions.
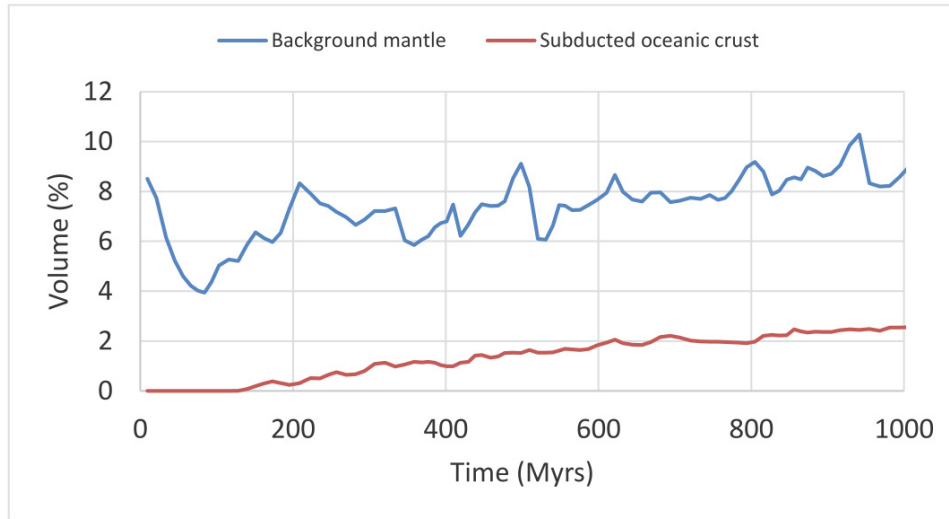
Figure 4.2. Proportion of subducted oceanic crust and background mantle within piles as a function of time, for the reference case. Note that the proportion of subducted oceanic crust and background mantle within piles increases with time, leading to a changing of composition of the thermochemical piles and plumes which entrain material from piles. In this study, the pile region is defined by $T > 0.75$ (non-dimensional), and the proportion of each compositional component within piles is estimated using the number of tracers within piles for each component.
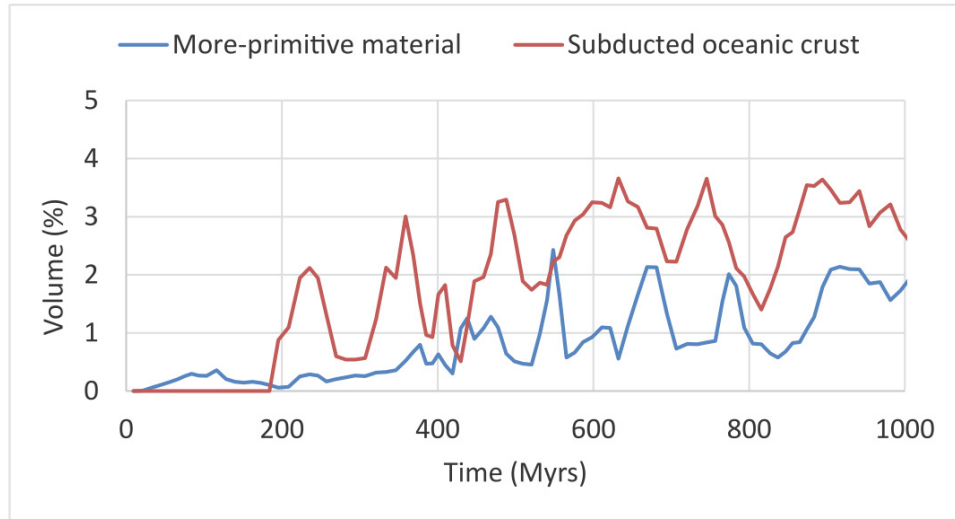
Figure 4.3. Proportion of subducted oceanic crust and more-primitive material in plumes as a function of time, for the reference case. Here, the proportion of each compositional component within plumes is estimated using the number of tracers of each component within plume regions where $T>0.5$ (non-dimensional), and with a depth range of 0-1690 km (excluding tracers within piles).
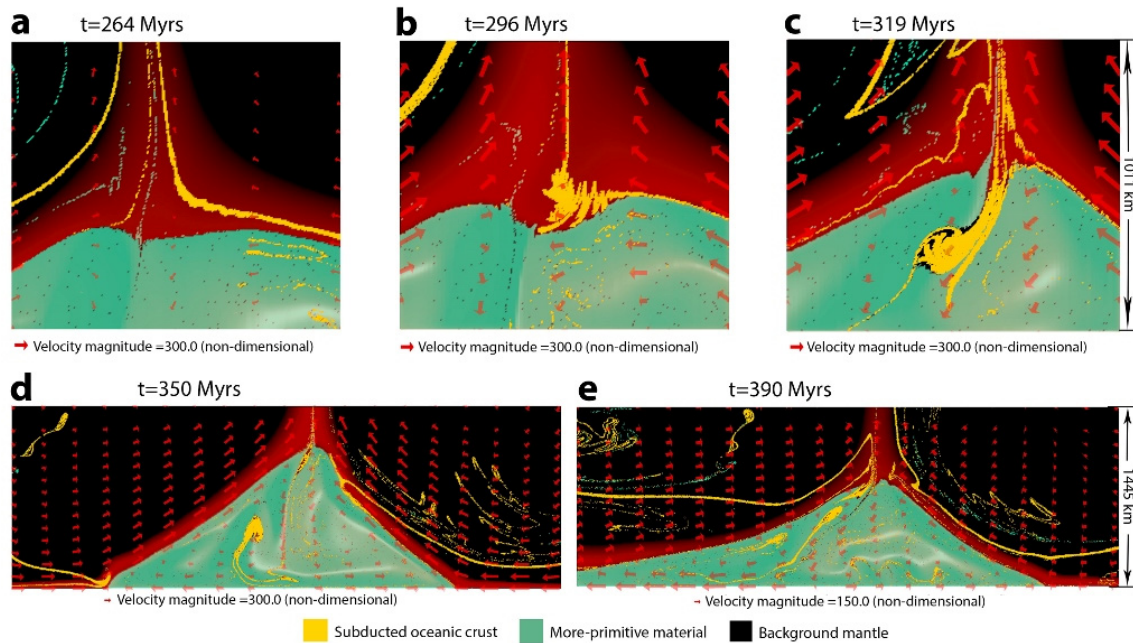
Figure 4.4. Sequence of snapshots for the reference case, showing multiple pathways for subducted oceanic crust. Only the non-dimensional temperature *T*>0.5 is displayed, which outlines plumes, piles and the thermal boundary layer. a-c, zoomed-in panels showing regions around the top of the central pile (see Figure 4.1) at 264 Myrs, 296 Myrs and 319 Myrs, respectively. d-e, zoomed-out panels showing the entire central pile at 350 Myrs and 390 Myrs, respectively.
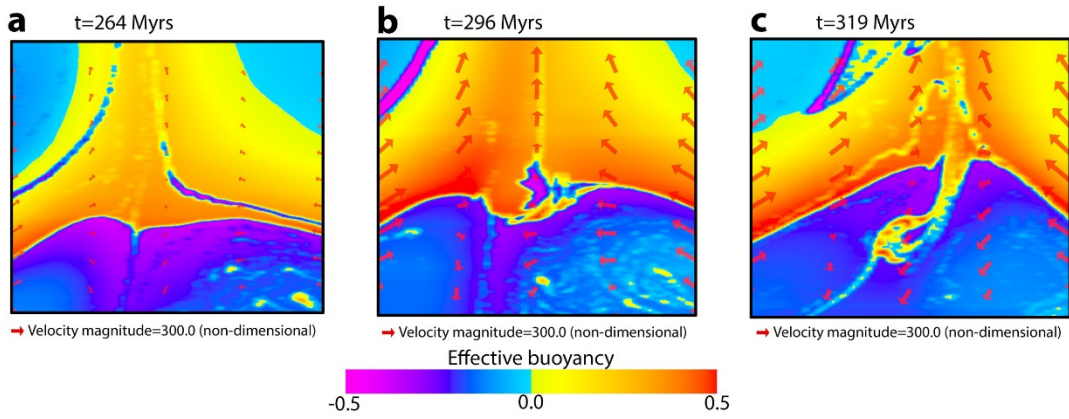
Figure 4.5. Effective buoyancy ($T - BC$) with horizontal average deducted for snapshots shown in Figure 4.4a-c.
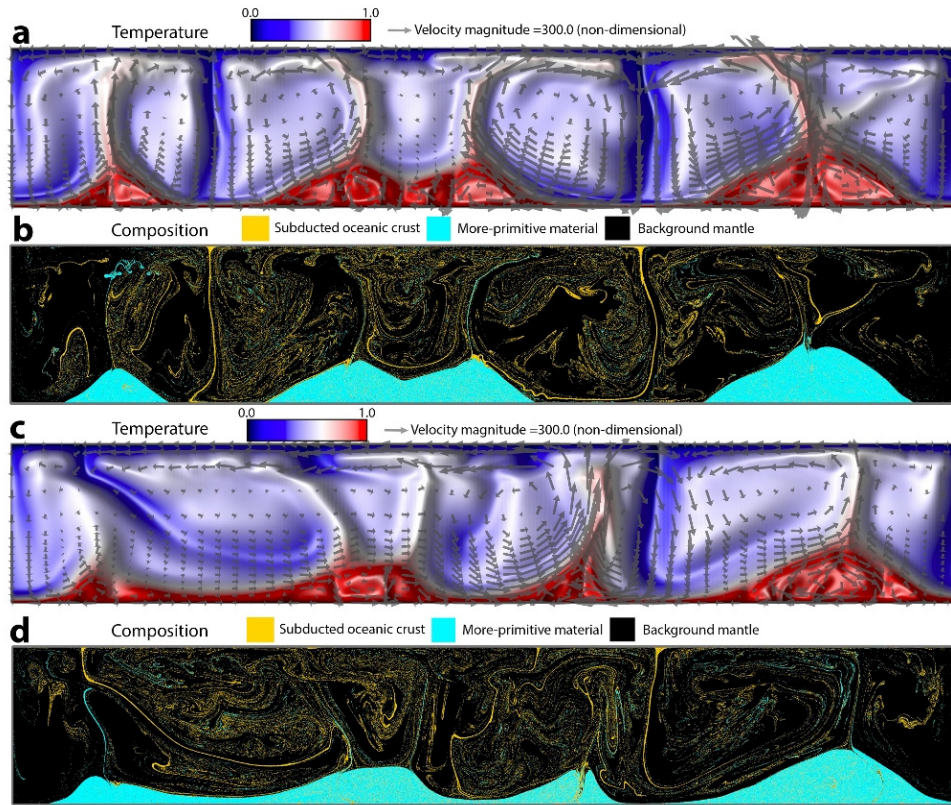
Figure 4.6. Snapshots of two cases showing the effects of density contrast between more-primitive reservoir and oceanic crust on dynamics. a-b, snapshot (at 880 Myrs) of Case 4.2 in which oceanic crust is less dense (B=0.6) than the more-primitive reservoir (B=0.8). c-d, snapshot (at 840 Myrs) of Case 4.3 in which oceanic crust is more dense (B=1.0) than the more-primitive reservoir (B=0.8). a, c, temperature field with mantle flow velocity superimposed (gray arrows). b, d, composition field (colors are the same as Figure 4.1).
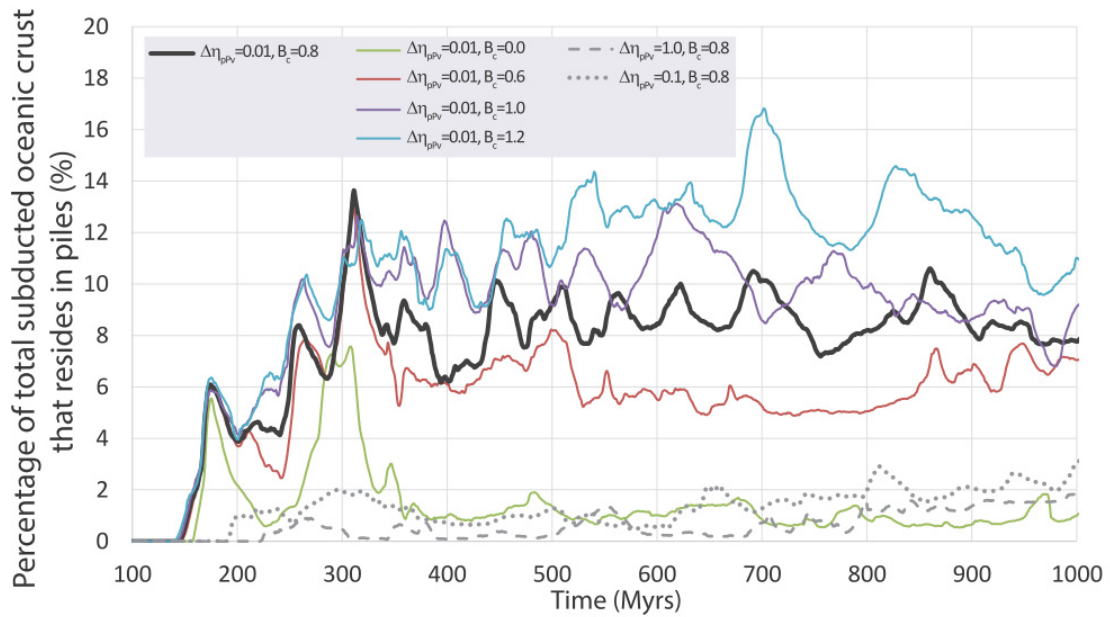
Figure 4.7. Percentage of total subducted oceanic crust that resides in piles as a function of time. $\Delta\eta_{pPv}$: viscosity reduction due to the pPv phase; B_c: buoyancy number of oceanic crust.
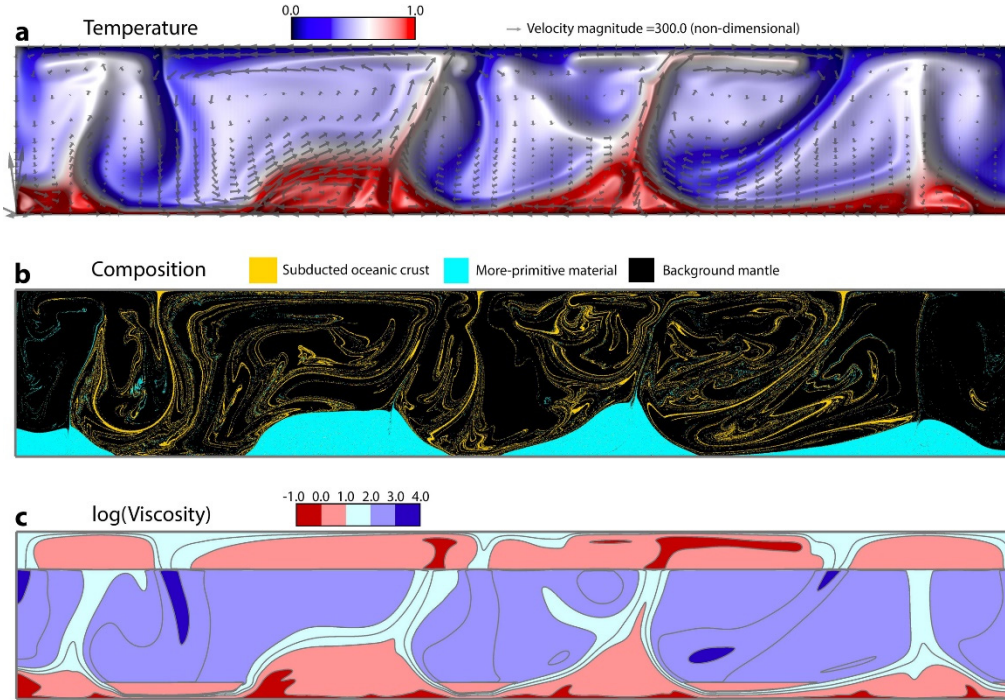
Figure 4.8. Snapshot of Case 4.4 at 1.0 Gyrs. a, temperature field (non-dimensional) with mantle flow velocity superimposed (gray arrows). b, composition field with 3 components: oceanic crust (yellow), more-primitive material (cyan) and background mantle (black). c, logarithm of viscosity (non-dimensional). Gray lines are contours with an interval of 0.5. In this case, the buoyancy number for the oceanic crust is B_c =0.0.

Figure 4.9. Snapshot of Case 4.5 at 856 Myrs. **a**, temperature field (non-dimensional) with mantle flow velocity superimposed (gray arrows). **b**, composition field with 3 components: oceanic crust (yellow), more-primitive material (cyan) and background mantle (black). **c**, logarithm of viscosity (non-dimensional). Gray lines are contours with an interval of 0.5. In this case, the buoyancy for the oceanic crust is B_c =1.2.
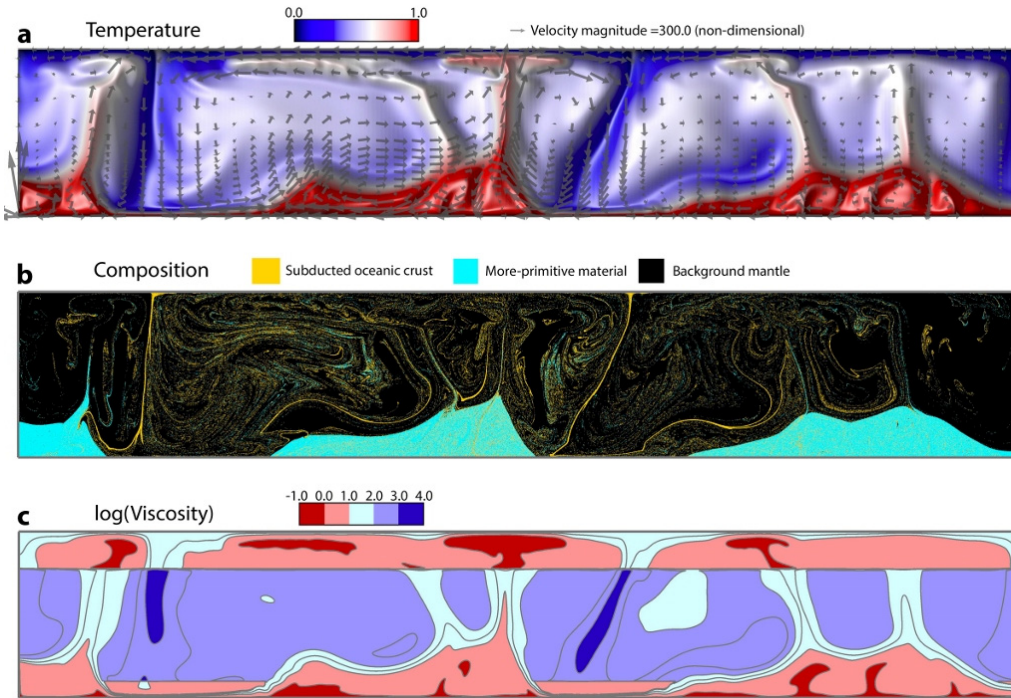
Figure 4.10. Snapshot of Case 4.6 at 828 Myrs. a, temperature field (non-dimensional) with mantle flow velocity superimposed (gray arrows). b, composition field with 3 components: oceanic crust (yellow), more-primitive material (cyan) and background mantle (black). c, logarithm of viscosity (non-dimensional). Gray lines are contours with an interval of 0.5. In this case, no additional viscosity reduction is applied to post-Perovskite.

Figure 4.11. Snapshot of Case 4.7 at 843 Myrs. a, temperature field (non-dimensional) with mantle flow velocity superimposed (gray arrows). b, composition field with 3 components: oceanic crust (yellow), more-primitive material (cyan) and background mantle (black). c, logarithm of viscosity (non-dimensional). Gray lines are contours with an interval of 0.5. In this case, a 10x viscosity reduction is applied to post-Perovskite.
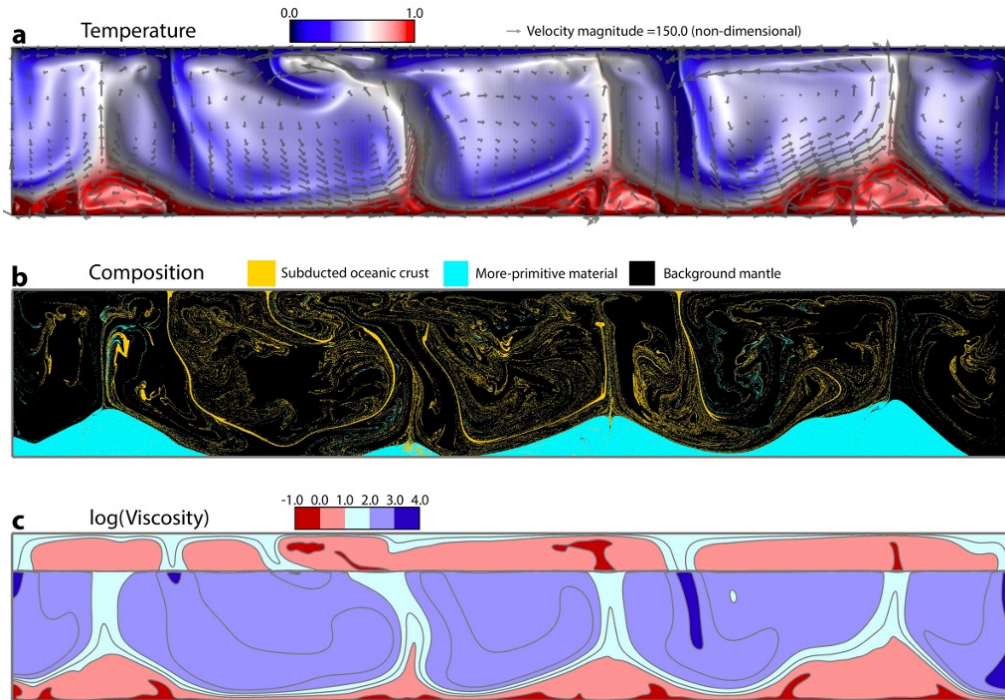
Figure 4.12. Snapshot of Case 4.8 at 839 Myrs. a, temperature field (non-dimensional) with mantle flow velocity superimposed (gray arrows). b, composition field with 3 components: oceanic crust (yellow), more-primitive material (cyan) and background mantle (black). c, logarithm of viscosity (non-dimensional). Gray lines are contours with an interval of 0.5. In this case, the Rayleigh number is Ra=5e6.
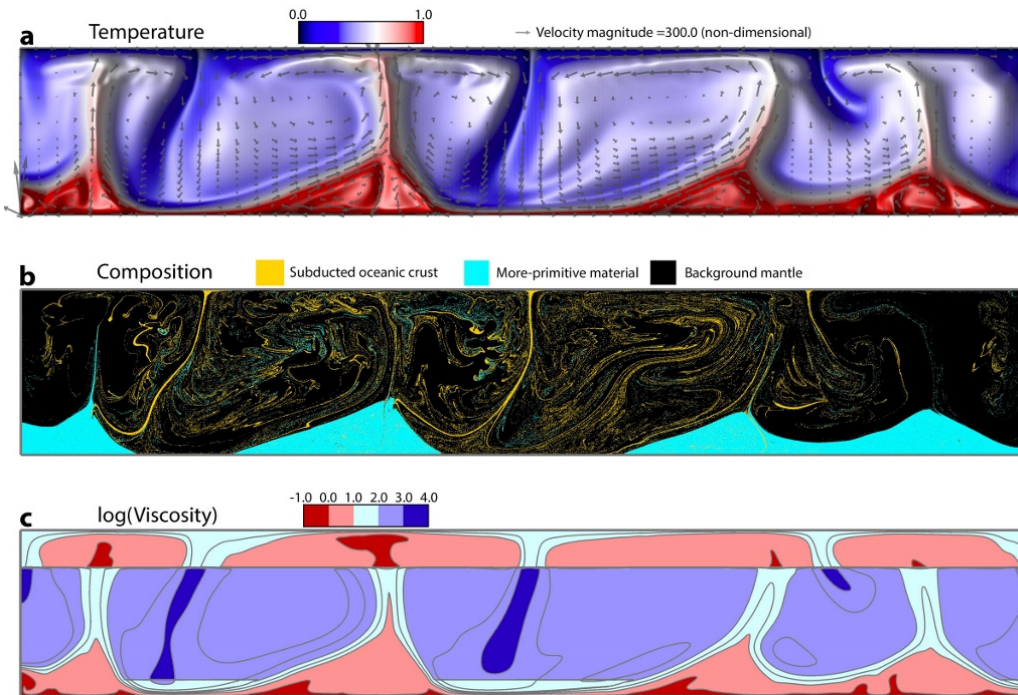
Figure 4.13. Snapshot of Case 4.9 at 828 Myrs. a, temperature field (non-dimensional) with mantle flow velocity superimposed (gray arrows). b, composition field with 3 components: oceanic crust (yellow), more-primitive material (cyan) and background mantle (black). c, logarithm of viscosity (non-dimensional). Gray lines are contours with an interval of 0.5. In this case, the Rayleigh number is Ra=5e7.
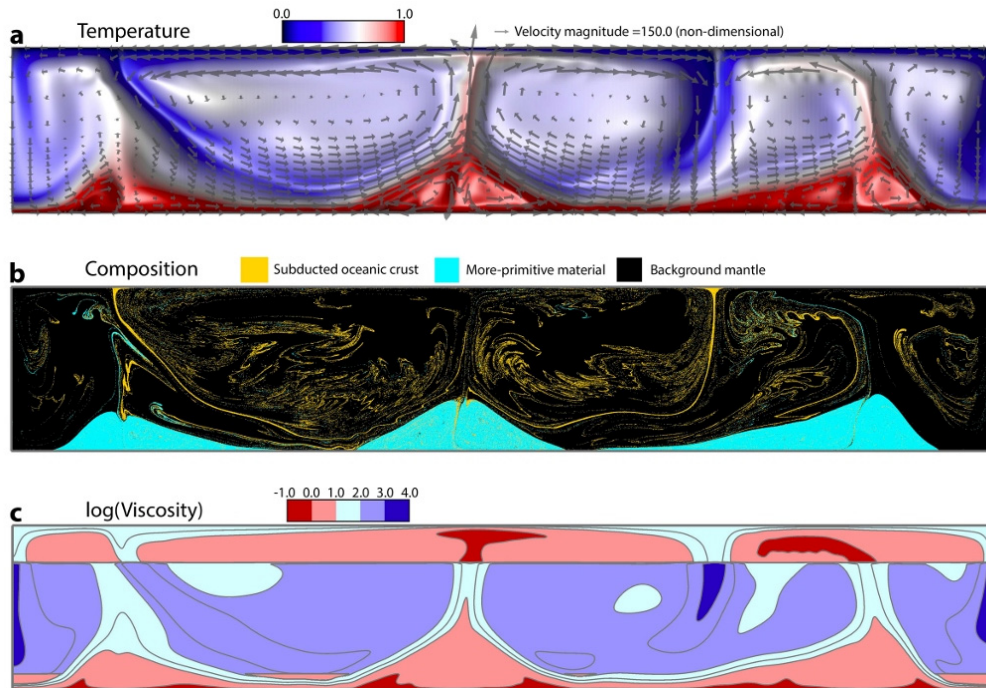
Figure 4.14. Snapshot of Case 4.10 at 855 Myrs. a, temperature field (non-dimensional) with mantle flow velocity superimposed (gray arrows). b, composition field with 3 components: oceanic crust (yellow), more-primitive material (cyan) and background mantle (black). c, logarithm of viscosity (non-dimensional). Gray lines are contours with an interval of 0.5. In this case, the activation energy is A=6.91, which leads to 1,000x temperature viscosity contrast between hottest and coldest regions.
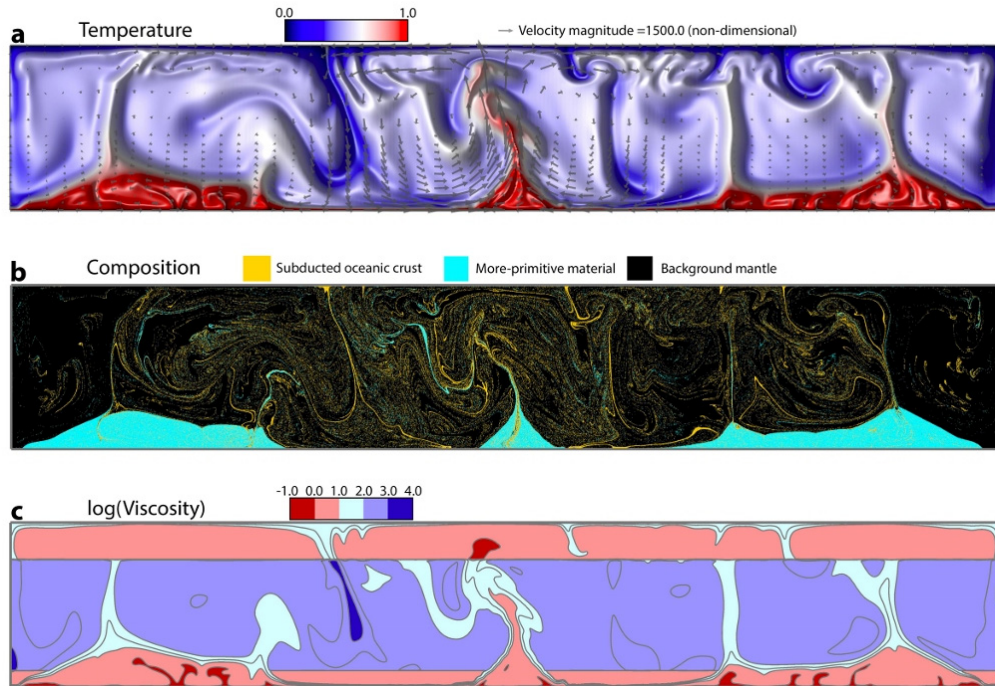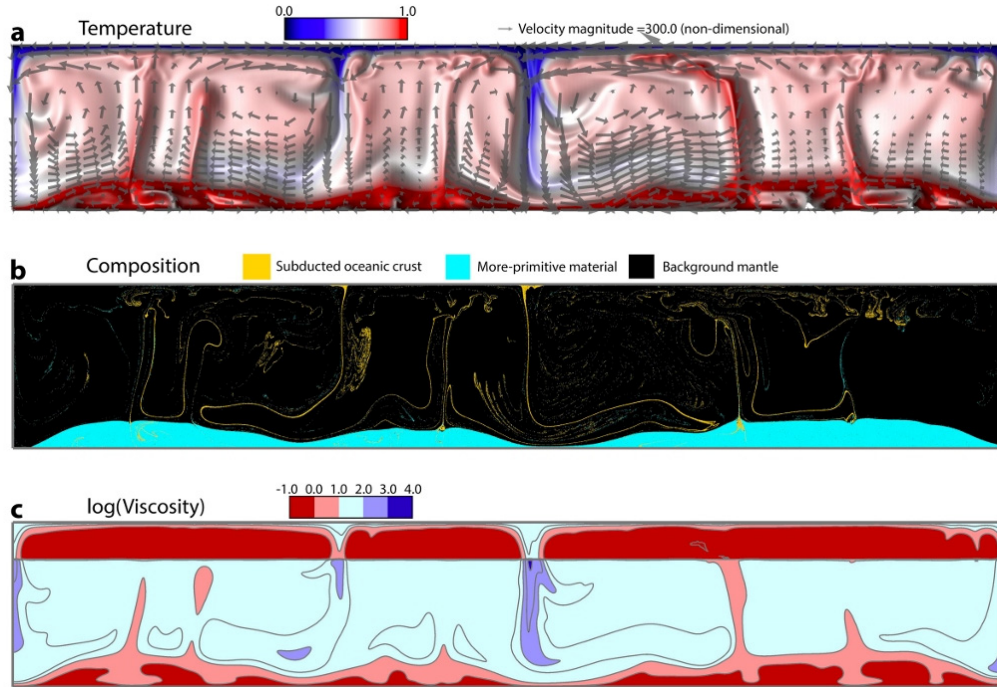
Figure 4.15. Snapshot of Case 4.11 at 343 Myrs. a, temperature field (non-dimensional) with mantle flow velocity superimposed (gray arrows). b, composition field with 3 components: oceanic crust (yellow), more-primitive material (cyan) and background mantle (black). c, logarithm of viscosity (non-dimensional). Gray lines are contours with an interval of 0.5. In this case, the internal heating is Q=20.
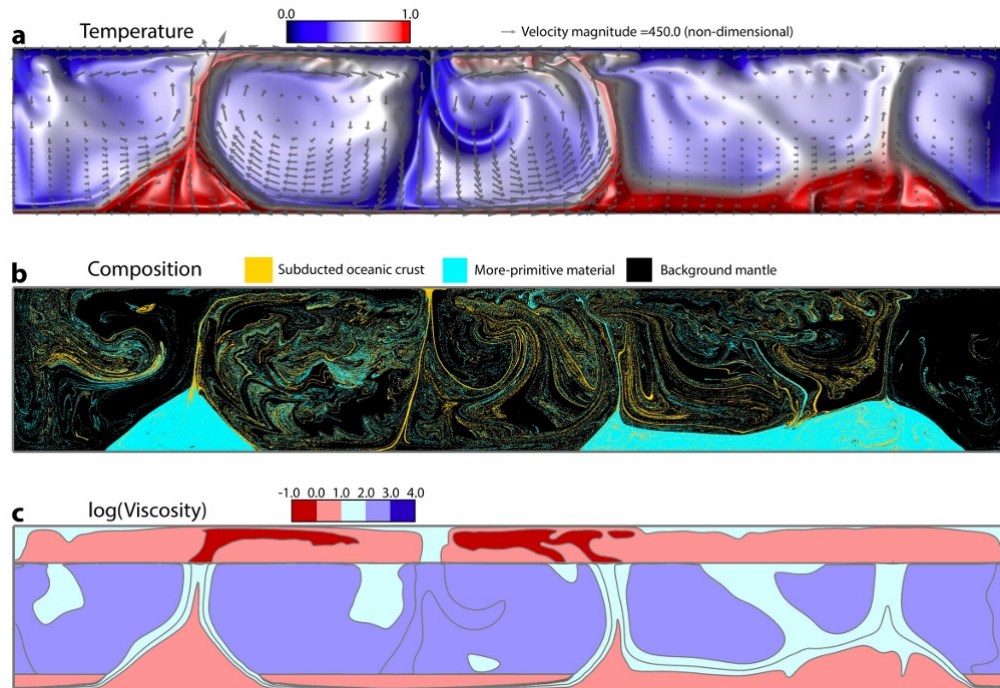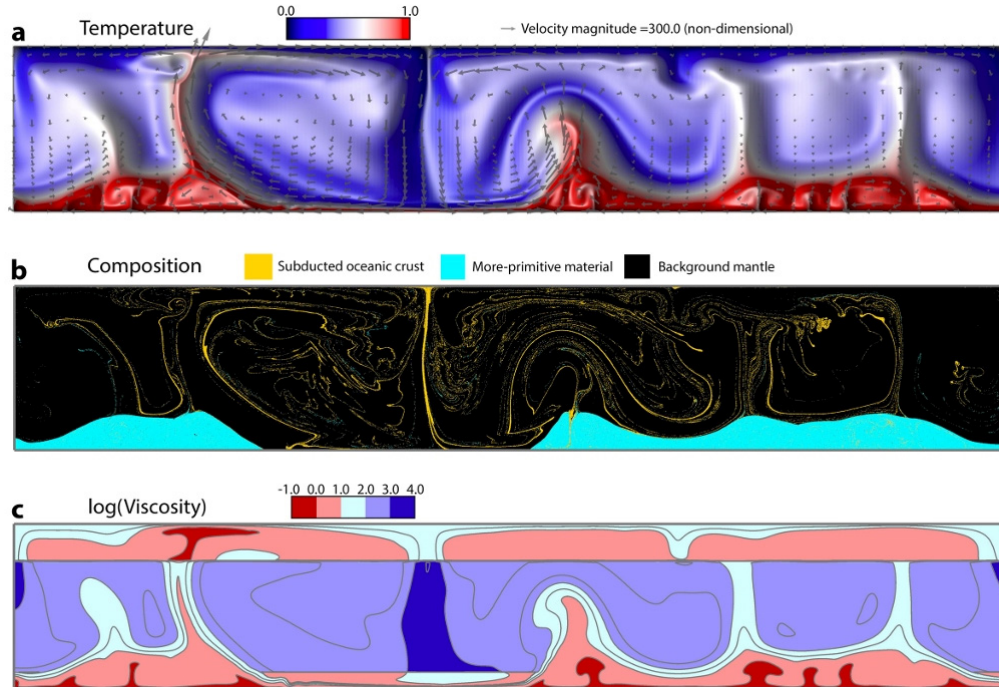
Figure 4.16. Snapshot of Case 4.12 at 653 Myrs. **a**, temperature field (non-dimensional) with mantle flow velocity superimposed (gray arrows). **b**, composition field with 3 components: oceanic crust (yellow), more-primitive material (cyan) and background mantle (black). **c**, logarithm of viscosity (non-dimensional). Gray lines are contours with an interval of 0.5. In this case, the buoyancy number for the more-primitive reservoir material is B_p =1.0.
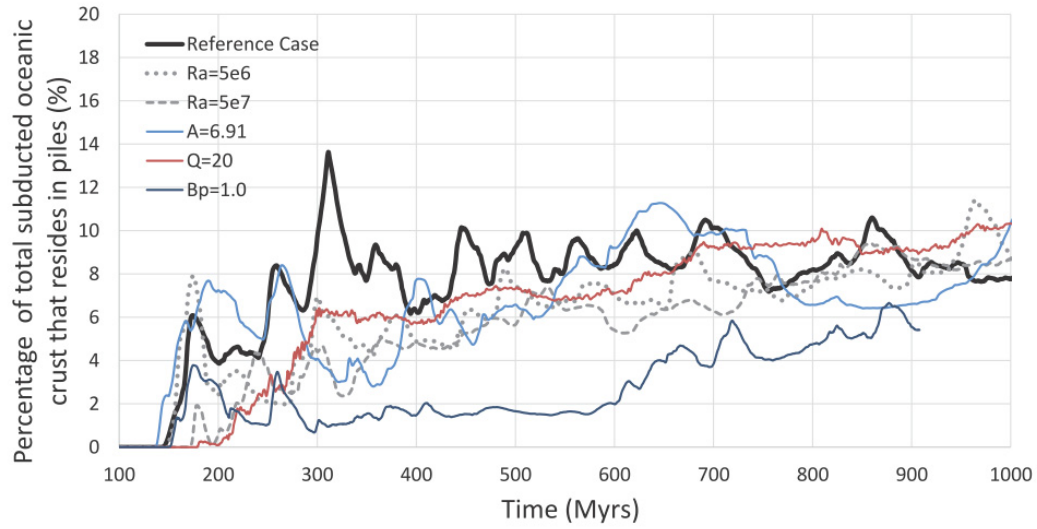
Figure 4.17. Percentage of total subducted oceanic crust that resides in piles as a function of time for Case 4.1 and Case 4.8-4.12. *Ra*: Rayleigh number; *A*: Activation parameter; *Q*: internal heating; B_p : Buoyancy number of the more-primitive material.

CHAPTER 5

INVESTIGATING THE ORIGIN OF ULTRA-LOW VELOCITY ZONES

5.1 Abstract

Discovering the origin of seismic anomalies in Earth's lowermost mantle, such as the large low shear velocity provinces (LLSVPs) beneath the central Pacific and Africa [*Garnero and McNamara*, 2008; *Dziewonski et al.*, 2010; *He and Wen*, 2012] and the much smaller-scale ultra-low velocity zones (ULVZs) observed in some localized regions on the core mantle boundary (CMB) [*Williams et al.*, 1998; *Rondenay and Fischer*, 2003; *Rost et al.*, 2005; *Hutko et al.*, 2009; *McNamara et al.*, 2010], provides important constraints on Earth's thermal and chemical evolution. While the LLSVPs are hypothesized to be caused by large-scale compositional heterogeneity in Earth's lowermost mantle[*Tackley*, 1998; *McNamara and Zhong*, 2005; *Labrosse et al.*, 2007; *Deschamps et al.*, 2012], one question centers on whether ULVZs are caused by additional, small-scale compositional heterogeneity or whether they are simply caused by partial melting of LLSVP material. Furthermore, it is important to determine whether the spatial distribution of ULVZs (relative to LLSVPs) can provide information as to their origin. Here, we present numerical experiments to demonstrate that if ULVZs have different composition than LLSVPs, they will preferentially accumulate into discontinuous patches of variable size and shape along the margins of LLSVPs; however, if ULVZs are caused by partial melting of LLSVP material, they would be located inboard from the edges of LLSVPs, where temperatures are highest. Our results suggest that ULVZs along the edges of LLSVPs are best explained by compositional

heterogeneity, while ULVZs located inside LLSVPs may be better (but not exclusively) explained by partial melting.

5.2 Introduction

ULVZs are seismic anomalies detected on the CMB with a significant reduction of seismic velocity (generally greater than 10%) and increased density [*Rost et al.*, 2005; *Rost et al.*, 2006]. Compared to the large-scale LLSVPs (covering ~21% area of the CMB and up to ~1000 km thick; [*Burke et al.*, 2008; *He and Wen*, 2012]), the ULVZs are much smaller structures (on the order of 10 km thick and 100 km across; [*Williams et al.*, 1998; *Rondenay and Fischer*, 2003; *Rost et al.*, 2005; *Hutko et al.*, 2009]). The LLSVPs are hypothesized to be caused by intrinsically more-dense material, possibly remnant from earlier differentiation events [*Labrosse et al.*, 2007; *Deschamps et al.*, 2012], that are swept to upwelling regions by downwelling subducted slabs [*McNamara and Zhong*, 2005]. However, the origin of ULVZs remains unclear. If ULVZs have the same composition as LLSVPs, ULVZs could be best explained by partial melting within the hottest regions of LLSVPs. Some seismic studies have found that S- and P-wave velocity of ULVZs are reduced by ~30% and ~10%, respectively [*Helmberger et al.*, 1998; *Williams et al.*, 1998; *Rost and Revenaugh*, 2003]. The 3-to-1 ratio of S and P velocity reduction of ULVZs is consistent with ~5-30% partial melting [*Williams and Garnero*, 1996]. Alternatively, if ULVZs have a different composition from LLSVPs (for example, enriched in iron; [*Wicks et al.*, 2010; *Bower et al.*, 2011]), the location of ULVZs would be largely controlled by mantle dynamics rather than temperature [*Hernlund and Jellinek*, 2010; *McNamara et al.*, 2010]. Previously proposed causes for compositional ULVZs include remnants of crystallization of Earth's early magma ocean [*Labrosse et al.*, 2007],

accumulation of banded iron formation at the CMB [*Dobson and Brodholt*, 2005], and

products of core mantle interaction [*Buffett et al.*, 2000; *Kanda and Stevenson*, 2006].

Previous two-dimensional numerical simulations have demonstrated that a small volume

of compositionally distinct and more-dense ULVZ material can be topographically

supported by mantle convection to form distinct accumulations of ULVZ along the

margins of thermochemical piles (which are hypothesized to cause LLSVPs) [*McNamara

et al.*, 2010]. However, two-dimensional studies cannot provide information on the three-

dimensional morphology of compositional ULVZs, so it remains unclear whether they

would be ubiquitously located along the edges of LLSVPs (like a ribbon) or form into

discontinuous patches.

5.3 Method

Here, we perform high resolution three-dimensional calculations to investigate the

morphology, distribution and dynamics of ULVZs by solving the following non-

dimensional equations for conservation of mass, momentum, and energy under the

Boussinesq approximation:

$$\nabla \cdot \vec{u} = 0 \tag{5.1}$$

$$-\nabla P + \nabla \cdot \left(\eta \bar{\bar{\varepsilon}} \right) = Ra(T - \sum_{i=1}^{n} B_i C_i)\hat{r} \tag{5.2}$$

$$\frac{\partial T}{\partial t} + (\vec{u} \cdot \nabla)T = \nabla^2 T + H \tag{5.3}$$

where, $\vec{u}$ is velocity, P is dynamic pressure, η is viscosity, $\bar{\bar{\varepsilon}}$ is strain rate tensor, T is

temperature, $\hat{r}$ is unit vector in radial direction, n is the number of compositional

components, B_i is the buoyancy number of the ith compositional component and C_i is the

corresponding composition fraction. The term $\sum_{i=1}^{n} B_i C_i$ in Eq. (5.2) is the summation of

chemical driving force or effective buoyancy number (hereafter denoted as F_c) from all compositional components. t is time and H is internal heating. Physical parameters in the above equations are all non-dimensional.

The thermal Rayleigh number Ra is defined as:

$$Ra = \frac{\rho_0 g \alpha_0 \Delta T D^3}{\eta_0 \kappa_0} \tag{5.4}$$

where ρ_0, α_0, ΔT, η_0 and κ_0 are dimensional reference values of background mantle density, thermal expansivity, temperature difference between core-mantle boundary and surface, reference viscosity at temperature $T = 0.6$ (non-dimensional), and thermal diffusivity, respectively. g and D are dimensional gravitational acceleration and mantle thickness, respectively.

The internal heating H is non-dimensionalized as:

$$H = \frac{D^2}{\kappa_0 c_{P_0} \Delta T} H^* \tag{5.5}$$

Here, c_{P_0} is heat capacity, H^* is the dimensional heal production rate.

The buoyancy number B is defined as the ratio between chemical density anomaly and density anomaly due to thermal expansion:

$$B = \frac{\Delta \rho}{\rho_0 \alpha_0 \Delta T} \tag{5.6}$$

Here, $\Delta \rho$ is intrinsic density difference between an individual compositional component and the background mantle.

The conservation equations of mass, momentum and energy are solved using our modified version of the code CitcomCU [*Zhong*, 2006] in the Boussinesq approximation. We employ a Rayleigh number Ra=9.4×10^6 for most cases. A 50x viscosity increase is

employed from upper mantle to lower mantle. The temperature dependent part of the viscosity is expressed as $\eta_T = \exp[A(0.6 - T)]$, where T is non-dimensional temperature, and we use a non-dimensional activation coefficient of A=9.21 for most cases, leading to a 10,000x viscosity range due to changes in temperature. Table 5.1 lists parameters for all cases used in this study.

The entire mantle convection system is modeled in a three-dimensional partial-sphere geometry (Figure 5.1a). The longitude of the model ranges from 30º to 120º, and the colatitude ranges from 30º to 150º. The model is divided into 512, 512 and 128 elements in longitude, colatitude and radial direction, respectively. The mesh is gradually refined towards the bottom of the model, resulting in a resolution of 5 km thick and ~14.5 km across for the lowermost 50 km. All boundaries are free-slip. Temperature boundary condition is isothermal on the top ($T = 0$) and at the bottom ($T = 1$), and insulating on the sides. The model is both heated from below and internally with an internal heating rate of $H = 12$.

The compositional field contains three compositional components: the background mantle, large-scale compositional heterogeneities (i.e., thermochemical piles) that resemble the LLSVPs (hereafter denoted as LLSVP material), and smaller scale compositional heterogeneities that resemble the ULVZs (herereafter denoted as ULVZ material). We developed a new hybrid tracer method to simulate the compositional field, in which the background mantle and the LLSVPs are modeled with ~710 million ratio tracers and the ULVZs are modeled with 50-110 million absolute tracers. The hybrid tracer method allows us to model both large-scale LLSVPs and much smaller scale ULVZs efficiently, with a much smaller number of total tracers, compared to each

122

method alone. The description and benchmark of hybrid tracer method are provided in Appendix A.

In order to develop an appropriate initial condition, we first carried out a lower resolution (192x192x128 elements) calculation with two compositional components (background mantle and LLSVP material) until it reached thermal equilibrium and large-scale thermochemical piles were established. Then, we interpolated the temperature and composition fields to higher resolution (512x512x128 elements). For LLSVP material, we employ a buoyancy number (defined in Supplementary Information) $B_{LLSVP} = 0.8$ which leads to them being ~2-3% denser than the background mantle for most cases (Table 5.1). For the cases that treat ULVZ as an additional component (cases 5.1, 5.3-5.9), a thin layer of ULVZ material was introduced to the bottom of the model, the thickness and density of which depends on the particular case.

5.4 Results

We first show the morphology and distribution of ULVZs under the hypothesis that ULVZs are caused by chemical heterogeneity. In Case 5.1, we initially introduced ULVZ materials with a buoyancy number of $B_{ULVZ} = 2.0$ (corresponding to ~5-10% denser than background mantle) in the lowermost 5 km of the mantle. Immediately after, the ULVZ material was advected by mantle flow toward the edges of LLSVPs, and later, accumulated into discontinuous patches with varying size and shape. Figure 5.1 shows a snapshot of this case at 227 Myr, from the start of the calculation. Figure 5.1a shows the LLSVP material (in gold) focused into piles by downwellings. Mantle plumes (red) arise from the tops of the piles. In Figure 5.1b (zoomed into the lower mantle), the pile is made partially transparent, and the compositional field at a depth of 5 km above the CMB is

displayed, illustrating the distribution and morphology of ULVZ material (ranging from green to red, depending on how diluted it has become from stirring with LLSVP material). We found that most of the ULVZ material is located within local accumulations at the edges of the piles, forming discrete patches of varying size (from ~100 km to ~1000 km). In addition, these accumulations have either round shape or linear morphologies, which provides important information about mantle flow velocity (discussed later in Figure 5.2). The thickness of the ULVZs ranges from 5 to 100 km (Figure 1c). Note that some ULVZ material is temporarily present (in transit) within pile interiors (due to either piles merging or being entrained into mantle flow within piles).

Figure 5.1d-f shows cross-sections of temperature superimposed on the compositional field at locations marked by gray cross-section lines in Figure 5.1b. The LLSVP material is swept into thermochemical piles beneath upwelling regions by downwellings, with ULVZ materials located at the edges of the piles. Some ULVZ material is stirred into the LLSVP material (e.g., Figure 5.1e). Regions outlined by gray boxes in Figure 5.1d-f are enlarged and shown in Figure 5.1g-h. Note that most ULVZs have an asymmetric shape, thicker on the outboard side of piles (Figure 5.1g, 5.1i), consistent with previous two-dimensional numerical modeling results[*McNamara et al.*, 2010].

Figure 5.2, 5.3 and 5.4 show a time sequence of snapshots for Case 5.1, illustrating the time-dependence of ULVZs. All three figures show the composition field at 5 km above the CMB, with mantle flow velocity arrows superimposed. At 121 Myr (Figure 5.2), two ULVZs (ULVZ #1 and #2) are located at the edges of the pile. At 160 Myr (Figure 5.3), ULVZ #2 is advected into a linear shape by mantle flow, whereas

ULVZ #1 maintains its round shape, being in a region where mantle flow velocity converges. At 227 Myr (Figure 5.4), ULVZ #2 is split into three parts: one migrates toward ULVZ #1, one forms into smaller scale ULVZ #3 with round shape, and the third part is entrained into the pile and stirred with LLSVP material (ULVZ #4). We observed that rounded ULVZs tended to be stable within regions with converging mantle flow velocity, whereas linear ULVZs were relatively quickly split into discrete smaller parts.

The alternative hypothesis for the origin of ULVZs is that they are caused by partial melting of LLSVP material [*Williams and Garnero*, 1996]. Figure 5.5 shows a snapshot at 218 Myr for Case 5.2, which does not include the additional compositional heterogeneity for ULVZ material. Figure 5.5a shows the temperature field at 5 km above the CMB. The hottest regions (marked by black contours, covering about 10% areas of the piles at this depth), and thus hypothetical locations of partial melt, occur inboard from the edges of the piles (pile edges are outlined by red lines).

Figure 5.5b shows a cross-section (marked by purple cross-section line in Figure 5.5a) of temperature field, superimposed with the composition field. The regions outlined by black boxes in Figure 5.5b are enlarged and shown in Figure 5.5c-d, superimposed with arrows of mantle flow velocity. We found that hot thermal instabilities (illustrated by black contours in Figure 5.5c-d) are developed within piles and are advected by mantle flow (illustrated by cyan arrows) toward their edges. Because the margins of piles are slightly cooled due to thermal diffusion with the cooler background mantle (further demonstrated in Appendix B), the hottest regions (red patches) occur significantly inboard from the pile edges.

We have calculated the distances between ULVZs and the edges of LLSVPs throughout the model run for both Case 5.1 and Case 5.2. First, the LLSVPs are defined as regions (grids) with $F_c > 0.1$. The ULVZs caused by additional compositional heterogeneity are defined as regions (grids) with $F_c > 1.5$. For ULVZs caused by partial melting, the melting temperature of LLSVP material is chosen to allow ~10% of LLSVP material is partially molten. Then, the closest distances between ULVZs and the edges of LLSVPs are calculated every 2.5 Myr. We exclude regions that are less than 500 km from side boundaries. Because for cases in which ULVZs are caused by additional compositional heterogeneity, it takes about 50 Myr for a layer of ULVZ material to be pushed to edges of LLSVPs, we thus exclude the first 50 Myr for these cases when calculating the distances between ULVZs and the edges of LLSVPs.

The distances between ULVZs and the edges of LLSVPs for all timesteps are summarized and shown in Figure 5.6. At all depths, the compositionally different ULVZ material (Case 5.1) is accumulated within local distances from the edges of LLSVPs; however, the distances between hottest regions of LLSVPs (or partial melting ULVZs, Case 5.2) and the edges of LLSVPs range from several hundred kilometers to over 1,500 km.

In cases 5.3-5.13, we investigate the effects of initial thickness of ULVZ material, density of ULVZ material, density of LLSVP material, temperature-dependence of and intrinsic viscosity of ULVZ material, and Rayleigh number. We found that although varying these parameters changes the details of dynamics (Figure 5.7-5.15), the overall fundamental conclusions about the morphology and distribution of ULVZs remain unchanged: (1) if ULVZs are chemically distinct from LLSVPs, ULVZs are

126

preferentially located along the edges of LLSVPs, with varying size and shape. ULVZ material may be temporarily located within LLSVPs when two or more LLSVPs merge together (Figure 5.7) or when ULVZ material is entrained into LLSVPs (Figure 5.1e). However, they are quickly advected to the edges of LLSVPs by mantle flow (Figure 5.7d). (2) If ULVZs are caused by partial melting of LLSVP material, they would be located inboard from the edges of LLSVPs.

Figure 5.7 shows a time series of snapshots for Case 5.3, in which the buoyancy number of ULVZ material is B=3.0. As the buoyancy number of ULVZ material increases, the amount of ULVZ material that is entrained into LLSVPs decreases, consistent with previous 2D numerical modeling results [*McNamara et al.*, 2010]. However, most ULVZ material is located along the edges of LLSVPs. We also found that some ULVZ material could be temporally located at the center of LLSVPs, however, it is quickly pushed to the edges of LLSVPs. For example, at 504 Myr, ULVZ #1 is located at the edges of LLSVPs (Figure 5.7a). At 538 Myr, ULVZ #1 is located at the center of LLSVPs because of the merging of LLSVPs (Figure 5.7b). However, this ULVZ is again pushed to the edges of LLSVPs at 608 Myr (Figure 5.7c).

Figure 5.8 shows the result of Case 5.4, in which the initial thickness of ULVZ material is doubled from 5 km in the reference case to 10 km. Although the initial volume of ULVZ material is two times as the reference case, the ULVZ material does not form a continuous ribbon along the edges of LLSVPs, but is pushed into discontinuous patches with variable size and shape along the edges of LLSVPs, similar to the reference case.

Figure 5.9 shows the result of Case 5.5, in which we employ a 100x viscosity reduction to the ULVZ material to simulating the dynamics of compositionally different

ULVZs which are partially molten. We found that as the viscosity of ULVZ material is reduced by 100 time, it becomes easier to be mixed with the LLSVP material in our calculations. Nevertheless, we found that most ULVZs are still located at the edges of LLSVPs, similar to the reference case.

We also investigated the effect of stronger temperature dependent viscosity on our results. In Figure 5.10, we show the results of Case 5.6, in which the temperature dependent of viscosity is increases to 100, 000x viscosity contrast due to changes of temperature. We did not find noticeable differences from our reference case.

In Figure 5.11, we higher the Rayleigh number to Ra=4.7e7 (Case 5.7). At higher Rayleigh number, the LLSVP material tends to form a continuous layer on the CMB. In order to generate isolated thermochemical piles, we also reduced the buoyancy number of LLSVP material to B=0.6. Because of higher Rayleigh number and higher density contrast between ULVZ and LLSVP material, the entrainment of ULVZ material into LLSVPs is impaired. However, ULVZs still tend to be located at the edges of LLSVPs, with varying size and shape.

In Figure 5.12, we increases the buoyancy number of LLSVP material to B=1.0 (Case 5.8). Although more ULVZ material tends to be entrained into LLSVPs due to reduced density contrast between ULVZ and LLSVP material, the major part ULVZ material remains at the edges of LLSVPs, similar to the reference case.

In Figure 5.13-5.15, we explored how temperature dependent viscosity, Rayleigh number and density of LLSVP material affect the location of hottest regions of LLSVPs. We found that in all of these cases (case 5.9-5.11), the hottest regions, or partial melting ULVZs, are located within and inboard from the edges of LLSVPs.

128

5.5 Discussion and Conclusion

In this study, we investigated two end-members of hypothetical origin for ULVZs. In reality, both types of ULVZs may co-exist. In addition, ULVZs caused by partial melting could be enriched in iron [*Nomura et al.*, 2011; *Jackson et al.*, 2014], which could increase the density [*Nomura et al.*, 2011] and lower the melting temperature of ULVZ material [*Boehler*, 1992; *Zerr and Boehler*, 1994]. In such case, these partially molten and compositionally-modified ULVZs would be advected by mantle flow to the edges of LLSVPs (shown in Case 5.5; Figure 5.9).

Here, we show that the relative distances between ULVZs and the edges of LLSVPs place significant constraints on the origin of ULVZs. Dozens of findings of ULVZs at the lowermost mantle have been reported (summarized by *McNamara et al.*, [2010]) by seismic waveform modeling studies. However, the precise lateral extent of these ULVZs remains unclear, mainly due to its trade-offs with seismic velocity anomaly. Past seismic tomography results also do not have enough resolution to show the locations of ULVZs and the edges of LLSVPs. As a result, the distribution of ULVZs respected to the edges of LLSVPs remains vague. Nonetheless, our results suggest that ULVZs at the edges of LLSVPs are caused by chemical heterogeneities (with or without partial melting) that are chemically distinct from LLSVPs and, ULVZs located within and off the edges of LLSVPs are better explained by partial melting in these regions. Future seismological studies should focus on the distribution and morphology of ULVZs, particularly the distance from the edges of LLSVPs and the shape of ULVZs, owing to their rich information about the origin of ULVZs and dynamics of Earth's lowermost mantle.

References

Boehler, R. (1992), Melting of the Fe-FeO and the Fe-FeS systems at high pressure: Constraints on core temperatures, *Earth and Planetary Science Letters*, *111*(2‑4), 217-227, doi:10.1016/0012-821X(92)90180-4.

Bower, D. J., J. K. Wicks, M. Gurnis, and J. M. Jackson (2011), A geodynamic and mineral physics model of a solid-state ultralow-velocity zone, *Earth and Planetary Science Letters*, *303*(3-4), 193-202, doi:10.1016/j.epsl.2010.12.035.

Buffett, B. A., E. J. Garnero, and R. Jeanloz (2000), Sediments at the Top of Earth's Core, *Science*, *290*(5495), 1338-1342, doi:10.1126/science.290.5495.1338.

Burke, K., B. Steinberger, T. H. Torsvik, and M. A. Smethurst (2008), Plume generation zones at the margins of large low shear velocity provinces on the core-mantle boundary, *Earth and Planetary Science Letters*, *265*(1-2), 49-60, doi:10.1016/j.epsl.2007.09.042.

Deschamps, F., L. Cobden, and P. J. Tackley (2012), The primitive nature of large low shear-wave velocity provinces, *Earth and Planetary Science Letters*, *349*(0), 198-208, doi:10.1016/j.epsl.2012.07.012.

Dobson, D. P., and J. P. Brodholt (2005), Subducted banded iron formations as a source of ultralow-velocity zones at the core-mantle boundary, *Nature*, *434*(7031), 371-374, doi:10.1038/Nature03385.

Dziewonski, A. M., V. Lekic, and B. A. Romanowicz (2010), Mantle Anchor Structure: An argument for bottom up tectonics, *Earth and Planetary Science Letters*, *299*(1-2), 69-79, doi:10.1016/j.epsl.2010.08.013.

Garnero, E. J., and A. K. McNamara (2008), Structure and Dynamics of Earth's Lower Mantle, *Science*, *320*(5876), 626-628, doi:10.1126/science.1148028.

He, Y., and L. Wen (2012), Geographic boundary of the "Pacific Anomaly" and its geometry and transitional structure in the north, *Journal of Geophysical Research*, *117*(B9), B09308, doi:10.1029/2012jb009436.

Helmberger, D. V., L. Wen, and X. Ding (1998), Seismic evidence that the source of the Iceland hotspot lies at the core-mantle boundary, *Nature*, *396*(6708), 251-255, doi:10.1038/24357.

Hernlund, J. W., and A. M. Jellinek (2010), Dynamics and structure of a stirred partially molten ultralow-velocity zone, *Earth and Planetary Science Letters*, *296*(1-2), 1-8, doi:10.1016/j.epsl.2010.04.027.

Hutko, A. R., T. Lay, and J. Revenaugh (2009), Localized double-array stacking analysis of PcP: D″ and ULVZ structure beneath the Cocos plate, Mexico, central Pacific, and north Pacific, *Physics of The Earth and Planetary Interiors*, *173*(1-2), 60-74, doi:10.1016/j.pepi.2008.11.003.

Jackson, C. R. M., L. B. Ziegler, H. Zhang, M. G. Jackson, and D. R. Stegman (2014), A geochemical evaluation of potential magma ocean dynamics using a parameterized model for perovskite crystallization, *Earth and Planetary Science Letters*, *392*(0), 154-165, doi:10.1016/j.epsl.2014.01.028.

Kanda, R. V. S., and D. J. Stevenson (2006), Suction mechanism for iron entrainment into the lower mantle, *Geophysical Research Letters*, *33*(2), doi:10.1029/2005gl025009.

Labrosse, S., J. W. Hernlund, and N. Coltice (2007), A crystallizing dense magma ocean at the base of the Earth's mantle, *Nature*, *450*(7171), 866-869, doi:10.1038/Nature06355.

McNamara, A. K., E. J. Garnero, and S. Rost (2010), Tracking deep mantle reservoirs with ultra-low velocity zones, *Earth and Planetary Science Letters*, *299*(1-2), 1-9, doi:10.1016/j.epsl.2010.07.042.

McNamara, A. K., and S. Zhong (2005), Thermochemical structures beneath Africa and the Pacific Ocean, *Nature*, *437*(7062), 1136-1139, doi:10.1038/nature04066.

Nomura, R., H. Ozawa, S. Tateno, K. Hirose, J. Hernlund, S. Muto, H. Ishii, and N. Hiraoka (2011), Spin crossover and iron-rich silicate melt in the Earth's deep mantle, *Nature*, *473*(7346), 199-202, doi:10.1038/Nature09940.

Rondenay, S., and K. M. Fischer (2003), Constraints on localized core-mantle boundary structure from multichannel, broadband SKS coda analysis, *Journal of Geophysical Research*, *108*(B11), 2537, doi:10.1029/2003jb002518.

Rost, S., E. J. Garnero, and Q. Williams (2006), Fine-scale ultralow-velocity zone structure from high-frequency seismic array data, *Journal of Geophysical Research*, *111*(B9), B09310, doi:10.1029/2005jb004088.

Rost, S., E. J. Garnero, Q. Williams, and M. Manga (2005), Seismological constraints on a possible plume root at the core-mantle boundary, *Nature*, *435*(7042), 666-669, doi:10.1038/Nature03620.

Rost, S., and J. Revenaugh (2003), Small-scale ultralow-velocity zone structure imaged by ScP, *Journal of Geophysical Research*, *108*(B1), 2056, doi:10.1029/2001jb001627.

Tackley, P. (1998), Three-Dimensional Simulations of Mantle Convection with a Thermo-Chemical Basal Boundary Layer: D"?, *AGU Geophysical Mongraph on the CMB ed. M. Gurnis*.

Wicks, J. K., J. M. Jackson, and W. Sturhahn (2010), Very low sound velocities in iron-rich (Mg,Fe)O: Implications for the core-mantle boundary region, *Geophysical Research Letters*, *37*, doi:10.1029/2010gl043689.

Williams, Q., and E. J. Garnero (1996), Seismic Evidence for Partial Melt at the Base of Earth's Mantle, *Science*, *273*(5281), 1528-1530, doi:10.1126/science.273.5281.1528.

Williams, Q., J. Revenaugh, and E. Garnero (1998), A correlation between ultra-low basal velocities in the mantle and hot spots, *Science*, *281*(5376), 546-549, doi:10.1126/science.281.5376.546.

Zerr, A., and R. Boehler (1994), Constraints on the melting temperature of the lower mantle from high-pressure experiments on MgO and magnesioustite, *Nature*, *371*(6497), 506-508, doi:10.1038/371506a0.

Zhong, S. J. (2006), Constraints on thermochemical convection of the mantle from plume heat flux, plume excess temperature, and upper mantle temperature, *Journal of Geophysical Research-Solid Earth*, *111*(B4), doi:10.1029/2005jb003972.

Table 5.1

Cases Used in Chapter 5.

Case	B_{ULVZ}	H_{ULVZ}	μ_{ULVZ}	A	Ra	B_{LLSVP}
1(REF)	2.0	5 km	1.0	9.21	9.4e6	0.8
2	N/A	N/A	N/A	9.21	9.4e6	0.8
3	**3.0**	5 km	1.0	9.21	9.4e6	0.8
4	2.0	**10 km**	1.0	9.21	9.4e6	0.8
5	2.0	5 km	**0.01**	9.21	9.4e6	0.8
6	2.0	5 km	1.0	**11.51**	9.4e6	0.8
7	2.0	5 km	1.0	9.21	**4.7e7**	**0.6**
8	2.0	5 km	1.0	9.21	9.4e6	**1.0**
9	N/A	N/A	N/A	**11.51**	9.4e6	0.8
10	N/A	N/A	N/A	9.21	**4.7e7**	**0.6**
11	N/A	N/A	N/A	9.21	9.4e6	**1.0**

REF: reference case; B_{ULVZ} : buoyancy number of ULVZ material; H_{ULVZ}: initial thickness of ULVZ material; μ_{ULVZ}: viscosity reduction of ULVZ material; A: activation coefficient; Ra: Rayleigh number; Numbers in bold are parameters whose value is different from the reference case. Parameters of cases in which ULVZs have different composition as LLSVPs are shown in green color; Parameters of cases with no additional ULVZ material are shown in red color.
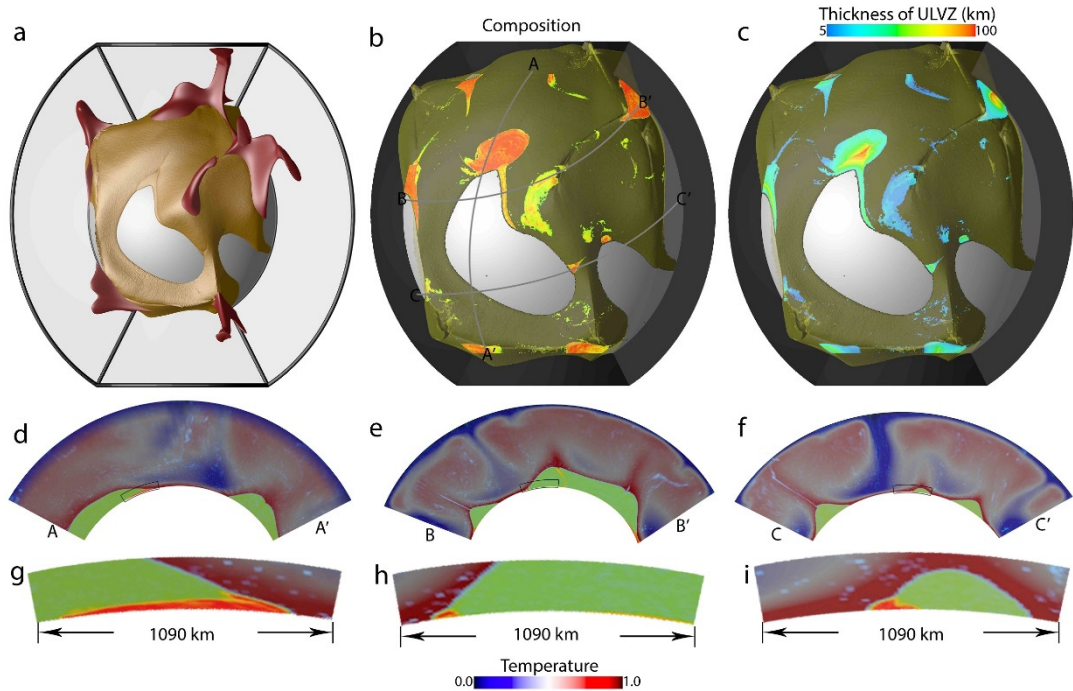
Figure 5.1. Snapshot of the reference case at 227 Myr, showing the morphology and distribution of ULVZs. a, LLSVP material (golden) forms into a pile at the lowermost mantle with mantle plumes forming on tops of the pile. The three dimensional partial spherical geometry of the model is outlined by black lines. The Earth's core (grey color) is exposed by removing downwelling slabs above it. b, composition field at 5 km above the CMB. Red: ULVZ material; green: LLSVP material; yellow: stirring between ULVZ and LLSVP material. c, thickness of ULVZs with partially transparent LLSVP materials superimposed (green). d-e, cross-sections of temperature field imposed with composition field at locations marked by gray cross-section lines in Figure 5.1b. g-h, zoomed-in at the regions outlined by black lines in Figure 5.1d-5.1f, respectively.
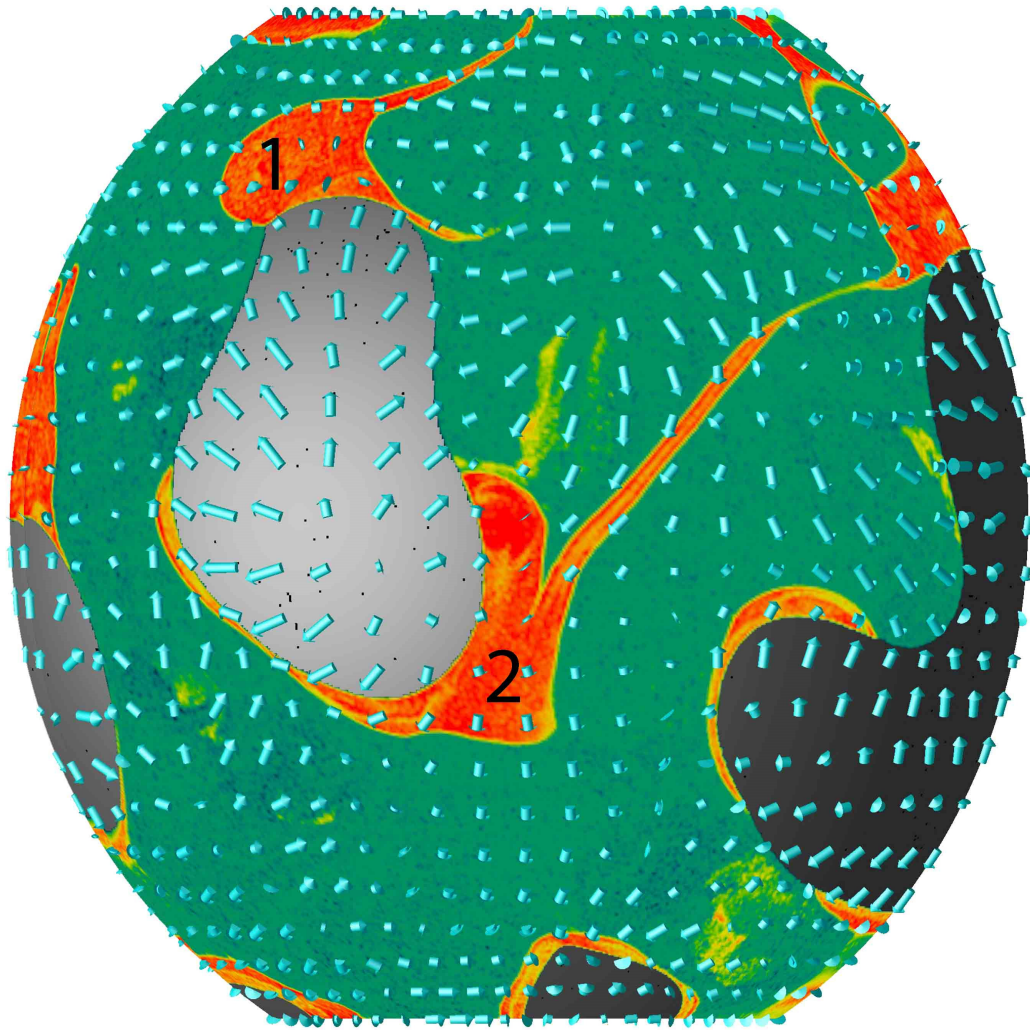
t=121 Myr

Velocity magnitude = 1000 (non-dimensional)

Figure 5.2. Snapshot of Case 5.1 at 121 Myr. Showing here is composition field at 5 km above the CMB, superimposed with mantle flow velocity (arrows). Red: ULVZ material; green: LLSVP material; yellow: stirring between ULVZ and LLSVP material. Gray color represents Earth's core.

Figure 5.3. Snapshot of Case 5.1 at 160 Myr. Showing here is composition field at 5 km above the CMB, superimposed with mantle flow velocity (arrows). Red: ULVZ material; green: LLSVP material; yellow: stirring between ULVZ and LLSVP material. Gray color represents Earth's core.
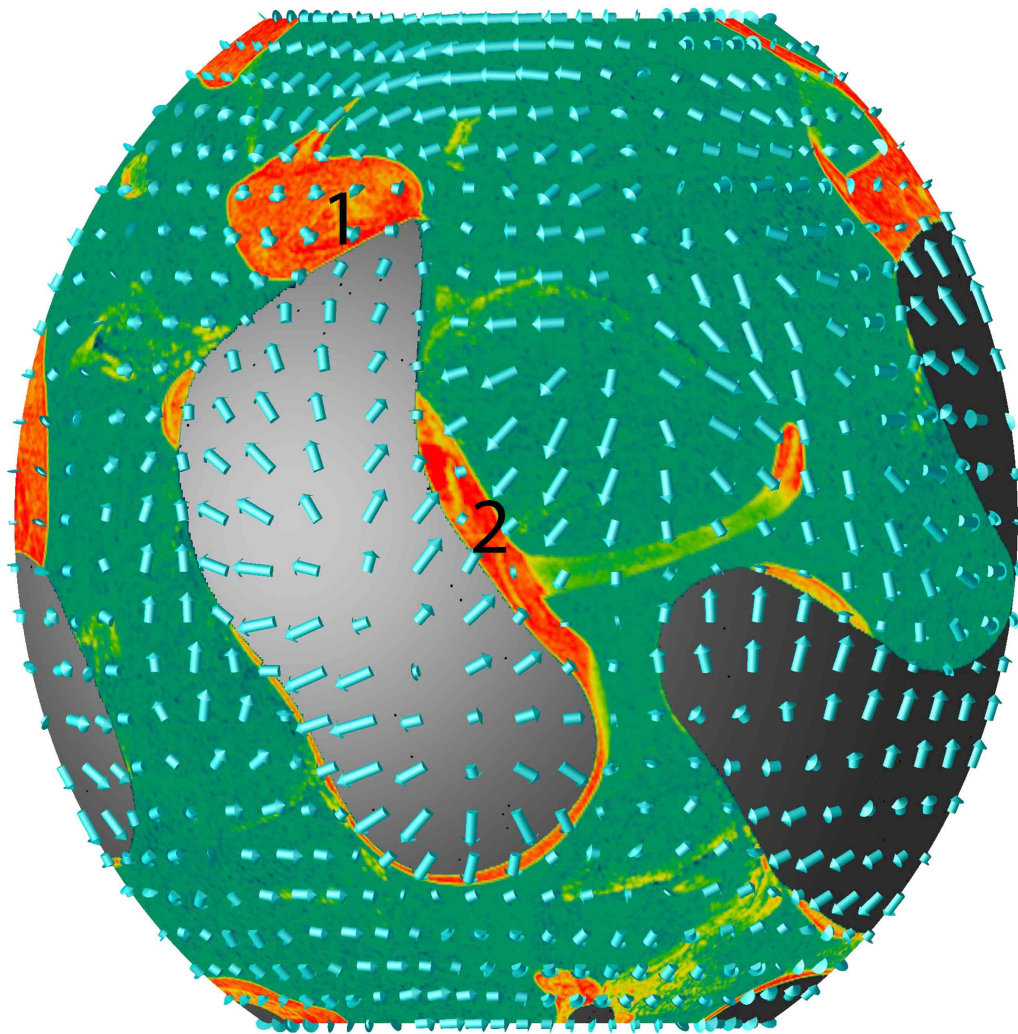
t=227 Myr

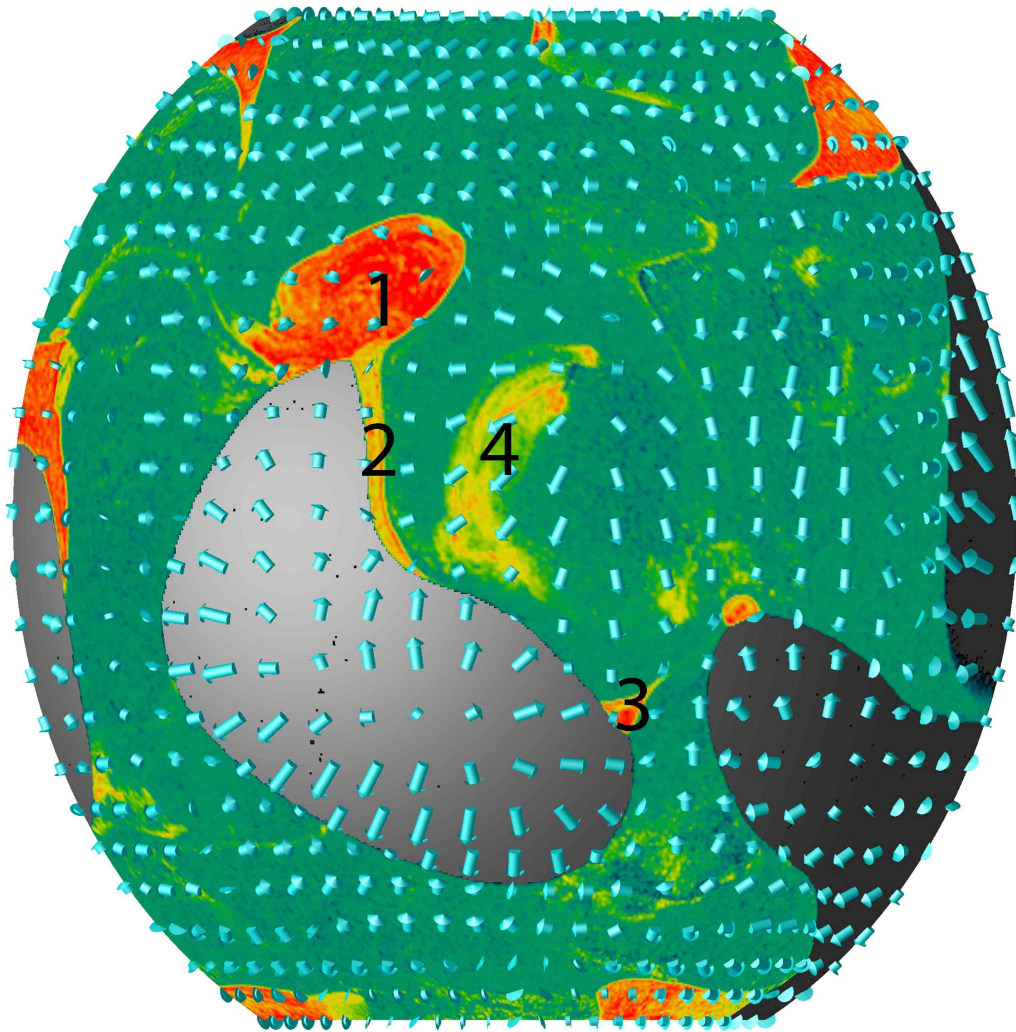→ Velocity magnitude = 1000 (non-dimensional)

Figure 5.4. Snapshot of Case 5.1 at 227 Myr. Showing here is composition field at 5 km above the CMB, superimposed with mantle flow velocity (arrows). Red: ULVZ material; green: LLSVP material; yellow: stirring between ULVZ and LLSVP material. Gray color represents Earth's core.
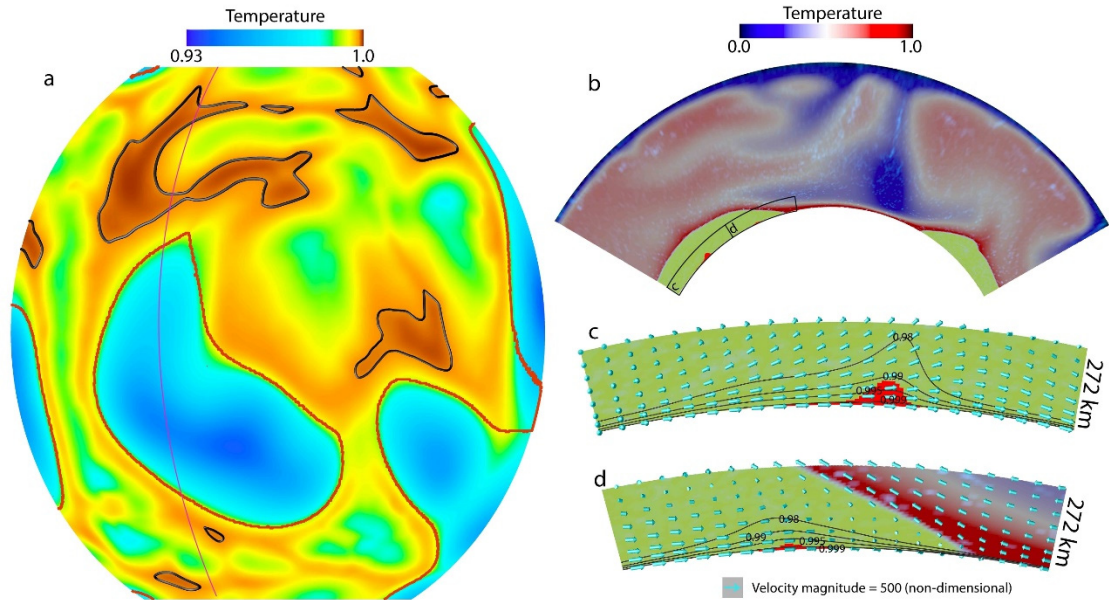
Figure 5.5. Snapshot of Case 5.2 at 218 Myr. a, Temperature field at 5 km above the CMB. Black contours show hottest regions with T>0.999 (non-dimensional). Red lines show the edges of LLSVPs. b, cross-sections of temperature field imposed with composition field at locations marked by purple cross-section lines in Figure 5.3a. Potential locations of ULVZs are shown as red patches. c-d, zoomed-in at the regions outlined by black lines in Figure 5.3b. Mantle flow velocity arrows are superimposed. Black lines show the temperature (non-dimensional) contours at T=0.98, 0.99, 0.995, and 0.999.
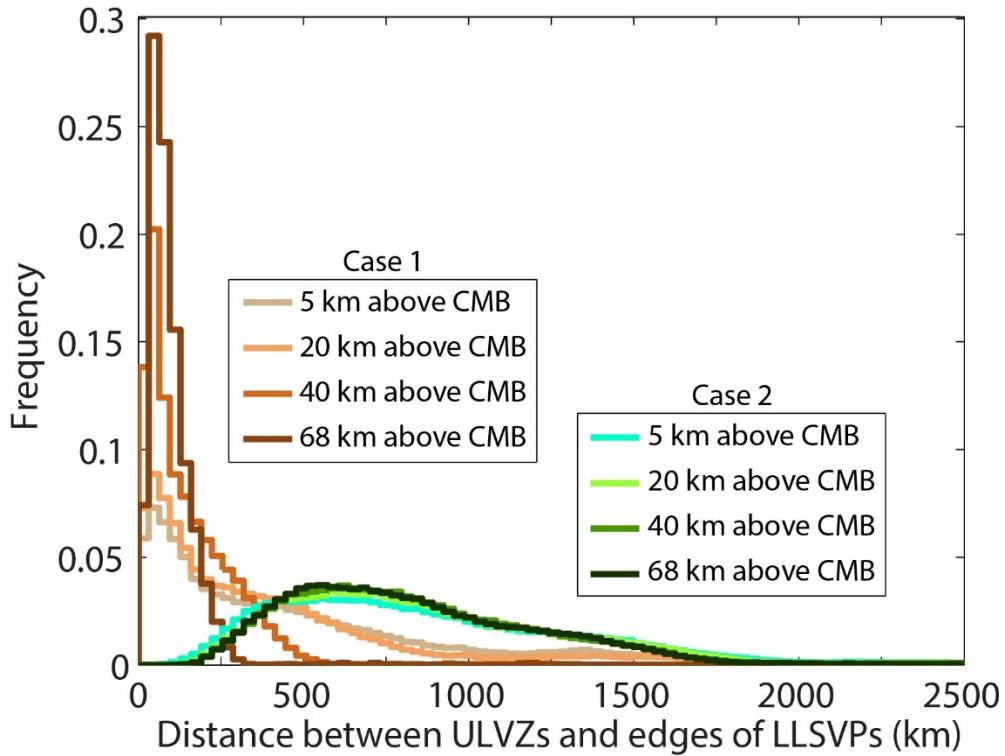
Figure 5.6. Distances between ULVZs and the edges of LLSVPs for Case 5.1 and Case 5.2. We calculated the distances throughout the model run, but excluding the first 50 Myr for Case 5.1 because during this time most ULVZ material is on its way to the edges of LLSVPs. We excludes ULVZs that are less than 500 km from side boundaries. The y-axis of the histograms is normalized with the total number of ULVZ samples for each case.
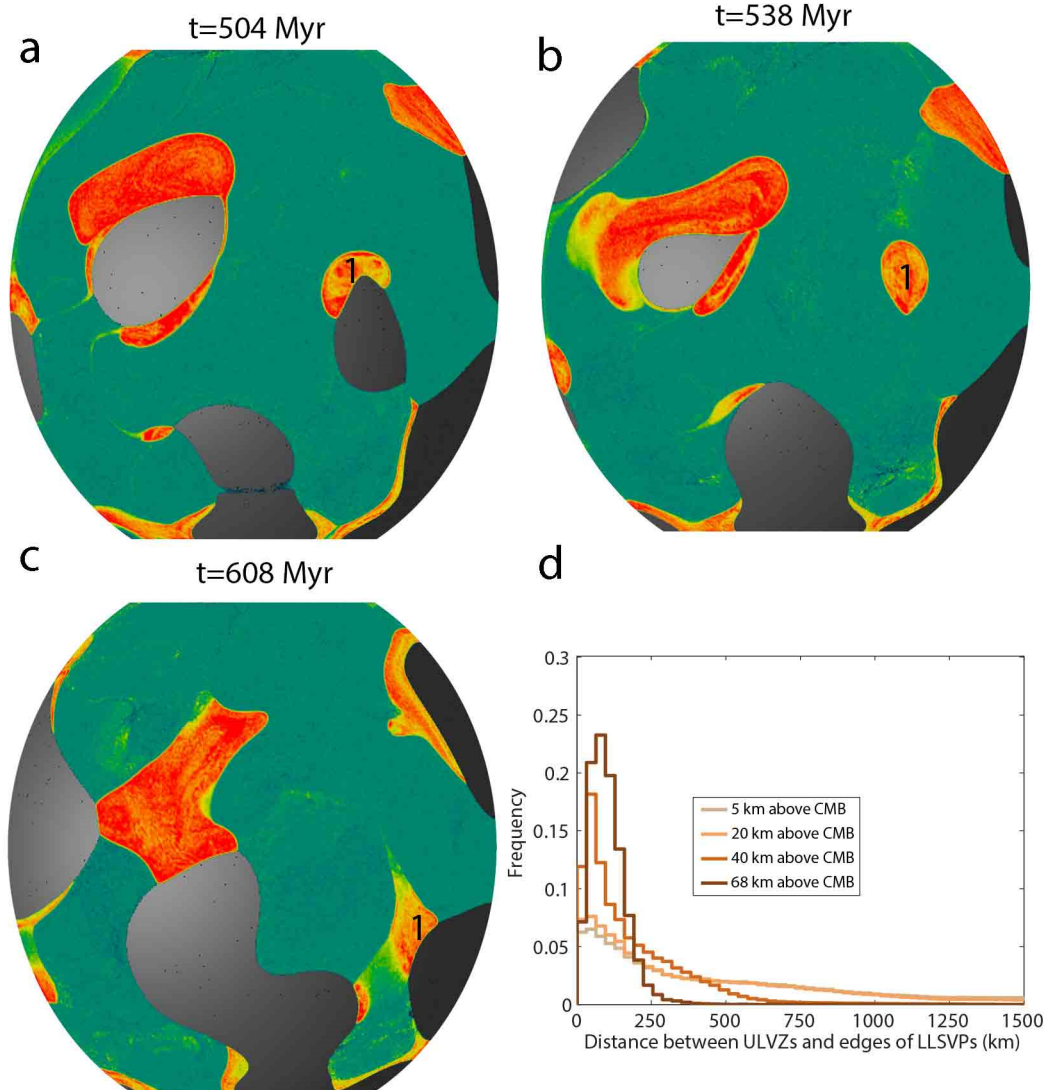
Figure 5.7. Mechanism of locating compositionally different ULVZs within LLSVPs. a-c, snapshots showing the composition field at 5 km above the CMB for Case 5.3, in which the buoyancy number of ULVZ material is B=3.0. Red: ULVZ material; green: LLSVP material; yellow: stirring between ULVZ and LLSVP material. a, Mantle flow velocity starts to converge around ULVZ #1. b, ULVZ #1 with round shape forms in the center of LLSVPs. c, ULVZ #1 is moved to the edges of LLSVPs. d, Distances between ULVZ material and the edges of LLSVPs.
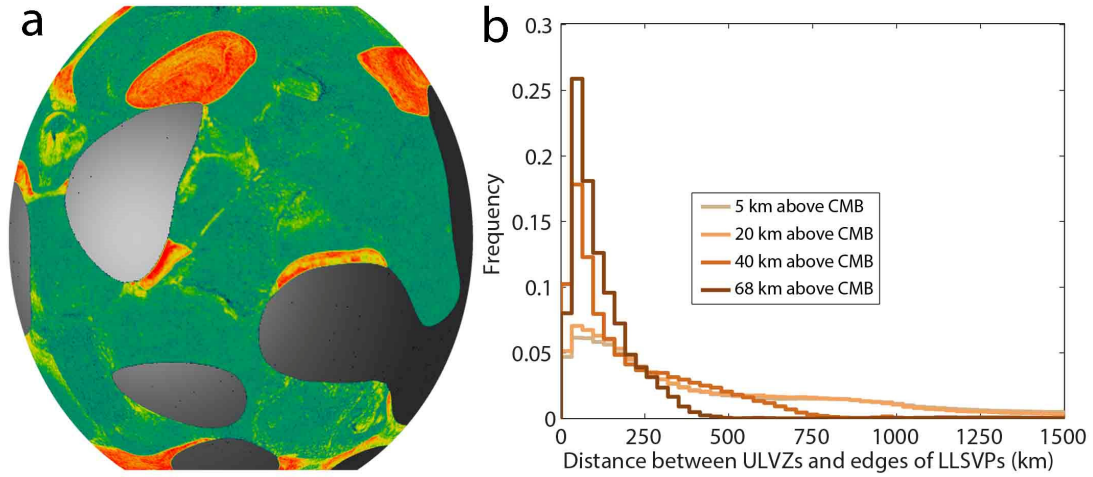
Figure 5.8. Snapshot for Case 5.4 at 462 Myr, in which the initial thickness of ULVZ material is 10 km. a, composition field at 5 km above the CMB. Red: ULVZ material; green: LLSVP material; yellow: stirring between ULVZ and LLSVP material. b, Distances between ULVZ material and the edges of LLSVPs.

Figure 5.9. Snapshot for Case 5.5 at 144 Myr, in which a 100x viscosity reduction (in addition to the reduction due to temperature-dependence) is applied to the ULVZ material, in addition to temperature dependent viscosity. **a**, composition field at 5 km above the CMB. Red: ULVZ material; green: LLSVP material; yellow: stirring between ULVZ and LLSVP material. **b**, Distances between ULVZ material and the edges of LLSVPs.

Figure 5.10. Snapshot for Case 5.6 at 166 Myr, in which the temperature dependent of viscosity is A=11.51, leading to 100,000x viscosity contrast due to temperature. a, composition field at 5 km above the CMB. Red: ULVZ material; green: LLSVP material; yellow: stirring between ULVZ and LLSVP material. b, Distances between ULVZ material and the edges of LLSVPs.
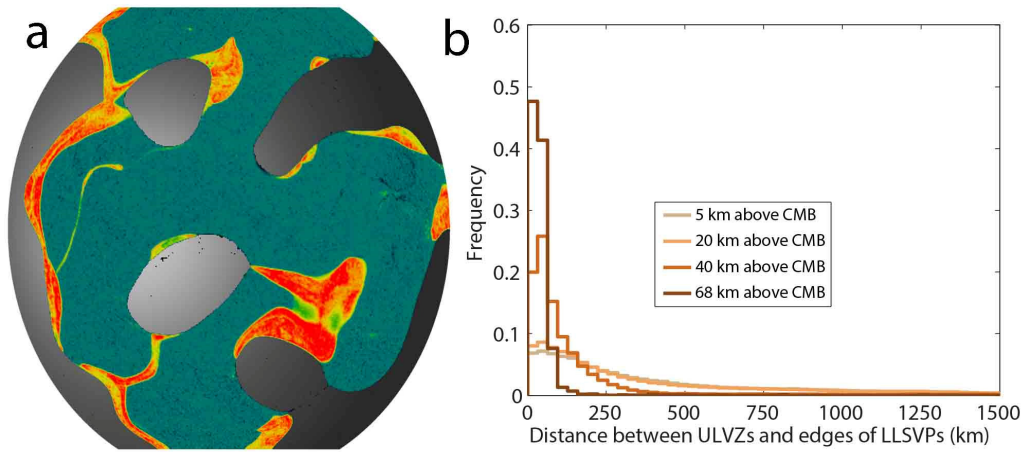
Figure 5.11. Snapshot for Case 5.7 at 466 Myr, in which the Rayleigh number is Ra=4.7e7 and the buoyancy number for the LLSVP material is $B = 0.6$. **a**, composition field at 5 km above the CMB. Red: ULVZ material; green: LLSVP material; yellow: stirring between ULVZ and LLSVP material. **b**, Distances between ULVZ material and the edges of LLSVPs.

Figure 5.12. Snapshot for Case 5.8 at 281 Myr, in which the buoyancy number for the LLSVP material is B=1.0. **a**, composition field at 5 km above the CMB. Red: ULVZ material; green: LLSVP material; yellow: stirring between ULVZ and LLSVP material. **b**, Distances between ULVZ material and the edges of LLSVPs.
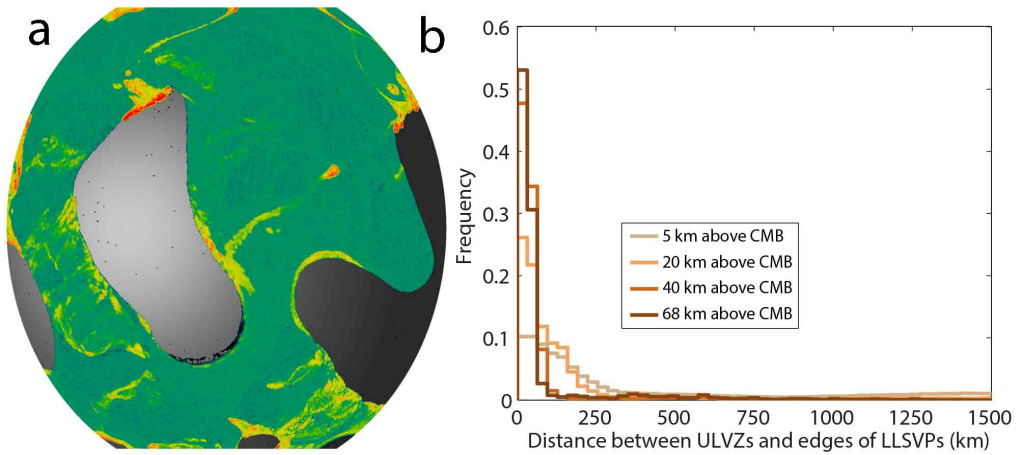
a

b

Temperature

0.93 | | 1.0
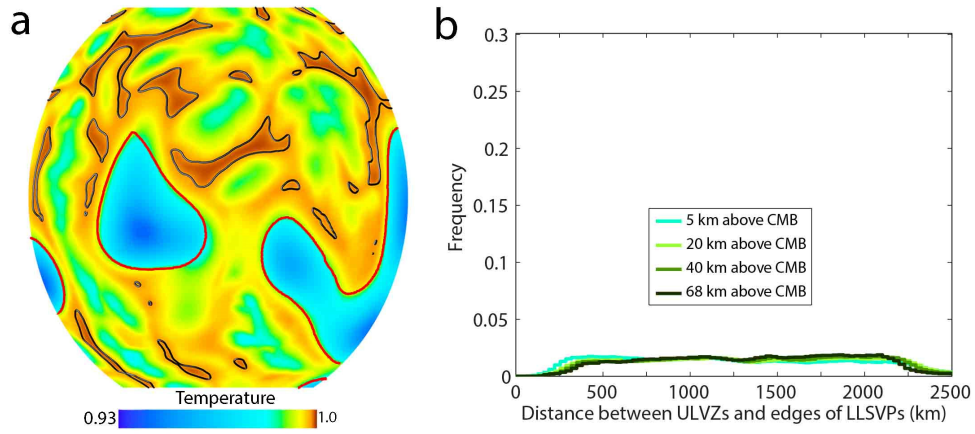
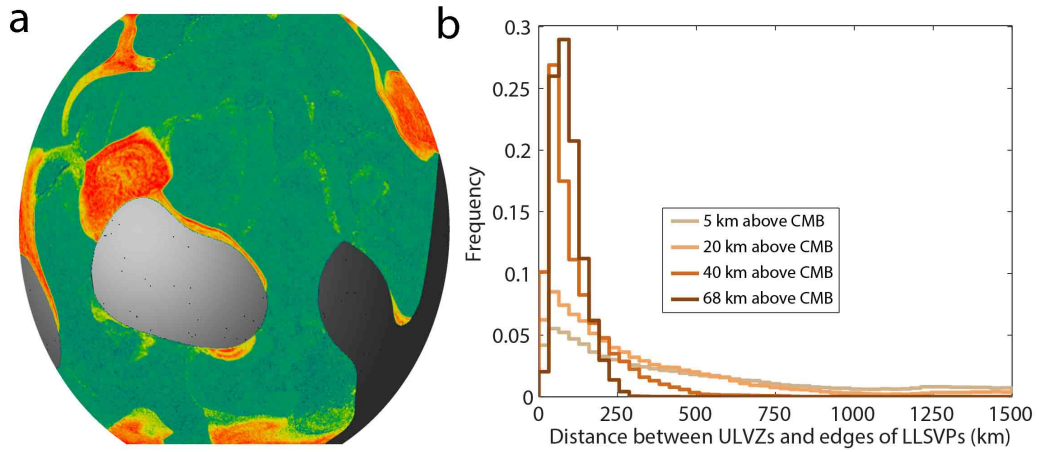*Figure 5.13*. Snapshot for Case 5.9 at 108 Myr, in which the temperature dependent of viscosity is A=11.51, leading to 100,000x visocisty contrast due to temperature. a, temperature field at 5 km above the CMB. Black contours show hottest regions. Red lines show the edges of LLSVPs. b, Distances of hottest regions of LLSVPs, or partial melting ULVZs, from the edges of LLSVPs.
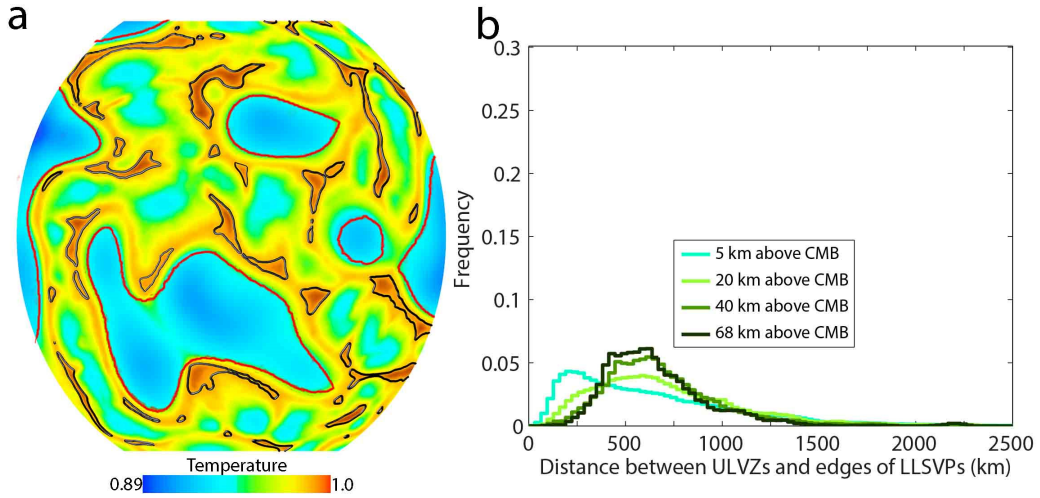
Figure 5.14. Snapshot for Case 5.10 at 393 Myr, in which the Rayleigh number is Ra=4.7e7 and the buoyancy number for the LLSVP material is $B = 0.6$. a, temperature field at 5 km above the CMB. Black contours show hottest regions. Red lines show the edges of LLSVPs. b, Distances of hottest regions of LLSVPs, or partial melting ULVZs, from the edges of LLSVPs.

a

b
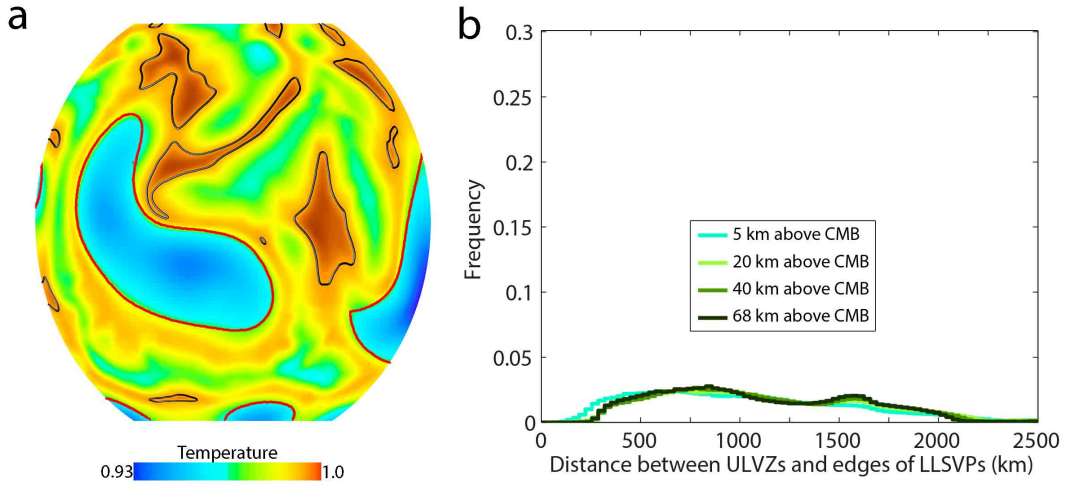
Temperature
0.93 — 1.0

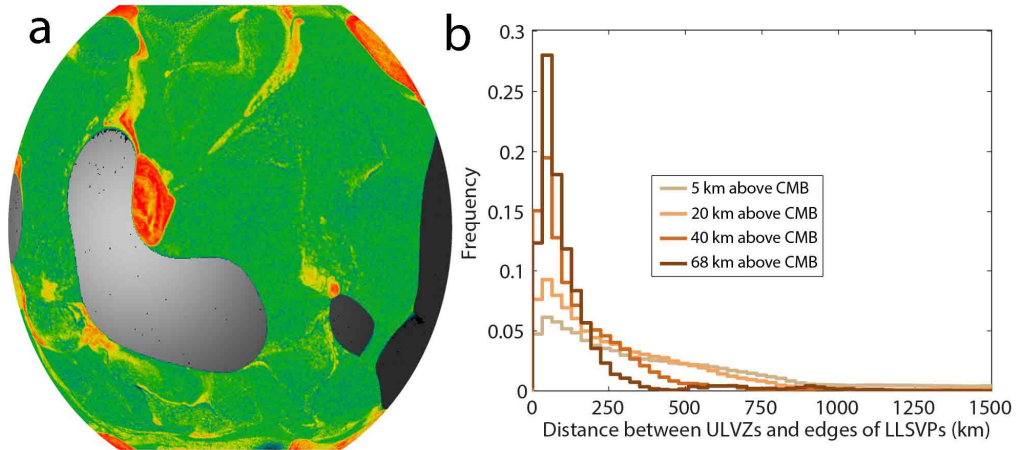*Figure 5.15*. Snapshot for Case 5.11 at 312 Myr, in which the buoyancy number for the LLSVP material is $B = 1.0$. a, temperature field at 5 km above the CMB. Black contours show hottest regions. Red lines show the edges of LLSVPs. b, Distances of hottest regions of LLSVPs, or partial melting ULVZs, from the edges of LLSVPs.

148

CHAPTER 6

FINAL SYNOPSIS

In this dissertation, I performed numerical calculations to investigate the thermochemical structure and dynamics of Earth's lowermost mantle.

In Chapter 2, I described the equations for conservation of mass, momentum energy and numerical method used to solve these equations.

In Chapter 3, we performed high resolution 2D calculations to study the possibility of subducted oceanic crust to accumulate at the core-mantle boundary. We found that as the oceanic crust is subducted to the lowermost mantle, the majority of it is entrained up by upwelling mantle plumes and stirred into the background mantle. Only a small amount of the subducted oceanic crust could accumulate at the core-mantle boundary, but it is consistently entrained away into mantle plumes. Under current Earth-like condition, it is difficult for the thin (~6 km) subducted oceanic crust to accumulate at the CMB into large scales as that of LLSVPs.

In Chapter 4, we studies the interaction between mantle plumes, subducted oceanic crust and more-primitive reservoir. We found that the subducted oceanic crust takes multiple pathways as it is subducted to the lowermost mantle. While some part of the crust is directly entrained into mantle plumes without contacting the more-primitive reservoir, a significant of it (up to 10%) enters the more-primitive reservoir and undergoes vigorous stirring with the more-primitive material. As a result, plumes forming on top of the more-primitive reservoir entrain a varying combination of more-primitive material, oceanic crust with varying ages and background mantle. The result reconciles geochemical observation of multiple compositional components and varying ages of

149

oceanic crust in the source of ocean-island basalts. In addition, this provides explanation to the seismic heterogeneities within the LLSVPs.

In Chapter 5, we performed 3D high resolution numerical calculations to investigate the morphology and distribution of ULVZs. We found if ULVZs are caused by chemical heterogeneities with different composition as LLSVPs, ULVZs tend to be located at the edges of LLSVPs. Alternatively, if ULVZs are caused by partial melting within the hottest regions of LLSVPs, ULVZs will be located in board and off the edges of LLSVPs. The results indicate that ULVZs at the edges of LLSVPs are best explained by distinct compositional heterogeneity and ULVZs insider to LLSVPs are better explained by partial melting of LLSVP material.

REFERENCES

Allegre, C. J., and D. L. Turcotte (1986), Implications of a two-component marble-cake mantle, *Nature*, *323*(6084), 123-127, doi:10.1038/323123a0.

Ammann, M. W., J. P. Brodholt, J. Wookey, and D. P. Dobson (2010), First-principles constraints on diffusion in lower-mantle minerals and a weak D" layer, *Nature*, *465*(7297), 462-465, doi:10.1038/nature09052.

Anders, E., and M. Ebihara (1982), Solar-system abundances of the elements, *Geochimica et Cosmochimica Acta*, *46*(11), 2363-2380, doi:10.1016/0016-7037(82)90208-3.

Anders, E., and N. Grevesse (1989), Abundances of the elements: Meteoritic and solar, *Geochimica et Cosmochimica Acta*, *53*(1), 197-214, doi:10.1016/0016-7037(89)90286-X.

Andrault, D., N. Bolfan-Casanova, G. L. Nigro, M. A. Bouhifd, G. Garbarino, and M. Mezouar (2011), Solidus and liquidus profiles of chondritic mantle: Implication for melting of the Earth across its history, *Earth and Planetary Science Letters*, *304*(1-2), 251-259, doi:10.1016/j.epsl.2011.02.006.

Andrault, D., G. Pesce, M. A. Bouhifd, N. Bolfan-Casanova, J.-M. Hénot, and M. Mezouar (2014), Melting of subducted basalt at the core-mantle boundary, *Science*, *344*(6186), 892-895, doi:10.1126/science.1250466.

Avants, M., T. Lay, and E. J. Garnero (2006), A new probe of ULVZ S-wave velocity structure: Array stacking of ScS waveforms, *Geophysical Research Letters*, *33*(7), L07314, doi:10.1029/2005gl024989.

Badro, J. (2014), Spin Transitions in Mantle Minerals, *Annual Review of Earth and Planetary Sciences*, *42*(1), 231-248, doi:10.1146/annurev-earth-042711-105304.

Beuchert, M. J., and H. Schmeling (2013), A melting model for the lowermost mantle using Clapeyron slopes derived from experimental data: Consequences for the thickness of ultralow velocity zones (ULVZs), *Geochemistry Geophysics Geosystems*, *14*(1), 197-208, doi:10.1029/2012gc004356.

Boehler, R. (1992), Melting of the Fe-FeO and the Fe-FeS systems at high pressure: Constraints on core temperatures, *Earth and Planetary Science Letters*, *111*(2‑4), 217-227, doi:10.1016/0012-821X(92)90180-4.

Bourdon, B., M. Touboul, G. Caro, and T. Kleine (2008), Early differentiation of the Earth and the Moon, *Philosophical Transactions of the Royal Society A: Mathematical, Physical and Engineering Sciences*, *366*(1883), 4105-4128, doi:10.1098/rsta.2008.0125.

Bower, D. J., M. Gurnis, J. M. Jackson, and W. Sturhahn (2009), Enhanced convection and fast plumes in the lower mantle induced by the spin transition in ferropericlase, *Geophysical Research Letters*, *36*(10), L10306, doi:10.1029/2009gl037706.

Bower, D. J., J. K. Wicks, M. Gurnis, and J. M. Jackson (2011), A geodynamic and mineral physics model of a solid-state ultralow-velocity zone, *Earth and Planetary Science Letters*, *303*(3-4), 193-202, doi:10.1016/j.epsl.2010.12.035.

Brandenburg, J. P., and P. E. van Keken (2007), Deep storage of oceanic crust in a vigorously convecting mantle, *Journal of Geophysical Research*, *112*(B6), B06403, doi:10.1029/2006jb004813.

Brandon, A. D., and R. J. Walker (2005), The debate over core-mantle interaction, *Earth and Planetary Science Letters*, *232*(3-4), 211-225, doi:10.1016/j.epsl.2005.01.034.

Buffett, B. A., E. J. Garnero, and R. Jeanloz (2000), Sediments at the Top of Earth's Core, *Science*, *290*(5495), 1338-1342, doi:10.1126/science.290.5495.1338.

Bull, A. L., M. Domeier, and T. H. Torsvik (2014), The effect of plate motion history on the longevity of deep mantle heterogeneities, *Earth and Planetary Science Letters*, *401*(0), 172-182, doi:10.1016/j.epsl.2014.06.008.

Bull, A. L., A. K. McNamara, T. W. Becker, and J. Ritsema (2010), Global scale models of the mantle flow field predicted by synthetic tomography models, *Physics of The Earth and Planetary Interiors*, *182*(3-4), 129-138, doi:10.1016/j.pepi.2010.03.004.

Bull, A. L., A. K. McNamara, and J. Ritsema (2009), Synthetic tomography of plume clusters and thermochemical piles, *Earth and Planetary Science Letters*, *278*(3-4), 152-162, doi:10.1016/j.epsl.2008.11.018.

Bunge, H.-P., M. A. Richards, C. Lithgow-Bertelloni, J. R. Baumgardner, S. P. Grand, and B. A. Romanowicz (1998), Time Scales and Heterogeneous Structure in Geodynamic Earth Models, *Science*, *280*(5360), 91-95, doi:10.1126/science.280.5360.91.

Burke, K., B. Steinberger, T. H. Torsvik, and M. A. Smethurst (2008), Plume generation zones at the margins of large low shear velocity provinces on the core-mantle boundary, *Earth and Planetary Science Letters*, *265*(1-2), 49-60, doi:10.1016/j.epsl.2007.09.042.

Cabral, R. A., M. G. Jackson, E. F. Rose-Koga, K. T. Koga, M. J. Whitehouse, M. A. Antonelli, J. Farquhar, J. M. Day, and E. H. Hauri (2013), Anomalous sulphur isotopes in plume lavas reveal deep mantle storage of Archaean crust, *Nature*, *496*(7446), 490-493, doi:10.1038/nature12020.

Campbell, I. H., and H. O'Neill (2012), Evidence against a chondritic Earth, *Nature*, *483*(7391), 553-558, doi:10.1038/nature10901.

Canup, R. M., and E. Asphaug (2001), Origin of the Moon in a giant impact near the end of the Earth's formation, *Nature*, *412*(6848), 708-712, doi:10.1038/35089010.

Chopelas, A., and R. Boehler (1992), Thermal expansivity in the lower mantle, *Geophysical Research Letters*, *19*(19), 1983-1986, doi:10.1029/92gl02144.

Christensen, U. R., and A. W. Hofmann (1994), Segregation of subducted oceanic crust in the convecting mantle, *Journal of Geophysical Research*, *99*(B10), 19867-19884, doi:10.1029/93JB03403.

Coltice, N., and J. Schmalzl (2006), Mixing times in the mantle of the early Earth derived from 2-D and 3-D numerical simulations of convection, *Geophysical Research Letters*, *33*(23), doi:10.1029/2006gl027707.

Cottaar, S., M. Li, A. K. McNamara, B. Romanowicz, and H.-R. Wenk (2014), Synthetic seismic anisotropy models within a slab impinging on the core – mantle boundary, *Geophysical Journal International*, *199*(1), 164-177, doi:10.1093/gji/ggu244.

Cottaar, S., and B. Romanowicz (2012), An unusually large ULVZ at the base of the mantle near Hawaii, *Earth and Planetary Science Letters*, *355-356*(0), 213-222, doi:10.1016/j.epsl.2012.09.005.

Davaille, A. (1999), Simultaneous generation of hotspots and superswells by convection in a heterogenous planetary mantle, *Nature*, *402*(6763), 756-760, doi:10.1038/45461.

Davaille, A., F. Girard, and M. Le Bars (2002), How to anchor hotspots in a convecting mantle?, *Earth and Planetary Science Letters*, *203*(2), 621-634, doi:10.1016/S0012-821X(02)00897-X.

Davaille, A., E. Stutzmann, G. Silveira, J. Besse, and V. Courtillot (2005), Convective patterns under the Indo-Atlantic <box> ?, *Earth and Planetary Science Letters*, *239*(3-4), 233-252, doi:10.1016/j.epsl.2005.07.024.

Davies, G. F. (2008), Episodic layering of the early mantle by the 'basalt barrier' mechanism, *Earth and Planetary Science Letters*, *275*(3-4), 382-392, doi:10.1016/j.epsl.2008.08.036.

Deschamps, F., L. Cobden, and P. J. Tackley (2012), The primitive nature of large low shear-wave velocity provinces, *Earth and Planetary Science Letters*, *349*(0), 198-208, doi:10.1016/j.epsl.2012.07.012.

Deschamps, F., E. Kaminski, and P. J. Tackley (2011), A deep mantle origin for the primitive signature of ocean island basalt, *Nature Geosci.*, *4*(12), 879-882, doi:10.1038/Ngeo1295.

Deschamps, F., and P. J. Tackley (2008), Searching for models of thermo-chemical convection that explain probabilistic tomography: I. Principles and influence of rheological parameters, *Physics of The Earth and Planetary Interiors*, *171*(1-4), 357-373, doi:10.1016/j.pepi.2008.04.016.

Dobson, D. P., and J. P. Brodholt (2005), Subducted banded iron formations as a source of ultralow-velocity zones at the core-mantle boundary, *Nature*, *434*(7031), 371-374, doi:10.1038/Nature03385.

Dziewonski, A. M., and D. L. Anderson (1981), Preliminary reference Earth model, *Physics of The Earth and Planetary Interiors*, *25*(4), 297-356, doi:10.1016/0031-9201(81)90046-7.

Dziewonski, A. M., V. Lekic, and B. A. Romanowicz (2010), Mantle Anchor Structure: An argument for bottom up tectonics, *Earth and Planetary Science Letters*, *299*(1-2), 69-79, doi:10.1016/j.epsl.2010.08.013.

Farnetani, C. G. (1997), Excess temperature of mantle plumes: The role of chemical stratification across D", *Geophysical Research Letters*, *24*(13), 1583-1586, doi:10.1029/97gl01548.

Farnetani, C. G., B. Legras, and P. J. Tackley (2002), Mixing and deformations in mantle plumes, *Earth and Planetary Science Letters*, *196*(1-2), 1-15, doi:10.1016/S0012-821x(01)00597-0.

Fei, Y., L. Zhang, A. Corgne, H. Watson, A. Ricolleau, Y. Meng, and V. Prakapenka (2007), Spin transition and equations of state of (Mg, Fe)O solid solutions, *Geophysical Research Letters*, *34*(17), doi:10.1029/2007gl030712.

Ferrachat, S., and Y. Ricard (1998), Regular vs, chaotic mantle mixing, *Earth and Planetary Science Letters*, *155*(1-2), 75-86, doi:10.1016/S0012-821X(97)00200-8.

Fitoussi, C., and B. Bourdon (2012), Silicon Isotope Evidence Against an Enstatite Chondrite Earth, *Science*, *335*(6075), 1477-1480, doi:10.1126/science.1219509.

Ford, S. R., E. J. Garnero, and A. K. McNamara (2006), A strong lateral shear velocity gradient and anisotropy heterogeneity in the lowermost mantle beneath the southern Pacific, *Journal of Geophysical Research*, *111*(B3), B03306, doi:10.1029/2004jb003574.

Fujita, K., and M. Ogawa (2009), Basaltic accumulation instability and chaotic plate motion in the earliest mantle inferred from numerical experiments, *Journal of Geophysical Research-Solid Earth*, *114*, B10402, doi:10.1029/2008jb006222.

Garnero, E. J., and D. V. Helmberger (1996), Seismic detection of a thin laterally varying boundary layer at the base of the mantle beneath the central-Pacific, *Geophysical Research Letters*, *23*(9), 977-980, doi:10.1029/95gl03603.

Garnero, E. J., and A. K. McNamara (2008), Structure and Dynamics of Earth's Lower Mantle, *Science*, *320*(5876), 626-628, doi:10.1126/science.1148028.

Graham, D. W. (2002), Noble Gas Isotope Geochemistry of Mid-Ocean Ridge and Ocean Island Basalts: Characterization of Mantle Source Reservoirs, *Reviews in Mineralogy and Geochemistry*, *47*(1), 247-317, doi:10.2138/rmg.2002.47.8.

Grand, S. P. (2002), Mantle shear-wave tomography and the fate of subducted slabs, *Philosophical Transactions of the Royal Society of London Series a-Mathematical Physical and Engineering Sciences*, *360*(1800), 2475-2491, doi:10.1098/rsta.2002.1077.

Grand, S. P., R. D. van der Hilst, and S. Widiyantoro (1997), Global seismic tomography: a snapshot of convection in the Earth, *GSA Today*, *7*, 1-7, Retrieved from http://geo.web.ru/sbmg/sbor/tomography/Grand/grand.html

Hahm, D., P. R. Castillo, and D. R. Hilton (2009), A deep mantle source for high ^{3}He/^{4}He ocean island basalts (OIB) inferred from Pacific near-ridge seamount lavas, *Geophysical Research Letters*, *36*(20), L20316, doi:10.1029/2009gl040560.

Hart, S. R., and A. Zindler (1986), In search of a bulk-Earth composition, *Chemical Geology*, *57*(3–4), 247-267, doi:10.1016/0009-2541(86)90053-7.

Hayden, L. A., and E. B. Watson (2007), A diffusion mechanism for core-mantle interaction, *Nature*, *450*(7170), 709-U706, doi:10.1038/Nature06380.

He, X., and M. D. Long (2011), Lowermost mantle anisotropy beneath the northwestern Pacific: Evidence from PcS, ScS, SKS, and SKKS phases, *Geochemistry Geophysics Geosystems*, *12*, Q12012, doi:10.1029/2011gc003779.

He, Y., and L. Wen (2009), Structural features and shear-velocity structure of the "Pacific Anomaly", *Journal of Geophysical Research*, *114*(B2), B02309, doi:10.1029/2008jb005814.

He, Y., and L. Wen (2011), Seismic velocity structures and detailed features of the D" discontinuity near the core-mantle boundary beneath eastern Eurasia, *Physics of The Earth and Planetary Interiors*(3-4), 176-184, doi:10.1016/j.pepi.2011.09.002.

He, Y., and L. Wen (2012), Geographic boundary of the "Pacific Anomaly" and its geometry and transitional structure in the north, *Journal of Geophysical Research*, *117*(B9), B09308, doi:10.1029/2012jb009436.

Helmberger, D., S. Ni, L. Wen, and J. Ritsema (2000), Seismic evidence for ultralow-velocity zones beneath Africa and eastern Atlantic, *Journal of Geophysical Research*, *105*(B10), 23865-23878, doi:10.1029/2000jb900143.

Helmberger, D. V., L. Wen, and X. Ding (1998), Seismic evidence that the source of the Iceland hotspot lies at the core-mantle boundary, *Nature*, *396*(6708), 251-255, doi:10.1038/24357.

Hernlund, J. W., and C. Houser (2008), The statistical distribution of seismic velocities in Earth's deep mantle, *Earth and Planetary Science Letters*, *265*(3-4), 423-437, doi:10.1016/j.epsl.2007.10.042.

Hernlund, J. W., and A. M. Jellinek (2010), Dynamics and structure of a stirred partially molten ultralow-velocity zone, *Earth and Planetary Science Letters*, *296*(1-2), 1-8, doi:10.1016/j.epsl.2010.04.027.

Hernlund, J. W., and P. J. Tackley (2007), Some dynamical consequences of partial melting in Earth's deep mantle, *Physics of The Earth and Planetary Interiors*, *162*(1-2), 149-163, doi:10.1016/j.pepi.2007.04.005.

Hernlund, J. W., C. Thomas, and P. J. Tackley (2005), A doubling of the post-perovskite phase boundary and structure of the Earth's lowermost mantle, *Nature*, *434*(7035), 882-886, doi:10.1038/nature03472.

Hier-Majumder, S. (2008), Influence of contiguity on seismic velocities of partially molten aggregates, *Journal of Geophysical Research-Solid Earth*, *113*(B12), doi:10.1029/2008jb005662.

Hier-Majumder, S., and J. Revenaugh (2010), Relationship between the viscosity and topography of the ultralow-velocity zone near the core-mantle boundary, *Earth and Planetary Science Letters*, *299*(3-4), 382-386, doi:10.1016/j.epsl.2010.09.018.

Hirose, K., N. Takafuji, N. Sata, and Y. Ohishi (2005), Phase transition and density of subducted MORB crust in the lower mantle, *Earth and Planetary Science Letters*, *237*(1-2), 239-251, doi:10.1016/j.epsl.2005.06.035.

Hofmann, A. W. (1997), Mantle geochemistry: The message from oceanic volcanism, *Nature*, *385*(6613), 219-229, doi:10.1038/385219a0.

Hofmann, A. W., D. H. Heinrich, and K. T. Karl (2007), Sampling Mantle Heterogeneity through Oceanic Basalts: Isotopes and Trace Elements, in *Treatise on Geochemistry*, edited, pp. 1-44, Pergamon, Oxford.

Hofmann, A. W., and W. M. White (1982), Mantle Plumes from Ancient Oceanic-Crust, *Earth and Planetary Science Letters*, *57*(2), 421-436, doi:10.1016/0012-821x(82)90161-3.

Huang, J., and G. F. Davies (2007), Stirring in three-dimensional mantle convection models and implications for geochemistry: 2. Heavy tracers, *Geochemistry Geophysics Geosystems*, *8*(7), Q07004, doi:10.1029/2007gc001621.

Hunt, S. A., D. J. Weidner, L. Li, L. P. Wang, N. P. Walte, J. P. Brodholt, and D. P. Dobson (2009), Weakening of calcium iridate during its transformation from perovskite to post-perovskite, *Nature Geosci.*, *2*(11), 794-797, doi:10.1038/Ngeo663.

Hutko, A. R., T. Lay, and J. Revenaugh (2009), Localized double-array stacking analysis of PcP: D" and ULVZ structure beneath the Cocos plate, Mexico, central Pacific, and north Pacific, *Physics of The Earth and Planetary Interiors*, *173*(1-2), 60-74, doi:10.1016/j.pepi.2008.11.003.

Irifune, T. (1987), An experimental investigation of the pyroxene-garnet transformation in a pyrolite composition and its bearing on the constitution of the mantle, *Physics of The Earth and Planetary Interiors*, *45*(4), 324-336, doi:10.1016/0031-9201(87)90040-9.

Irifune, T., T. Shinmei, C. A. McCammon, N. Miyajima, D. C. Rubie, and D. J. Frost (2010), Iron Partitioning and Density Changes of Pyrolite in Earth's Lower Mantle, *Science*, *327*(5962), 193-195, doi:10.1126/science.1181443.

Ishii, M., and J. Tromp (1999), Normal-mode and free-Air gravity constraints on lateral variations in velocity and density of Earth's mantle, *Science*, *285*(5431), 1231-1236, doi:10.1126/science.285.5431.1231.

Ishii, M., and J. Tromp (2004), Constraining large-scale mantle heterogeneity using mantle and inner-core sensitive normal modes, *Physics of The Earth and Planetary Interiors*, *146*(1-2), 113-124, doi:10.1016/j.pepi.2003.06.012.

Jackson, C. R. M., L. B. Ziegler, H. Zhang, M. G. Jackson, and D. R. Stegman (2014), A geochemical evaluation of potential magma ocean dynamics using a parameterized model for perovskite crystallization, *Earth and Planetary Science Letters*, *392*(0), 154-165, doi:10.1016/j.epsl.2014.01.028.

Jackson, M. G., R. W. Carlson, M. D. Kurz, P. D. Kempton, D. Francis, and J. Blusztajn (2010), Evidence for the survival of the oldest terrestrial mantle reservoir, *Nature*, *466*(7308), 853-U884, doi:10.1038/Nature09287.

Jellinek, A. M., and M. Manga (2004), Links between long-lived hot spots, mantle plumes, D ", and plate tectonics, *Reviews of Geophysics*, *42*(3), doi:10.1029/2003rg000144.

Kanda, R. V. S., and D. J. Stevenson (2006), Suction mechanism for iron entrainment into the lower mantle, *Geophysical Research Letters*, *33*(2), doi:10.1029/2005gl025009.

Kellogg, L. H., B. H. Hager, and R. D. van der Hilst (1999), Compositional Stratification in the Deep Mantle, *Science*, *283*(5409), 1881-1884, doi:10.1126/science.283.5409.1881.

Kito, T., S. Rost, C. Thomas, and E. J. Garnero (2007), New insights into the P- and S-wave velocity structure of the D " discontinuity beneath the Cocos plate, *Geophysical Journal International*, *169*(2), 631-645, doi:10.1111/j.1365-246X.2007.03350.x.

Knittle, E., and R. Jeanloz (1989), Simulating the core-mantle boundary: An experimental study of high-pressure reactions between silicates and liquid iron, *Geophysical Research Letters*, *16*(7), 609-612, doi:10.1029/GL016i007p00609.

Knittle, E., and R. Jeanloz (1991), Earth's Core-Mantle Boundary: Results of Experiments at High Pressures and Temperatures, *Science*, *251*(5000), 1438-1443, doi:10.1126/science.251.5000.1438.

Labrosse, S., J. W. Hernlund, and N. Coltice (2007), A crystallizing dense magma ocean at the base of the Earth's mantle, *Nature*, *450*(7171), 866-869, doi:10.1038/Nature06355.

Lay, T. (2008), Sharpness of the D " discontinuity beneath the Cocos Plate: Implications for the perovskite to post-perovskite phase transition, *Geophysical Research Letters*, *35*(3), doi:10.1029/2007GL032465.

Lay, T., J. Hernlund, and B. A. Buffett (2008), Core-mantle boundary heat flow, *Nature Geosci*, *1*(1), 25-32, doi:10.1038/Ngeo.2007.44.

Lay, T., J. Hernlund, E. J. Garnero, and M. S. Thorne (2006), A Post-Perovskite Lens and D" Heat Flux Beneath the Central Pacific, *Science*, *314*(5803), 1272-1276, doi:10.1126/science.1133280.

Lee, C. T. A., P. Luffi, T. Hoink, J. Li, R. Dasgupta, and J. Hernlund (2010), Upside-down differentiation and generation of a 'primordial' lower mantle, *Nature*, *463*(7283), 930-U102, doi:10.1038/Nature08824.

Li, C., R. D. van der Hilst, E. R. Engdahl, and S. Burdick (2008), A new global model for P wave speed variations in Earth's mantle, *Geochemistry Geophysics Geosystems*, *9*(5), Q05018, doi:10.1029/2007gc001806.

Li, M., and A. K. McNamara (2013), The difficulty for subducted oceanic crust to accumulate at the Earth's core-mantle boundary, *Journal of Geophysical Research*, *118*(4), 1807-1816, doi:10.1002/Jgrb.50156.

Li, M., A. K. McNamara, and E. J. Garnero (2014a), Chemical complexity of hotspots caused by cycling oceanic crust through mantle reservoirs, *Nature Geoscience*, *7*(5), 366-370, doi:10.1038/Ngeo2120.

Li, X. D., and B. Romanowicz (1996), Global mantle shear velocity model developed using nonlinear asymptotic coupling theory, *Journal of Geophysical Research-Solid Earth*, *101*(B10), 22245-22272, doi:10.1029/96JB01306.

Li, Y., F. Deschamps, and P. J. Tackley (2014b), Effects of low-viscosity post-perovskite on the stability and structure of primordial reservoirs in the lower mantle, *Geophysical Research Letters*, 2014GL061362, doi:10.1002/2014GL061362.

Lin, J.-F., S. Speziale, Z. Mao, and H. Marquardt (2013), EFFECTS OF THE ELECTRONIC SPIN TRANSITIONS OF IRON IN LOWER MANTLE MINERALS: IMPLICATIONS FOR DEEP MANTLE GEOPHYSICS AND GEOCHEMISTRY, *Reviews of Geophysics*, *51*(2), 244-275, doi:10.1002/rog.20010.

Lin, J.-F., G. Vanko, S. D. Jacobsen, V. Iota, V. V. Struzhkin, V. B. Prakapenka, A. Kuznetsov, and C.-S. Yoo (2007), Spin Transition Zone in Earth's Lower Mantle, *Science*, *317*(5845), 1740-1743, doi:10.1126/science.1144997.

Lin, J. F., V. V. Struzhkin, S. D. Jacobsen, M. Y. Hu, P. Chow, J. Kung, H. Liu, H. K. Mao, and R. J. Hemley (2005), Spin transition of iron in magnesiowustite in the Earth's lower mantle, *Nature*, *436*(7049), 377-380, doi:10.1038/nature03825.

LithgowBertelloni, C., and M. Gurnis (1997), Cenozoic subsidence and uplift of continents from time-varying dynamic topography, *Geology*, *25*(8), 735-738, doi:10.1130/0091-7613(1997).

Luo, S.-N., S. Ni, and D. V. Helmberger (2001), Evidence for a sharp lateral variation of velocity at the core-mantle boundary from multipathed PKPab, *Earth and Planetary Science Letters*, *189*(3-4), 155-164, doi:10.1016/S0012-821x(01)00364-8.

Lynner, C., and M. D. Long (2014), Lowermost mantle anisotropy and deformation along the boundary of the African LLSVP, *Geophysical Research Letters*, *41*(10), 3447-3454, doi:10.1002/2014gl059875.

Mao, W. L., H.-k. Mao, W. Sturhahn, J. Zhao, V. B. Prakapenka, Y. Meng, J. Shu, Y. Fei, and R. J. Hemley (2006), Iron-Rich Post-Perovskite and the Origin of Ultralow-Velocity Zones, *Science*, *312*(5773), 564-565, doi:10.1126/science.1123442.

Mao, W. L., et al. (2005), Iron-rich silicates in the Earth's D " layer, *Proceedings of the National Academy of Sciences of the United States of America*, *102*(28), 9751-9753, doi:10.1073/pnas.0503737102.

Masters, G., G. Laske, H. Bolton, and A. Dziewonski (2000), The relative behavior of shear veocity, bulk sound speed, and compressional velocity in the mantle: implications for chemical and thermal structure, in *Earth's Deep Interior: Mineral Physics and Tomography From the Atomic to the Global Scale*, edited by S. K. e. al., pp. 63-86, AGU Geophysical Monograph, Washington, D.C.

McDonough, W. F., and S. s. Sun (1995), The composition of the Earth, *Chemical Geology*, *120*(3‐4), 223-253, doi:10.1016/0009-2541(94)00140-4.

McKenzie, D., and M. J. Bickle (1988), The Volume and Composition of Melt Generated by Extension of the Lithosphere, *Journal of Petrology*, *29*(3), 625-679, doi:10.1093/petrology/29.3.625.

McNamara, A. K., E. J. Garnero, and S. Rost (2010), Tracking deep mantle reservoirs with ultra-low velocity zones, *Earth and Planetary Science Letters*, *299*(1-2), 1-9, doi:10.1016/j.epsl.2010.07.042.

McNamara, A. K., and S. Zhong (2004), Thermochemical structures within a spherical mantle: Superplumes or piles?, *Journal of Geophysical Research*, *109*(B7), B07402, doi:10.1029/2003jb002847.

McNamara, A. K., and S. Zhong (2005), Thermochemical structures beneath Africa and the Pacific Ocean, *Nature*, *437*(7062), 1136-1139, doi:10.1038/nature04066.

Merkel, S., A. K. McNamara, A. Kubo, S. Speziale, L. Miyagi, Y. Meng, T. S. Duffy, and H.-R. Wenk (2007), Deformation of (Mg,Fe)SiO3 Post-Perovskite and D" Anisotropy, *Science*, *316*(5832), 1729-1732, doi:10.1126/science.1140609.

Miller, M. S., and F. Niu (2008), Bulldozing the core-mantle boundary: Localized seismic scatterers beneath the Caribbean Sea, *Physics of The Earth and Planetary Interiors*, *170*(1-2), 89-94, doi:10.1016/j.pepi.2008.07.044.

Moresi, L., and M. Gurnis (1996), Constraints on the lateral strength of slabs from three-dimensional dynamic flow models, *Earth and Planetary Science Letters*, *138*(1-4), 15-28, doi:10.1016/0012-821x(95)00221-W.

Moresi, L. N., and V. S. Solomatov (1995), Numerical Investigation of 2d Convection with Extremely Large Viscosity Variations, *Physics of Fluids*, *7*(9), 2154-2162, doi:10.1063/1.868465.

Mukhopadhyay, S. (2012), Early differentiation and volatile accretion recorded in deep-mantle neon and xenon, *Nature*, *486*(7401), 101-U124, doi:10.1038/Nature11141.

Murakami, M., and J. Bass (2011), Evidence of denser MgSiO3 glass above 133 gigapascal (GPa) and implications for remnants of ultradense silicate melt from a deep magma ocean, *Proceedings of the National Academy of Sciences of the United States of America*, *108*(42), 17286-17295, doi:10.1073/pnas.1109748108.

Murakami, M., K. Hirose, K. Kawamura, N. Sata, and Y. Ohishi (2004), Post-Perovskite Phase Transition in MgSiO3, *Science*, *304*(5672), 855-858, doi:10.1126/science.1095932.

Nakagawa, T., and P. J. Tackley (2004), Effects of thermo-chemical mantle convection on the thermal evolution of the Earth's core, *Earth and Planetary Science Letters*, *220*(1-2), 107-119, doi:10.1016/S0012-821x(04)00055-X.

Nakagawa, T., and P. J. Tackley (2011), Effects of low-viscosity post-perovskite on thermo-chemical mantle convection in a 3-D spherical shell, *Geophysical Research Letters*, *38*(4), L04309, doi:10.1029/2010gl046494.

Nakagawa, T., and P. J. Tackley (2014), Influence of combined primordial layering and recycled MORB on the coupled thermal evolution of Earth's mantle and core, *Geochemistry, Geophysics, Geosystems*, *15*(3), 619-633, doi:10.1002/2013GC005128.

Nakagawa, T., P. J. Tackley, F. Deschamps, and J. A. D. Connolly (2009), Incorporating self-consistently calculated mineral physics into thermochemical mantle convection simulations in a 3-D spherical shell and its influence on seismic anomalies in Earth's mantle, *Geochemistry Geophysics Geosystems*, *10*(3), Q03004, doi:10.1029/2008gc002280.

Nakagawa, T., P. J. Tackley, F. Deschamps, and J. A. D. Connolly (2010), The influence of MORB and harzburgite composition on thermo-chemical mantle convection in a 3-D spherical shell with self-consistently calculated mineral physics, *Earth and Planetary Science Letters*, *296*(3-4), 403-412, doi:10.1016/j.epsl.2010.05.026.

Ni, S., and D. V. Helmberger (2003), Ridge-like lower mantle structure beneath South Africa, *Journal of Geophysical Research*, *108*(B2), 2094, doi:10.1029/2001jb001545.

Ni, S., E. Tan, M. Gurnis, and D. Helmberger (2002), Sharp Sides to the African Superplume, *Science*, *296*(5574), 1850-1852, doi:10.1126/science.1070698.

Niu, F., and L. Wen (2001), Strong seismic scatterers near the core-mantle boundary west of Mexico, *Geophysical Research Letters*, *28*(18), 3557-3560, doi:10.1029/2001gl013270.

Nomura, R., K. Hirose, K. Uesugi, Y. Ohishi, A. Tsuchiyama, A. Miyake, and Y. Ueno (2014), Low Core-Mantle Boundary Temperature Inferred from the Solidus of Pyrolite, *Science*, *343*(6170), 522-525, doi:10.1126/science.1248186.

Nomura, R., H. Ozawa, S. Tateno, K. Hirose, J. Hernlund, S. Muto, H. Ishii, and N. Hiraoka (2011), Spin crossover and iron-rich silicate melt in the Earth's deep mantle, *Nature*, *473*(7346), 199-202, doi:10.1038/Nature09940.

Nowacki, A., J. Wookey, and J. M. Kendall (2010), Deformation of the lowermost mantle from seismic anisotropy, *Nature*, *467*(7319), 1091-1094, doi:10.1038/nature09507.

O'Farrell, K. A., and J. P. Lowman (2010), Emulating the thermal structure of spherical shell convection in plane-layer geometry mantle convection models, *Physics of The Earth and Planetary Interiors*, *182*(1-2), 73-84, doi:10.1016/j.pepi.2010.06.010.

O'Neill, H. S. C. (1991), The origin of the moon and the early history of the earth—A chemical model. Part 2: The earth, *Geochimica et Cosmochimica Acta*, *55*(4), 1159-1172, doi:10.1016/0016-7037(91)90169-6.

Oganov, A. R., and S. Ono (2004), Theoretical and experimental evidence for a post-perovskite phase of MgSiO3 in Earth's D" layer, *Nature*, *430*(6998), 445-448, doi:10.1038/Nature02701.

Ogawa, M. (2010), Variety of plumes and the fate of subducted basaltic crusts, *Physics of The Earth and Planetary Interiors*, *183*(1-2), 366-375, doi:10.1016/j.pepi.2010.05.001.

Ohta, K., K. Hirose, T. Lay, N. Sata, and Y. Ohishi (2008), Phase transitions in pyrolite and MORB at lowermost mantle conditions: Implications for a MORB-rich pile above the core-mantle boundary, *Earth and Planetary Science Letters*, *267*(1-2), 107-117, doi:10.1016/j.epsl.2007.11.037.

Ohtani, E., and M. Maeda (2001), Density of basaltic melt at high pressure and stability of the melt at the base of the lower mantle, *Earth and Planetary Science Letters*, *193*(1), 69-144, doi:10.1016/S0012-821x(01)00505-2.

Otsuka, K., and S. Karato (2012), Deep penetration of molten iron into the mantle caused by a morphological instability, *Nature*, *492*(7428), 243-246, doi:10.1038/nature11663.

Revenaugh, J., and R. Meyer (1997), Seismic Evidence of Partial Melt Within a Possibly Ubiquitous Low-Velocity Layer at the Base of the Mantle, *Science*, *277*(5326), 670-673, doi:10.1126/science.277.5326.670.

Ricolleau, A., et al. (2009), Density profile of pyrolite under the lower mantle conditions, *Geophysical Research Letters*, *36*(6), L06302, doi:10.1029/2008gl036759.

Ricolleau, A., J.-P. Perrillat, G. Fiquet, I. Daniel, J. Matas, A. Addad, N. Menguy, H. Cardon, M. Mezouar, and N. Guignot (2010), Phase relations and equation of state of a natural MORB: Implications for the density profile of subducted oceanic crust in the Earth's lower mantle, *Journal of Geophysical Research*, *115*(B8), B08202, doi:10.1029/2009jb006709.

Ringwood, A. E. (1962), A model for the upper mantle, *Journal of Geophysical Research*, *67*(2), 857-867, doi:10.1029/JZ067i002p00857.

Ringwood, A. E. (1982), Phase-Transformations and Differentiation in Subducted Lithosphere - Implications for Mantle Dynamics, Basalt Petrogenesis, and Crustal Evolution, *Journal of Geology*, *90*(6), 611-643, doi:10.1086/628721.

Ringwood, A. E. (1990), Slab-Mantle Interactions .3. Petrogenesis of Intraplate Magmas and Structure of the Upper Mantle, *Chemical Geology*, *82*(3-4), 187-207, doi:10.1016/0009-2541(90)90081-H.

Ringwood, A. E. (1991), Phase-Transformations and Their Bearing on the Constitution and Dynamics of the Mantle, *Geochimica et Cosmochimica Acta*, *55*(8), 2083-2110, doi:10.1016/0016-7037(91)90090-R.

Ritsema, J., A. Deuss, H. J. van Heijst, and J. H. Woodhouse (2011), S40RTS: a degree-40 shear-velocity model for the mantle from new Rayleigh wave dispersion, teleseismic traveltime and normal-mode splitting function measurements, *Geophysical Journal International*, *184*(3), 1223-1236, doi:10.1111/j.1365-246X.2010.04884.x.

Ritsema, J., H. J. van Heijst, and J. H. Woodhouse (2004), Global transition zone tomography, *Journal of Geophysical Research*, *109*(B2), B02302, doi:10.1029/2003jb002610.

Romanowicz, B. (2003), Global mantle tomography: Progress status in the past 10 years, *Annual Review of Earth and Planetary Sciences*, *31*, 303-328, doi:10.1146/annurev.earth.31.091602.113555.

Rondenay, S., and K. M. Fischer (2003), Constraints on localized core-mantle boundary structure from multichannel, broadband SKS coda analysis, *Journal of Geophysical Research*, *108*(B11), 2537, doi:10.1029/2003jb002518.

Ross, A. R., H. Thybo, and L. N. Solidilov (2004), Reflection seismic profiles of the core-mantle boundary, *Journal of Geophysical Research*, *109*(B8), B08303, doi:10.1029/2003jb002515.

Rost, S., and P. S. Earle (2010), Identifying regions of strong scattering at the core-mantle boundary from analysis of PKKP precursor energy, *Earth and Planetary Science Letters*, *297*(3-4), 616-626, doi:10.1016/j.epsl.2010.07.014.

Rost, S., E. J. Garnero, and Q. Williams (2006), Fine-scale ultralow-velocity zone structure from high-frequency seismic array data, *Journal of Geophysical Research*, *111*(B9), B09310, doi:10.1029/2005jb004088.

Rost, S., E. J. Garnero, Q. Williams, and M. Manga (2005), Seismological constraints on a possible plume root at the core-mantle boundary, *Nature*, *435*(7042), 666-669, doi:10.1038/Nature03620.

Rost, S., and J. Revenaugh (2003), Small-scale ultralow-velocity zone structure imaged by ScP, *Journal of Geophysical Research*, *108*(B1), 2056, doi:10.1029/2001jb001627.

Samuel, H., and C. G. Farnetani (2003), Thermochemical convection and helium concentrations in mantle plumes, *Earth and Planetary Science Letters*, *207*(1-4), 39-56, doi:10.1016/S0012-821x(02)01125-1.

Schubert, G., G. Masters, P. Olson, and P. Tackley (2004), Superplumes or plume clusters?, *Physics of The Earth and Planetary Interiors*, *146*(1-2), 147-162, doi:10.1016/j.pepi.2003.09.025.

Shang, X., S.-H. Shim, M. de Hoop, and R. van der Hilst (2014), Multiple seismic reflectors in Earth's lowermost mantle, *Proceedings of the National Academy of Sciences*, *111*(7), 2442-2446, doi:10.1073/pnas.1312647111.

Shim, S.-H. (2008), The Postperovskite Transition, *Annual Review of Earth and Planetary Sciences*, *36*(1), 569-599, doi:10.1146/annurev.earth.36.031207.124309.

Sobolev, A. V., A. W. Hofmann, K. P. Jochum, D. V. Kuzmin, and B. Stoll (2011), A young source for the Hawaiian plume, *Nature*, *476*(7361), 434-437, doi:10.1038/nature10321.

Solomatov, V. S. (2000), Fluid dynamics of a terrestrial magma ocean, *In Origin of the Earth and Moon (ed. R. Canup and K. Righter)*, 323-338.

Solomatov, V. S. (2007), Magma oceans and primordial mantle differentiation, *Treatise on Geophysics*, 91-119.

Steinbach, V., and D. A. Yuen (1999), Viscous heating: a potential mechanism for the formation of the ultralow velocity zone, *Earth and Planetary Science Letters*, *172*(3–4), 213-220, doi:10.1016/S0012-821X(99)00205-8.

Stixrude, L., and C. Lithgow-Bertelloni (2011), Thermodynamics of mantle minerals – II. Phase equilibria, *Geophysical Journal International*, *184*(3), 1180-1213, doi:10.1111/j.1365-246X.2010.04890.x.

Stixrude, L., and C. Lithgow-Bertelloni (2012), Geophysics of Chemical Heterogeneity in the Mantle, *Annual Review of Earth and Planetary Sciences*, *40*(1), 569-595, doi:10.1146/annurev.earth.36.031207.124244.

Su, W. J., and A. M. Dziewonski (1997), Simultaneous inversion for 3-D variations in shear and bulk velocity in the mantle, *Physics of The Earth and Planetary Interiors*, *100*(1-4), 135-156, doi:10.1016/S0031-9201(96)03236-0.

Su, W. J., R. L. Woodward, and A. M. Dziewonski (1994), Degree-12 Model of Shear Velocity Heterogeneity in the Mantle, *Journal of Geophysical Research-Solid Earth*, *99*(B4), 6945-6980, doi:10.1029/93JB03408.

Sun, D., D. V. Helmberger, J. M. Jackson, R. W. Clayton, and D. J. Bower (2013), Rolling hills on the core‒mantle boundary, *Earth and Planetary Science Letters*, *361*(0), 333-342, doi:10.1016/j.epsl.2012.10.027.

Sun, D., E. Tan, D. Helmberger, and M. Gurnis (2007a), Seismological support for the metastable superplume model, sharp features, and phase changes within the lower mantle, *Proceedings of the National Academy of Sciences of the United States of America*, *104*(22), 9151-9155, doi:10.1073/pnas.0608160104.

Sun, S.-S. (1982), Chemical composition and origin of the earth's primitive mantle, *Geochimica et Cosmochimica Acta*, *46*(2), 179-192, doi:10.1016/0016-7037(82)90245-9.

Sun, X., X. Song, S. Zheng, and D. V. Helmberger (2007b), Evidence for a chemical-thermal structure at base of mantle from sharp lateral P-wave variations beneath Central America, *Proc Natl Acad Sci U S A*, *104*(1), 26-30, doi:10.1073/pnas.0609143103.

Tackley, P. (1998), Three-Dimensional Simulations of Mantle Convection with a Thermo-Chemical Basal Boundary Layer: D"?, *AGU Geophysical Mongraph on the CMB ed. M. Gurnis*.

Tackley, P. J. (2000), Mantle Convection and Plate Tectonics: Toward an Integrated Physical and Chemical Theory, *Science*, *288*(5473), 2002-2007, doi:10.1126/science.288.5473.2002.

Tackley, P. J. (2007), Mantle Geochemical Geodynamics, in *Treatise on Geophysics*, edited by D. Bercovici, pp. 437‒505, Elsevier.

Tackley, P. J. (2011), Living dead slabs in 3-D: The dynamics of compositionally-stratified slabs entering a "slab graveyard" above the core-mantle boundary, *Physics of The Earth and Planetary Interiors*, *188*(3-4), 150-162, doi:10.1016/j.pepi.2011.04.013.
166

Tackley, P. J. (2012), Dynamics and evolution of the deep mantle resulting from thermal, chemical, phase and melting effects, *Earth Sci. Rev.*, *110*(1-4), 1-25, doi:10.1016/j.earscirev.2011.10.001.

Tackley, P. J., and S. D. King (2003), Testing the tracer ratio method for modeling active compositional fields in mantle convection simulations, *Geochemistry Geophysics Geosystems*, *4*(4), 8302, doi:10.1029/2001gc000214.

Tackley, P. J., and S. X. Xie (2002), The thermochemical structure and evolution of Earth's mantle: constraints and numerical models, *Philosophical Transactions of the Royal Society of London Series a-Mathematical Physical and Engineering Sciences*, *360*(1800), 2593-2609, doi:10.1098/rsta.2002.1082.

Takafuji, N., K. Hirose, M. Mitome, and Y. Bando (2005), Solubilities of O and Si in liquid iron in equilibrium with (Mg,Fe)SiO3 perovskite and the light elements in the core, *Geophysical Research Letters*, *32*(6), L06313, doi:10.1029/2005gl022773.

Tan, E., and M. Gurnis (2005), Metastable superplumes and mantle compressibility, *Geophysical Research Letters*, *32*(20), L20307, doi:10.1029/2005GL024190.

Tan, E., and M. Gurnis (2007), Compressible thermochemical convection and application to lower mantle structures, *Journal of Geophysical Research*, *112*(B6), B06304, doi:10.1029/2006JB004505.

Taylor, S. R. (1964), Chondritic Earth Model, *Nature*, *202*(4929), 281-282, doi:10.1038/202281a0.

To, A., Y. Fukao, and S. Tsuboi (2011), Evidence for a thick and localized ultra low shear velocity zone at the base of the mantle beneath the central Pacific, *Physics of The Earth and Planetary Interiors*, *184*(3-4), 119-133, doi:10.1016/j.pepi.2010.10.015.

To, A., B. Romanowicz, Y. Capdeville, and N. Takeuchi (2005), 3D effects of sharp boundaries at the borders of the African and Pacific Superplumes: Observation and modeling, *Earth and Planetary Science Letters*, *233*(1-2), 137-153, doi:10.1016/j.epsl.2005.01.037.

Tonks, W. B., and H. J. Melosh (1993), Magma ocean formation due to giant impacts, *Journal of Geophysical Research: Planets*, *98*(E3), 5319-5333, doi:10.1029/92JE02726.

Torsvik, T. H., K. Burke, B. Steinberger, S. J. Webb, and L. D. Ashwal (2010), Diamonds sampled by plumes from the core-mantle boundary, *Nature*, *466*(7304), 352-355, doi:10.1038/nature09216.

Torsvik, T. H., R. van der Voo, P. V. Doubrovine, K. Burke, B. Steinberger, L. D. Ashwal, R. G. Tronnes, S. J. Webb, and A. L. Bull (2014), Deep mantle structure as a reference frame for movements in and on the Earth, *Proceedings of the National Academy of Sciences*, *111*(24), 8735-8740, doi:10.1073/pnas.1318135111.

Touboul, M., T. Kleine, B. Bourdon, H. Palme, and R. Wieler (2007), Late formation and prolonged differentiation of the Moon inferred from W isotopes in lunar metals, *Nature*, *450*(7173), 1206-1209, doi:10.1038/nature06428.

Trampert, J., F. Deschamps, J. Resovsky, and D. Yuen (2004), Probabilistic Tomography Maps Chemical Heterogeneities Throughout the Lower Mantle, *Science*, *306*(5697), 853-856, doi:10.1126/science.1101996.

Tsuchiya, T., J. Tsuchiya, K. Umemoto, and R. M. Wentzcovitch (2004), Phase transition in MgSiO3 perovskite in the earth's lower mantle, *Earth and Planetary Science Letters*, *224*(3-4), 241-248, doi:10.1016/j.epsl.2004.05.017.

van der Hilst, R. D., M. V. de Hoop, P. Wang, S. H. Shim, P. Ma, and L. Tenorio (2007), Seismostratigraphy and Thermal Structure of Earth's Core-Mantle Boundary Region, *Science*, *315*(5820), 1813-1817, doi:10.1126/science.1137867.

Walker, A. M., A. M. Forte, J. Wookey, A. Nowacki, and J. M. Kendall (2011), Elastic anisotropy of D" predicted from global models of mantle flow, *Geochemistry Geophysics Geosystems*, *12*(10), Q10006, doi:10.1029/2011gc003732.

Wang, Y., and L. Wen (2004), Mapping the geometry and geographic distribution of a very low velocity province at the base of the Earth's mantle, *J. Geophys. Res.*, *109*(B10), B10305, doi:10.1029/2003jb002674.

Wang, Y., and L. Wen (2007a), Complex seismic anisotropy at the border of a very low velocity province at the base of the Earth's mantle, *Journal of Geophysical Research*, *112*(B9), B09305, doi:10.1029/2006jb004719.

Wang, Y., and L. X. Wen (2007b), Geometry and P and S velocity structure of the "African Anomaly", *Journal of Geophysical Research-Solid Earth*, *112*(B5), doi:10.1029/2006jb004483.

Weis, D., M. O. Garcia, J. M. Rhodes, M. Jellinek, and J. S. Scoates (2011), Role of the deep mantle in generating the compositional asymmetry of the Hawaiian mantle plume, *Nature Geosci.*, *4*(12), 831-838, doi:10.1038/Ngeo1328.

Wen, L. (2006), A compositional anomaly at the Earth's core-mantle boundary as an anchor to the relatively slowly moving surface hotspots and as source to the DUPAL anomaly, *Earth and Planetary Science Letters*, *246*(1-2), 138-148, doi:10.1016/j.epsl.2006.04.024.

Wen, L., and D. V. Helmberger (1998a), A two-dimensional P-SV hybrid method and its application to modeling localized structures near the core-mantle boundary, *Journal of Geophysical Research*, *103*(B8), 17901-17918, doi:10.1029/98jb01276.

Wen, L., and D. V. Helmberger (1998b), Ultra-Low Velocity Zones Near the Core-Mantle Boundary from Broadband PKP Precursors, *Science*, *279*(5357), 1701-1703, doi:10.1126/science.279.5357.1701.

Wen, L., P. Silver, D. James, and R. Kuehnel (2001), Seismic evidence for a thermo-chemical boundary at the base of the Earth's mantle, *Earth and Planetary Science Letters*, *189*(3-4), 141-153, doi:10.1016/S0012-821X(01)00365-X.

Wen, L. X. (2001), Seismic evidence for a rapidly varying compositional anomaly at the base of the Earth's mantle beneath the Indian Ocean, *Earth and Planetary Science Letters*, *194*(1-2), 83-95, doi:10.1016/S0012-821x(01)00550-7.

Wicks, J. K., J. M. Jackson, and W. Sturhahn (2010), Very low sound velocities in iron-rich (Mg,Fe)O: Implications for the core-mantle boundary region, *Geophysical Research Letters*, *37*, doi:10.1029/2010gl043689.

Williams, Q., and E. J. Garnero (1996), Seismic Evidence for Partial Melt at the Base of Earth's Mantle, *Science*, *273*(5281), 1528-1530, doi:10.1126/science.273.5281.1528.

Williams, Q., J. Revenaugh, and E. Garnero (1998), A correlation between ultra-low basal velocities in the mantle and hot spots, *Science*, *281*(5376), 546-549, doi:10.1126/science.281.5376.546.

Wookey, J., S. Stackhouse, J. M. Kendall, J. Brodholt, and G. D. Price (2005), Efficacy of the post-perovskite phase as an explanation for lowermost-mantle seismic properties, *Nature*, *438*(7070), 1004-1007, doi:10.1038/nature04345.

Wu, Z., and R. M. Wentzcovitch (2014), Spin crossover in ferropericlase and velocity heterogeneities in the lower mantle, *Proceedings of the National Academy of Sciences*, *111*(29), 10468-10472, doi:10.1073/pnas.1322427111.

Yamazaki, D., T. Yoshino, H. Ohfuji, J.-i. Ando, and A. Yoneda (2006), Origin of seismic anisotropy in the D" layer inferred from shear deformation experiments on post-

perovskite phase, *Earth and Planetary Science Letters*, *252*(3-4), 372-378, doi:10.1016/j.epsl.2006.10.004.

Zerr, A., and R. Boehler (1994), Constraints on the melting temperature of the lower mantle from high-pressure experiments on MgO and magnesioustite, *Nature*, *371*(6497), 506-508, doi:10.1038/371506a0.

Zhang, N., S. Zhong, W. Leng, and Z.-X. Li (2010), A model for the evolution of the Earth's mantle structure since the Early Paleozoic, *Journal of Geophysical Research*, *115*(B6), doi:10.1029/2009jb006896.

Zhong, S., M. T. Zuber, L. Moresi, and M. Gurnis (2000), Role of temperature-dependent viscosity and surface plates in spherical shell models of mantle convection, *J. Geophys. Res.*, *105*(B5), 11063-11082, doi:10.1029/2000jb900003.

Zhong, S. J. (2006), Constraints on thermochemical convection of the mantle from plume heat flux, plume excess temperature, and upper mantle temperature, *Journal of Geophysical Research-Solid Earth*, *111*(B4), doi:10.1029/2005jb003972.

APPENDIX A

HYBRID TRACER METHOD

The rate of chemical diffusion is nearly zero. In numerical modeling, the composition field is often simulated by tracers that are advected with mantle flows. The buoyancy forces due to intrinsic density anomaly of compositional components in each element of the model are scaled with the number of tracers within the element. In this appendix, I will first describe the ratio tracer method and absolute tracer method [*Tackley and King*, 2003]. This is followed by the theory of hybrid tracer method we developed and used in Chapter 5. Finally, benchmark results for the hybrid tracer method are provided.

A.1 Absolute Tracer Method and Ratio Tracer Method

In thermochemical geodynamical modeling, two methods are typically used to model the compositional advection: ratio tracer method and absolute tracer method [*Tackley and King*, 2003].

For the absolute tracer method, the composition fraction (C_i) of each compositional component (except the background mantle) is proportional to the number of tracers per volume:

$$C_i = \frac{N_i V_0}{V} \tag{A.1}$$

Here, N_i is the number of tracers for the ith compositional component in an element, V is the volume of the element and V_0 is a constant which equals to average volume per tracer for the ith compositional component.

From Eq. (A.1), when N_i equals zero (i.e., no trace in the element), C_i becomes zero, which is the case for the background mantle. For absolute tracer method, all tracers are used to simulate chemical heterogeneities and background mantle contains zero

number of tracers. Thus, the number of tracers required is related to the volume of chemical heterogeneities. This becomes a big advantage when the size of chemical heterogeneities is very small (e.g., the ULVZs), which could be efficiently simulated with a small amount of tracers.

For ratio tracer method, the background mantle is also represented by tracers. Usually, the density of the background mantle is the reference density and the buoyancy number for the background mantle equals zero. The compositional fraction (C_i) for each compositional component within an element is:

$$C_i = \frac{N_i}{N} \tag{A.2}$$

Here, N_i is the number of tracers in the element used to simulate the ith compositional component. N is the total number of tracers in that element.

The ratio tracer method is benchmarked, and compared with absolute tracer method in [*Tackley and King*, 2003]. The ratio tracer method has several advantages over the absolute tracer method, such as minimal numerical diffusion and low entrainment. Thus, ratio tracer method is often used when dealing with large-scale chemical heterogeneities (i.e., LLSVPs), because in this case the absolute tracer method also needs large amount of tracers and no longer has the advantage of modeling the compositional heterogeneities using less amount of tracers.

A.2 Hybrid Tracer Method

In the work presented in Chapter 5, our model is featured by both large- and small scale compositional heterogeneities, which resemble the LLSVPs and ULVZs, respectively. We developed a new hybrid tracer method which combines the advantages

of ratio and absolute tracer method. Here, the background mantle and large scale compositional heterogeneity of LLSVPs are simulated with ~710 million ratio tracers and the smaller scale compositional heterogeneity of ULVZs is modelled with ~52-110 million absolute traces (depending on the initial volume of ULVZ material).

For hybrid tracer method, the chemical driving force (the last term of Eq. (5.2)) contains two parts. One part is from background mantle and LLSVP material which are modelled with ratio tracers, and is given as:

$$F_c^r = B_{LLSVP} * C_{LLSVP} + B_{bg} * C_{bg} \tag{A.3}$$

Here, B_{LLSVP} is the buoyancy number of LLSVP material and C_{LLSVP} is compositional fraction of LLSVP material which is calculated using Eq. (A.2). B_{bg} and C_{bg} are buoyancy number and compositional fraction for the background mantle, respectively. The buoyancy number of background mantle is $B_{bg} = 0$, so Eq. (A.3) effectively becomes:

$$F_c^r = B_{LLSVP} * C_{LLSVP} \tag{A.4}$$

The other part of the chemical driving force is from ULVZ material which is modelled with absolute tracers, and is given as:

$$F_c^a = B_{ULVZ} * C_{ULVZ} \tag{A.5}$$

Here, B_{ULVZ} is the buoyancy number of ULVZ material and C_{ULVZ} is compositional fraction of ULVZ material which is calculated using Eq. (A.1). We truncated C_{ULVZ} at 1 to avoid unphysically settling of tracers [see *Tackley and King*, 2003].

In the hybrid tracer method, the chemical driving force (F_c) is a summation of F_c^a and F_c^r:

$$F_c = F_c^a + F_c^r * (1 - C_{ULVZ})$$ (A.6)

or,

$$F_c = B_{ULVZ} * C_{ULVZ} + F_c^r * (1 - C_{ULVZ})$$ (A.7)

Notice that, for $C_{ULVZ} = 0$ (element has no ULVZ material), F_c is equivalently calculated using ratio tracer method; for $C_{ULVZ} = 1$ (element is saturated with ULVZ material), F_c is equivalently calculated using absolute tracer method.

A.3 Benchmarks

Here, we perform numerical calculations to test the hybrid tracer method, which is compared with ratio tracer method. The 2D Cartesian model we used here contains 128x128 elements, with grid gradually refined towards the bottom of the model, resulting in 5 km resolution at the lowermost 50 km. We use both visual comparison of the temperature and composition field and quantitative diagnostics to evaluate the robustness of the hybrid tracer method.

A.3.1 Entrainment of a Dense Thin Layer

This test treats the entrainment of a thin layer of dense material. To obtain an appropriate initial condition, an isochemical calculation is performed until thermal equilibrium and the temperature field after thermal equilibrium is used as initial temperature condition for thermochemical calculations. Initially, a 10 km thick dense layer ($B = 2.0$) is introduced at the bottom of the mantle. For ratio tracer method (Case R1.1-R1.4, where "R" in the name of these cases refers to ratio tracer method), both the background mantle and dense material are simulated with ratio tracers. For hybrid tracer

method (Case H1.1, where "H" in the name of this case refers to hybrid tracer method), the background mantle is simulated with ratio tracers, and the dense layer is modelled with about 5,664 number of absolute tracers, or ~22 absolute tracers per element in dense layer regions. Cases used in this test are listed in Table A.1.

Shortly after the initial condition, the dense material is swept to the upwelling region beneath a mantle plume and the dense material is consistently entrained into the mantle plume and mixed into the background mantle. Figure A1 shows a snapshot at $t = 0.06$ (non-dimensional) for Case R1.2 and Case H1.1. Notice that both cases have similar convection pattern. However, the size of dense pile for the case with hybrid tracer method (Figure A1c, d; Case H1.1) is larger than that for the case with ratio tracer method (Figure Aa, b; Case R1.2), which indicates that hybrid tracer method results in slower entrainment.

We further defined the 'Mass' of dense elements (elements whose chemical driving force F_c is larger than 1.0) to quantify the entrainment rate:

$$Mass = \int_{1.0}^{2.0} F_c dv \tag{A.8}$$

The changes of this Mass as a function of time is shown in Figure A2. We see that for cases with ratio tracer method (Case 1.1-Case 1.4), more tracers per element leads to slower entrainment of the dense material. However, the dense material is entirely entrained away by the mantle plume after t~0.085 for these cases. In the contrast, the dense material remains at the bottom of the model until $t = 0.1$ for Case H1.1 in which the compositional field is simulated with hybrid tracer method. This result shows that the hybrid tracer method enables slower entrainment rate than the ratio tracer method. In

addition, for Case R1.4, up to 983,040 tracers are used (averaging 60 tracers per element) to model the advection of composition, while only 87,584 tracers (including 5,664 absolute tracers and 81,920 ratio tracers) are used for Case H1.1, less than 9% of the number of tracers used for Case R1.4. In fact, since the buoyancy number of the background mantle is zero, the 81,920 ratio tracers used in Case H1.1 to simulate the background mantle are redundant. Only 5,664 absolute tracers are needed to simulate the dense layer for the hybrid tracer method, which is less than 0.58% of the number of tracers used in Case R1.4.

In conclusion, in this test we find that the hybrid tracer method uses much less amount of tracers, but results in lower entrainment rate than the ratio tracer method.

A.3.2 Interaction between Large Scale and Small Scale Compositional Heterogeneity

This test treats the interaction between three compositional components: a large scale composition heterogeneity with an initial thickness of 300 km (hereafter denoted as LLSVP material) and buoyancy number of $B = 0.8$, a small scale compositional heterogeneity with an initial thickness of 10 km (hereafter denoted as ULVZ material) and buoyancy number $B = 2.0$, and the background mantle which has a buoyancy number of zero. To obtain an appropriate initial condition, we first run a calculation with only two compositional components, including the large scale chemical heterogeneity and background mantle, until thermal equilibrium. Then the temperature field under thermal equilibrium is used as initial temperature condition for three compositional components thermochemical calculations. Here, the thermochemical calculations are performed using either ratio tracer method (Case 2.1-Case 2.4) in which all three

compositional components are modeled with ratio tracer method or hybrid tracer method (Case H2.1-Case H2.4) in which the background mantle and LLSVP material are modeled with ratio tracer method while the ULVZ material is modeled with about 5,664 number of absolute tracers, or ~22 absolute tracers per element in ULVZ regions. Cases used in this test are listed in Table A.2.

Shortly after the initial condition, the LLSVP material is formed into a large pile beneath an upwelling mantle plume at the right corner of the model and the ULVZ material is located at the left edge of the pile and the ULVZ material is consistently entrained into the pile. Figure A3 shows a snapshot at $t = 0.019$ (non-dimensional) for Case R2.2 and Case H2.1. Notice that the dynamics shown in both cases are similar, except that for Case H2.1, slightly more ULVZ material resides at the edge of the pile than Case R2.2.

Figure A4 shows a snapshot at $t = 0.033$ (non-dimensional) for the same cases (Case R2.2 and Case H2.1) shown in Figure A3 At this time, all ULVZ material is entrained into the pile and background mantle and no ULVZ material is left at the edge of the LLSVP pile. However, for Case R2.2, some elements at the bottom of the model still have high chemical driving forces, which are shown by yellow and red color in Figure A4b. This is unrealistic and is caused by not enough ratio tracers are used in Case R2.2. Because of grid refinement, the number of tracers per element at the lowermost mantle is less than the average number of tracers per element. So, averaging 10 tracers per element in Case R2.2 results in only about 2 tracers per element at the lowermost 50 km of the model. For the ratio tracer method, the chemical driving force of one element is calculated from the fraction of different types of ratio tracers. As a result, very small

178

amount of tracers in the element could lead to artifacts. For example, if the element only contains 1 ratio tracer representing the ULVZ material, the chemical driving force of the element is 2.0 (which equals to the buoyancy number of ULVZ material); if this tracer represents the LLSVP material, the chemical driving force of the element is 0.8 (which equals to the buoyancy number of LLSVP material). This leads to neighboring elements having very different chemical driving forces, which is numerical noise. The problem is solved when increasing the number of tracers (showed in Figure A5). However, for the case with hybrid tracer method (Case H2.1), the chemical driving forces of elements are much smoother (Figure A4d).

Figure A5 shows the time evolution of the Mass of dense elements as defined in Eq. (A.8), for cases in which ratio tracer method is used (Case R2.1-Case R2.4). After $t \sim 0.045$ (non-dimensional), the Mass almost becomes zero when more than averaging 10 ratio tracers per element are used, indicating all ULVZ material is either mixed into the background mantle or entrained into the large LLSVP pile. The high Mass for the cases (Case R2.1 and Case R2.2) using only averaging 5 or 10 ratio tracers per element is due to artifacts as discussed above.

However, for the hybrid tracer method, the effect of number of ratio tracers on the entrainment of dense material is negligible, as is shown in Figure A6. We vary the averaging number of ratio tracers per element from 5 in Case H2.1 to 60 in Case H2.4. However, all cases with hybrid tracer method show similar Mass as a function of time. In summary, to avoid artifacts due to not enough number of tracers, at least 491,520 tracers (or averaging 30 tracers per element) are needed for the ratio tracer method. However for the hybrid tracer method, only 87,584 tracers (including 5,664 absolute tracers and

81,920 ratio tracers) are needed for hybrid tracer method, less than 18% of the number of tracers for the ratio tracer method.

A.4 Discussion and Conclusion

In numerical modeling, high resolution calculations are always challenging, especially in 3D thermochemical calculations. One of the difficulties is to increase the number of tracers needed to simulate the compositional field. It is because increasing the number of tracers not only increases the amount of computing time, the number of tracers is limited by the memory of the computational cluster as well. Thus, a good method should be able to model the advection of composition efficiently using less amount of tracers.

The ratio tracer method has several advantages over absolute tracer method such as less minimal statistical "noise" and low entrainment [*Tackley and King*, 2003]. However, the drawback of ratio tracer method is that the total amount of tracers needed is much more than absolute tracer method if the size of chemical heterogeneities is very small. Here, we developed a new hybrid tracer method which combines the advantages of both ratio and absolute tracer method. For hybrid tracer method, the large scale background mantle and large scale chemical heterogeneities are simulated with ratio tracers and the small scale chemical heterogeneities are simulated with absolute tracers. The hybrid tracer method enables us to model the interaction between large and small compositional reservoirs using much less amount of tracers than that of the ratio tracer method and absolute tracer method.

References

Tackley, P. J., and S. D. King (2003), Testing the tracer ratio method for modeling active compositional fields in mantle convection simulations, *Geochemistry Geophysics Geosystems*, *4*(4), 8302, doi:10.1029/2001gc000214.

Table A.1

Cases Used in Modeling the Entrainment of A Thin Dense Layer.

Case	Average number of ratio tracers per element	Total number of absolute tracers
R1.1	5	N/A
R1.2	10	N/A
R1.3	30	N/A
R1.4	60	N/A
H1.1	5	5,664

Table A.2

Cases Used in Modeling the Interaction between Large Scale and Small Scale

Compositional Heterogeneities.

Case	Average number of ratio tracers per element	Total number of absolute tracers
R2.1	5	N/A
R2.2	10	N/A
R3.3	30	N/A
R2.4	60	N/A
H2.1	5	5,664
H2.2	10	5,664
H2.3	30	5,664
H2.4	60	5,664
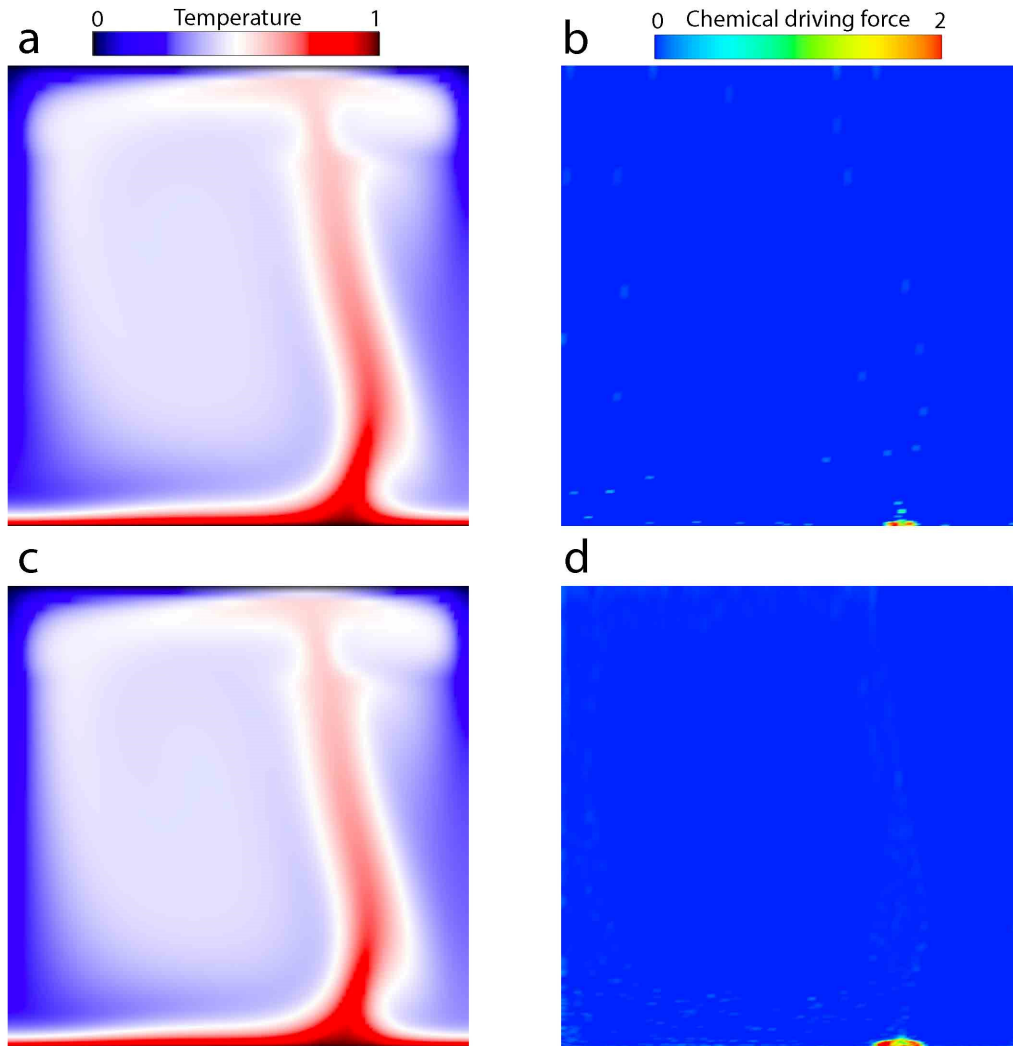
Figure A1. Snapshot ($t = 0.06$) for Case R1.2 (a, b) and Case H1.1 (c, d). a, c, temperature field. b,d, composition field represented by chemical driving force. For ratio tracer method, averaging 10 ratio tracers per element are used to simulate the compositional field. For hybrid tracer method, averaging 5 ratio tracers are used to simulate the background mantle and 5,664 absolute tracers are used to simulate the dense material with buoyancy number B=2.0.
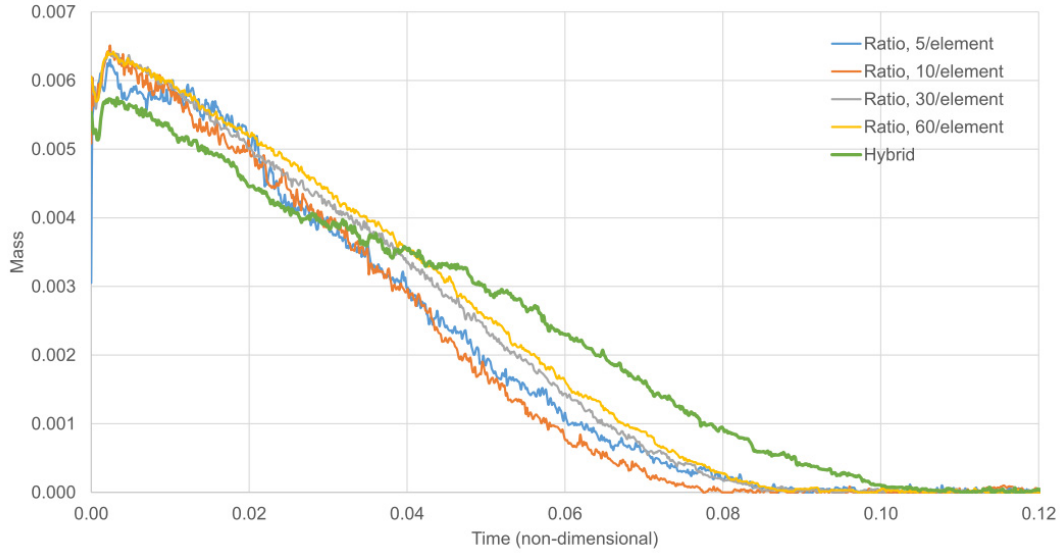
Figure A2. Time evolution of mass of the dense elements. For cases with ratio tracer method, the averaging number of ratio tracers per element is 5 (Case R1.1), 10 (Case R1.2), 30 (Case R1.3), and 60 (Case R1.4). For the case with hybrid tracer method (thick green line), we use averaging 5 ratio tracers per element to model the background mantel and additional 5,664 absolute tracers to model the dense material (Case H1.1).
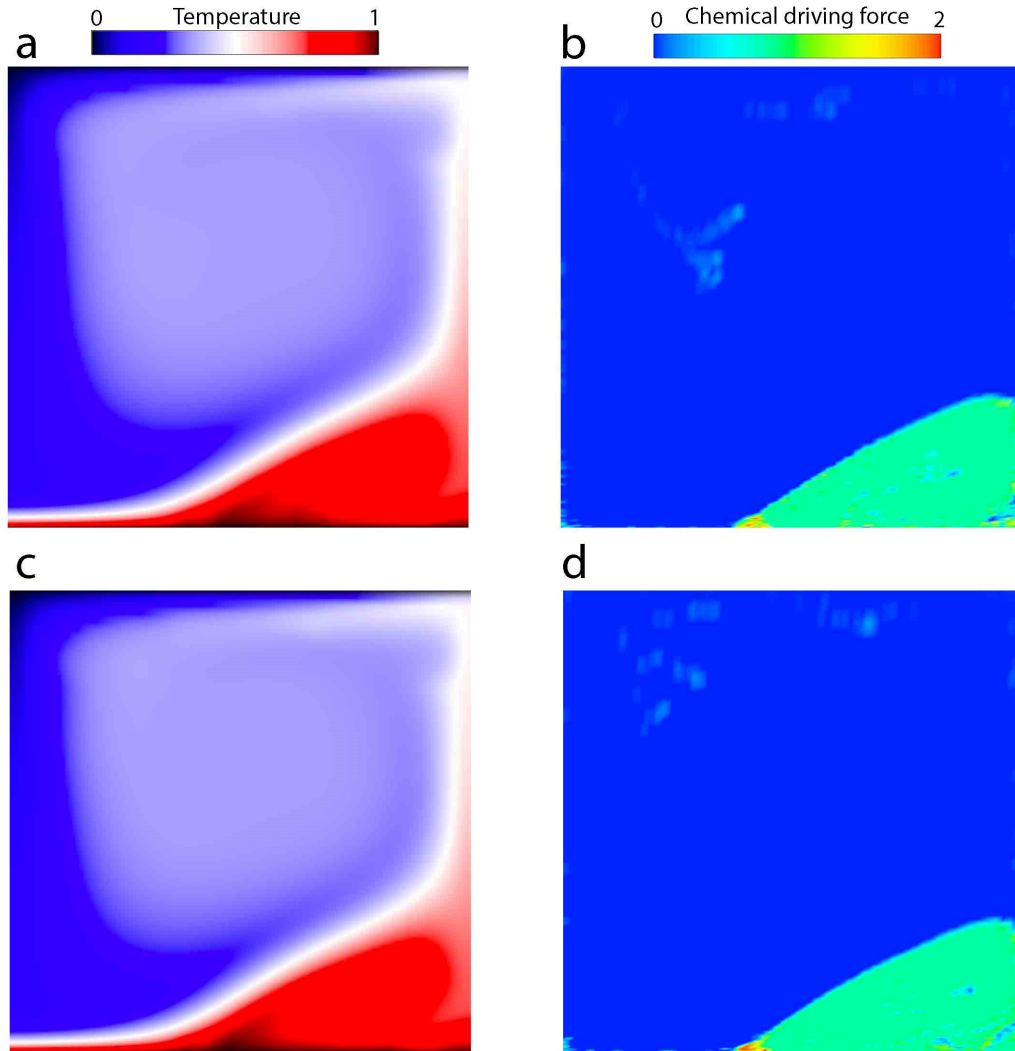
Figure A3. Snapshot ($t = 0.019$) of Case R2.2 (a, b) and Case H2.1 (c, d). a, c, temperature field. b,d, composition field represented by chemical driving force. For ratio tracer method, averaging 10 ratio tracers per element are used to simulate the compositional field. For hybrid tracer method, averaging 5 ratio tracers are used to simulate the background mantle and an additional 5,664 absolute tracers are used to simulate the ULVZ material.
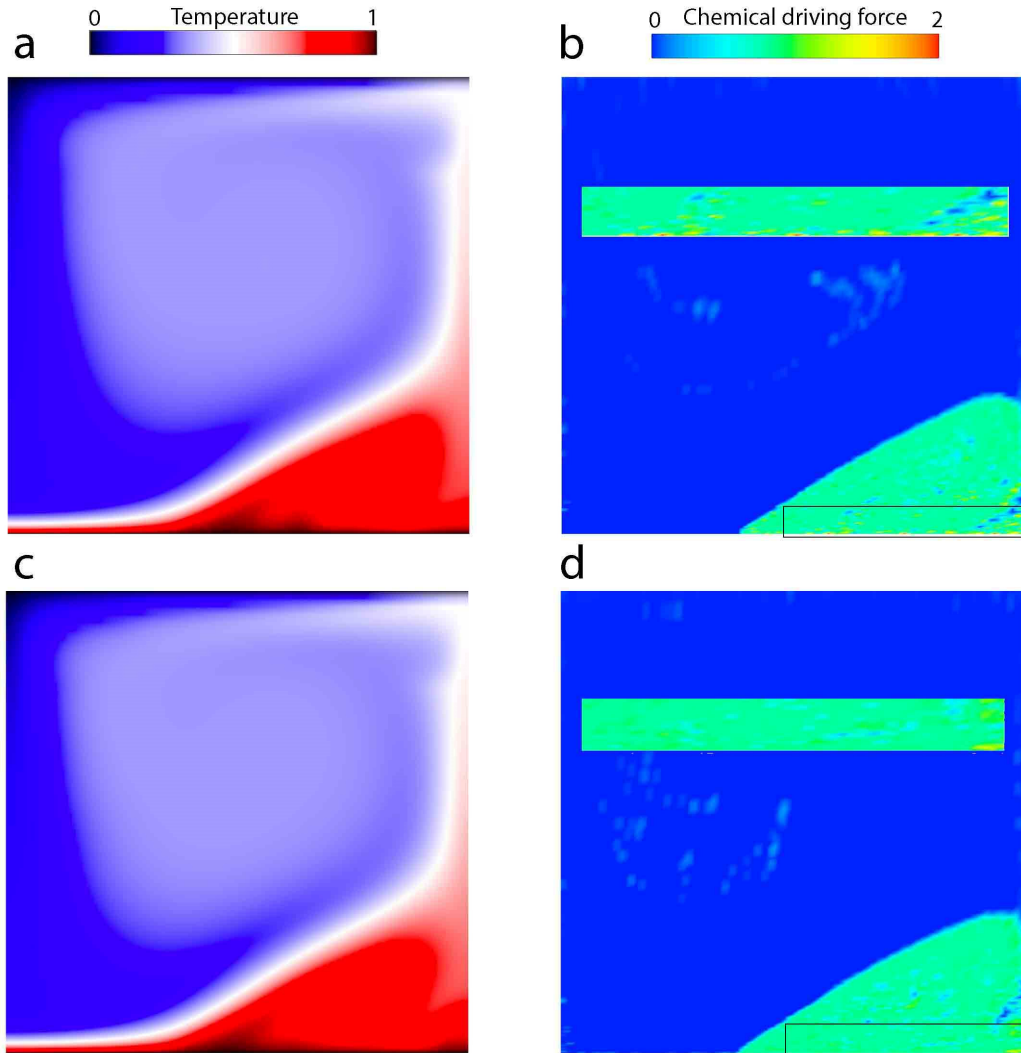
Figure A4. Snapshot ($t = 0.033$) of Case R2.2 and Case H2.1. a, c, temperature field. b,d, composition field represented by chemical driving force. The intersection in b, and d is zoomed-in from the region outlined by black rectangle in b, and d, respectively.
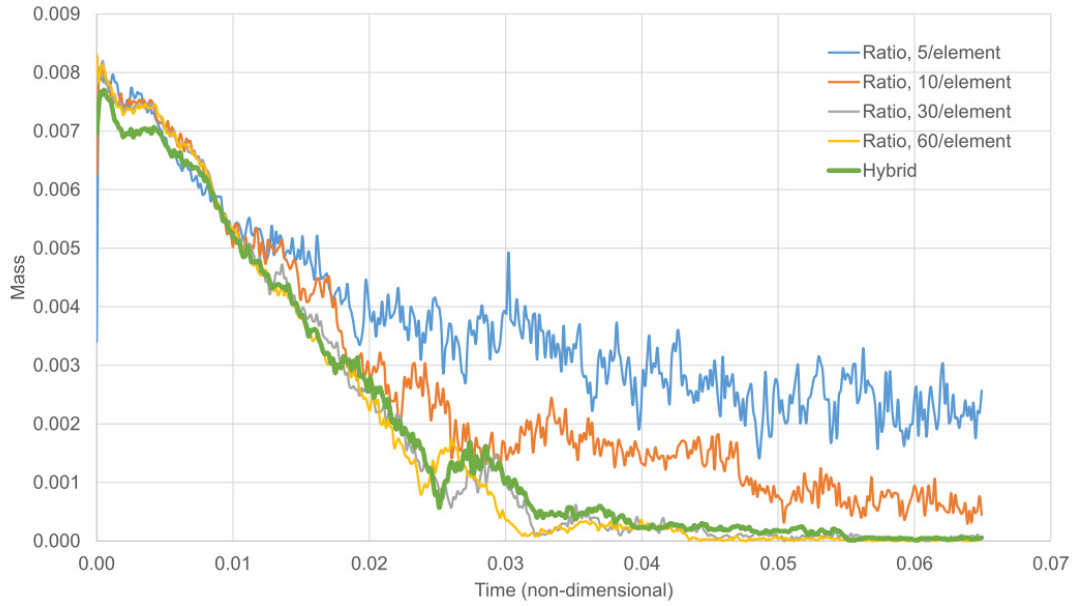
Figure A5. Time evolution of mass of the dense elements. Four cases using ratio tracer method are shown with varying averaging number of ratio tracers per element. For comparison, we also show the result of Case H2.1 (thick green line) with hybrid tracer method which contains averaging 5 ratio tracers per element and additional 5446 absolute tracers to model the ULVZ material.
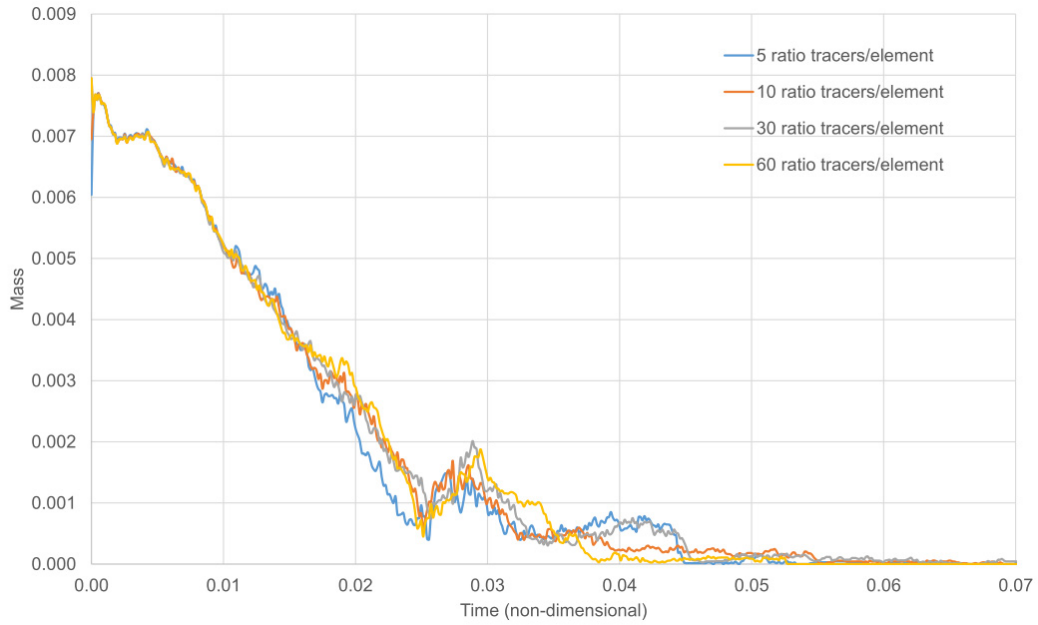
Figure A6. Time evolution of mass of the dense elements for cases with hybrid tracer method. Here, the averaging number of ratio tracers per element is 5 (Case H2.1), 10 (Case H2.2), 30 (Case H2.3), and 60 (Case H2.4), and we use additional 5,664 absolute tracers to model the ULVZ material.

APPENDIX B

COOLING THE EDGES OF LLSVPS BY THERMAL DIFFUSION

Here, we performed 2 two-dimensional isochemical calculations (Case B1 and Case B2) to study the process of cooling the edges of thermochemical piles by thermal diffusion. In these 2D models, temperature is isothermal both on the top (T=0.0) and at the bottom (T=1.0). All boundaries are free slip. Viscosity is temperature dependent with $\eta = \exp[A(0.5 - T)]$, where A=6.91, leading to 1,000 viscosity change due to changes of temperature. In addition, a viscosity increases of 50x is employed from upper mantle to lower mantle. Both cases have a Rayleigh number of Ra=1e6. The model has an aspect ratio of 1 and is divided into 128x128 elements.

All physical parameters of both cases are the same, except that for Case B1, both side boundaries are insulating, while for Case B2, the right boundary is insulating but the left boundary is isothermal with a temperature of T=0.5, which acts as a 'cooling' boundary. Figure B1 shows snapshots of temperature field for both two cases when in thermal equilibrium. For Case B1 (Figure B1a), single cell convection is established with cold downwelling occuring at the right boundary and hot upwelling at the left boundary. Hot thermal instabilities in the lowermost mantle are advected to the left side boundary. In this case, the hottest regions occur at the lower left of the model. However, when a cooling left boundary is employed (Case B2, Figure B1b), the hottest regions are located away from the left boundary, because of cooling by the left boundary.

Similarly, the edges of LLSVPs are cooled down by thermal diffusion from surrounding cold background mantle, and as a result, the hottest region appears inboard from the edges of LLSVPs.
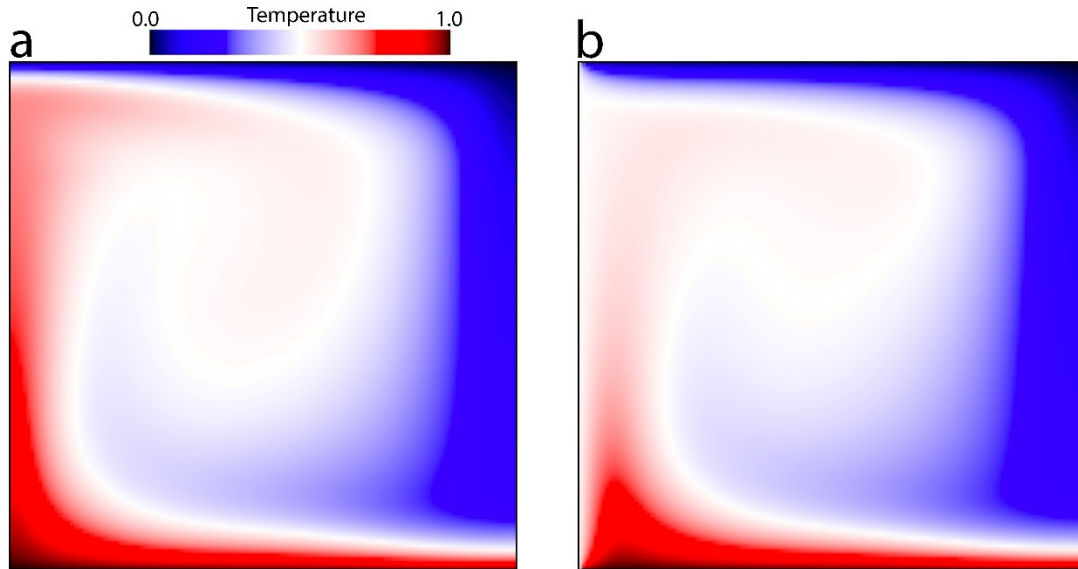
Figure B1. Steady state temperature field for (a) Case B1 and (b) Case B2. For Case B1, both side boundaries are insulating; for Case B2, the right boundary is insulating while the left boundary is isothermal with a temperature of T=0.5. Notice that for Case B1, the hottest regions occur at the lower left corner of the model. For Case B2, the hottest regions are located off the left boundary which is cooled down by thermal diffusion.